Multilayer Meta-optics for Next-generation Multifunctional Photonics

Thesis by
A. Bilgehan Baspinar

In Partial Fulfillment of the Requirements for the
Degree of
Doctor of Philosophy in Applied Physics



CALIFORNIA INSTITUTE OF TECHNOLOGY
Pasadena, California

2026
Defended May 27, 2026

© 2026

A. Bilgehan Baspinar
ORCID: 0009-0005-5382-6118

All rights reserved except where otherwise noted

To my mother and my brother, whose support has carried me through a lifetime.

ACKNOWLEDGEMENTS

When I first landed in LAX, it was my first time in the United States. Besides the sheer distance from home, the thought of being here permanently for the next several years of my life was more than a little terrifying in the beginning. The fact that my very first experience in the US was spending weeks indoors in a dorm under quarantine did not help matters either. But slowly, I began to discover what a beautiful little city I had found myself in, and what a remarkable campus I got to work on every day. In the beginning, I remember how intrigued I was by the squirrels on campus, whom I fed with the nuts I brought back from home (and my mom was not happy about it). I can't believe I'm acknowledging the squirrels first in the most important document I have ever written, but let me now turn to the people who helped me throughout this journey.

First and foremost, I owe my deepest gratitude to my advisor, Professor Andrei Faraon. He not only shaped me into the researcher I am today, but he also showed me the way whenever I felt lost, offered sharp insight and direction across all of my projects, and gave me both the resources and the freedom to pursue the work I cared about most. Throughout my PhD journey, he has been tremendously supportive, and I am deeply grateful for his guidance, patience, and encouragement at every step.

I would like to thank Professor Kerry Vahala, Professor Harry Atwater, and Professor Axel Scherer for serving on my doctoral thesis committee. They are pioneers in their respective fields, and I am truly honored to have had them in my committee.

I would also like to thank my labmates, as I feel incredibly lucky to have worked alongside both the current and former members of our group. Though Han graduated not long after I joined, he was a wonderful mentor who laid a strong foundation for my understanding of nanophotonic design and simulations. Terry taught me a great deal about nanofabrication and cleanroom practices that I carried throughout my PhD. Ian has been one of my closest friends over these past years, and working with him was just as much fun. Phil had an uncanny ability to offer exactly the right insight at exactly the right moment, pulling me out of more than a few dead ends. I learned a tremendous amount from Suki on the fabrication side, and our office conversations were always a highlight of my day. I also had a wonderful time working with the former meta-optics members, Greg, Conner, and Ding, from

whom I learned more than I can properly express. I am grateful to Jiahui, Antonia, and Emanuel in our quantum optics subgroup for their support and collaboration on my projects. And though they have since moved on from Caltech, I fondly remember the conversations I had with Mi, Chun-Ju, and Andrei. To the rest of the Faraon group, Riku, McCoy, Erin, Faraz, Will, Max, Matilda, and Dennis, thank you for making the lab such a genuinely great place to work. I have no doubt that every one of them will go on to do remarkable things.

I would like to thank our collaborators at JPL, Jeffrey Jewell and Mahmood Bagheri. Getting to work with NASA JPL was something of a childhood dream, and I am glad it became a reality. I would also like to acknowledge the staff at the Kavli Nanoscience Institute (KNI) who kept everything running: Guy, Bert, Alireza, Alex, Nathan, Kelly, Yonghwi, Tiffany, and Sydney. Their dedication to maintaining the tools and facilities was absolutely essential to my work. I also had the privilege of TAing for Alireza on two occasions, which turned out to be one of the more rewarding experiences of my PhD. And I cannot leave out Alessandro, whom I met in the cleanroom, the things I learned from him are too numerous to count, and I am grateful for every one of them.

I would like to thank Saman, my mentor during my internship at ASML, who taught me not just technical skills but the broader set of habits and instincts needed to thrive in an industrial environment. I am certain those lessons will stay with me throughout my career. I would also like to thank my manager Steve Cordes for his steady guidance and for making sure I was set up for success throughout my time there.

To the amazing friends I made during my PhD, Ian, Prachi, Riwa, Su, Eyyup, Mi, Fatima, Minzhi, you made an incredibly challenging experience feel, at times, like a great adventure. I would also like to thank the friends who have been in my life far longer. Asli, my college roommate, is one of the people who makes me laugh most, and I am grateful to have her by my side here in California. And Ahmad, one of the most philosophical and poetic people I've ever known whom I had the privilege to meet during my college years, thank you both. Canan and Zeyneb, I have been lucky enough to call you my friends for fifteen years now. Canan, our travels together have given me some of my most cherished memories, and I look forward to many more. Zeyneb, you are one of the first people I seek out every time I go back to Turkey, and I am so glad that 7,000 miles never managed to change that. Thank you both for the kind of friendship that holds regardless of distance or time.

Last but not least, I feel incredibly fortunate to have reconnected with an old undergraduate friend, Eray, here in LA, never imagining that he would one day become my partner. Having you in my life has been one of the greatest gifts of this chapter. Thank you for your selflessness, for standing by me through everything, and for the kind of unconditional support that made the hardest days feel manageable. I would also like to thank my family, especially my mom and my brother. My mom has been my biggest supporter from the very beginning, supporting every decision I made, including the one that sent me across the world, even when it meant being apart. My brother has always been my ultimate best friend whose support I have always felt no matter what, and nothing will ever change that. I am endlessly grateful to have all of these amazing people in my life. This journey would not have been the same, and honestly could not have been completed, without their love, their presence, and the joy they brought into my life.

ABSTRACT

Optical metasurfaces, planar arrays of subwavelength scatterers that enable precise manipulation of light's amplitude, phase, and polarization, have emerged as a compelling platform for next-generation photonic systems. While single-layer passive metasurfaces have demonstrated remarkable optical functionalities, practical applications increasingly demand devices that are dynamically reconfigurable, spectrally multifunctional, and compatible with scalable nanofabrication. This thesis addresses these challenges through the design, fabrication, and characterization of active and multilayer metasurfaces across a diverse set of photonic applications.

We first propose and computationally investigate a nanoelectromechanically tunable metasurface architecture based on slot-mode resonances at telecom wavelengths. An on-substrate design employing high-aspect-ratio doped silicon slabs circumvents the mechanical fragility of prior suspended architectures, achieving 80% amplitude modulation and 1.4π phase modulation within 10 V, and enabling beam steering with up to 58% efficiency.

We then establish a high-throughput direct-write electron-beam lithography platform in which an antimony-BDCA precursor decomposes in situ into high-index Sb_2S_3, eliminating deposition and etching steps entirely and enabling efficient multilayer fabrication. Leveraging this platform, we demonstrate three-layer quasi-bound-state-in-the-continuum-derived metasurfaces with independently tunable resonance wavelengths and quality factors, and construct decorrelated filter arrays achieving average absolute pairwise Pearson correlation coefficients of 0.11 and 0.21 for sets of 9 and 36 filters, surpassing prior metasurface and photonic-crystal implementations for compressive hyperspectral reconstruction. The same platform is applied to vertical fiber-to-chip coupling, where adjoint-based inverse design with the Adam optimizer across 204 geometric parameters yields a simulated peak coupling efficiency of 89.5% (-0.48 dB) at 1550 nm without any modification to the underlying photonic integrated circuit.

We further apply the Sb_2S_3 direct-write platform to the design and fabrication of ten-layer Bayer color routers operating in the visible spectrum. Six device variants are designed by adjoint-based inverse optimization, spanning three refractive index values and two RGB design wavelength sets, and fabricated on a transparent doped-SiC substrate. To our knowledge, this represents the first free-form multilayer

meta-optic Bayer color router in the visible spectrum and the highest layer count demonstrated with the direct-write Sb_2S_3 platform to date.

We then present the design, fabrication, and Mueller-matrix polarimetric characterization of geometric-phase TiO_2 and amorphous silicon metasurfaces functioning as phase aberration correctors for optical vortex coronagraphs, confirming spatially uniform retardance of $(179.4 \pm 0.4)^\circ$ and average transmission exceeding 84% across centimeter-scale apertures. Finally, a planar amorphous silicon metamirror encoding a quadratic reflection phase profile is used to stabilize a Fabry–Pérot cavity enclosing a YVO_4:Yb^{3+} crystal for microwave-to-optical quantum transduction, with spatially resolved finesse measurements confirming a greater than two-fold improvement approaching the mirror-reflectivity-limited theoretical maximum.

Taken together, this body of work demonstrates that active and multilayer metasurface platforms, when co-developed with purpose-built fabrication methods and physics-informed design tools, can meet the performance demands of applications as varied as reconfigurable beam steering, spectral reconstruction, on-chip photonic integration, astronomical imaging, and cavity-enhanced quantum transduction.

PUBLISHED CONTENT AND CONTRIBUTIONS

[1] A. B. Baspinar, T. Zheng, H. Kwon, and A. Faraon. "Nanoelectromechanically Tunable Dielectric Metasurfaces for Reconfigurable Wavefront Shaping". *ACS Photonics* 11.9 (2024), pp. 3585–3592. DOI: 10.1021/acsphotonics.4c00559.
B.B. participated in the conception of the project, design of the devices, sample fabrication, sample measurement, data analysis and writing of the manuscript.

[2] A. B. Baspinar, P. Pearson, and A. Faraon. "Multilayer Q-BIC-Like Optical Filters with High Throughput Direct-Write Multilayer Lithography". *Advanced Optical Materials* (2026), e71282. DOI: 10.1002/adom.71282.
B.B. participated in the conception of the project, design of the devices, sample fabrication, sample measurement, data analysis and writing of the manuscript.

[3] A. B. Baspinar, A. Ghita, and A. Faraon. "Sub-Decibel Efficiency Augmented Multilayer Vertical Coupler for Integrated Optics via Adjoint Inverse Design". *In Preparation* (2026).
B.B. participated in the conception of the project, design of the devices, sample fabrication, sample measurement, data analysis and writing of the manuscript.

[4] A. B. Baspinar*, I. Foo*, and A. Faraon. "Multilayer Bayer Filter in Visible via Direct-Write E-Beam Lithography". *In Preparation* (2026).
B.B. participated in the conception of the project, sample fabrication, and writing of the manuscript.

TABLE OF CONTENTS

Acknowledgements . . . iv
Abstract . . . vii
Published Content and Contributions . . . ix
Table of Contents . . . ix
List of Illustrations . . . xii
List of Tables . . . xiv
Chapter I: Introduction . . . 1
1.1 Flat Optics: Metasurfaces . . . 1
1.2 High-Contrast Dielectric Metasurfaces . . . 2
1.3 Multilayer and Volumetric Metamaterials for Multifunctionality . . . 4
1.4 Active Metasurfaces . . . 5
1.5 Thesis Outline . . . 7
Chapter II: Nano-electromechanically Tunable Dielectric Metasurfaces for Reconfigurable Wavefront Shaping . . . 9
2.1 Introduction . . . 9
2.2 Results and Discussion . . . 10
2.3 Conclusion . . . 19
2.4 Methods . . . 21
2.5 Appendix . . . 22
Chapter III: Multilayer Q-BIC-like Optical Filters with High Throughput Direct-Write Multilayer Lithography . . . 25
3.1 Introduction . . . 25
3.2 Results and Discussion . . . 27
3.3 Conclusion . . . 39
3.4 Appendix . . . 40
Chapter IV: Sub-Decibel Efficiency Augmented Multilayer Vertical Grating Coupler via Adjoint Inverse Design and Sb_2S_3 Direct-write E-beam Lithography . . . 48
4.1 Introduction . . . 48
4.2 Device Design . . . 51
4.3 Methods . . . 52
4.4 Results . . . 55
4.5 Fabrication-tolerance Analysis . . . 58
4.6 Discussion . . . 60
4.7 Conclusion . . . 62
4.8 Appendix . . . 63
Chapter V: Multilayer Bayer Color Router in the Visible via Direct-Write E-Beam Lithography . . . 65
5.1 Introduction . . . 65

5.2 Device Architecture . . . 66
5.3 Inverse Design and Optimization . . . 68
5.4 Fabrication . . . 68
5.5 Design and Results . . . 70
5.6 Conclusion and Outlook . . . 74
Chapter VI: Geometric phase metasurfaces for optical vortex coronographs . 75
6.1 Introduction . . . 75
6.2 Design and Fabrication . . . 77
6.3 Experimental Results . . . 81
6.4 Conclusion . . . 84
Chapter VII: Stable YVO_4 Quantum Transduction Cavity with Metamirrors . 86
7.1 Introduction . . . 86
7.2 Cavity Design and Stability Analysis . . . 88
7.3 Metamirror Design . . . 91
7.4 Cavity Characterization and Finesse Measurements . . . 93
7.5 Discussion . . . 95
Chapter VIII: Conclusion and Outlook . . . 97
8.1 Summary . . . 97
8.2 Outlook . . . 98
Bibliography . . . 100

LIST OF ILLUSTRATIONS

Number *Page*

2.1 NEMS metasurface architecture and slot mode characteristics 11
2.2 Amplitude and phase modulation under applied voltage 13
2.3 Dependence of optical response on slab, slot, and notch parameters . 14
2.4 Effect of notch depth and thickness on Q-factor, tunability, and phase coverage 15
2.5 Beam steering and steering efficiency optimization 17
2.6 SEM characterization and experimental slot mode coupling 22
2.7 Mechanical response and spectral tuning of the NEMS architecture . 23
3.1 Comparison of conventional nanofabrication and Sb_2S_3 direct-write multilayer fabrication flows 28
3.2 Unit cell design and spectral tuning of q-BIC-derived Sb_2S_3 metasurfaces 30
3.3 Three-layer rectangular-lattice device: simulation, measurement, and field profiles 33
3.4 Three-layer square-lattice device targeting six resonances 34
3.5 Decorrelated filter arrays for compressive spectral sensing 38
3.6 Cross-sectional SEM of the fabricated three-layer Sb_2S_3 device . . . 41
3.7 Optical and chemical characterization of Sb_2S_3 thin films 42
3.8 Resonance wavelength shift due to HSQ refractive index change upon electron exposure 44
3.9 Effect of HSQ spacer thickness on interlayer coupling and transmission spectra 45
3.10 Suppression of high-Q intra-post resonances under material absorption loss 46
4.1 Layer stack and simulation setup of the augmented two-layer grating coupler 50
4.2 Convergence of the adjoint optimization and final coupling efficiency spectrum 56
4.3 Optimized grating coupler geometry and electric field distribution . . 57
4.4 Fabrication tolerance analysis for the optimized grating coupler . . . 64

5.1 Visible Bayer filter transmission spectra for different device design configuration . . . 69
5.2 Transmission through the doped SiC bulk substrate . . . 70
5.3 Layers of the optimized design . . . 71
5.4 Preliminary experimental results . . . 73
6.1 Operating principle of a vector vortex coronagraph . . . 76
6.2 Broadband unit cell optimization for geometric phase metasurface coronagraph masks . . . 78
6.3 Hexagonal aperture and annular ring phase mask designs . . . 79
6.4 Optical and SEM images of fabricated geometric phase metasurface masks . . . 80
6.5 Ellipsometry measurement of ALD-grown TiO_2 refractive index . . . 81
6.6 Mueller matrix polarimetry characterization of the fabricated annular ring mask . . . 82
6.7 Measured HWP retardance orientation across the annular ring boundary 82
6.8 Wavelength-dependent retardance of a-Si half-wave plates . . . 83
6.9 Retardance uniformity and wavelength dependence of TiO_2 half-wave plates . . . 84
6.10 Simulated coronagraph contrast performance of broadband vortex phase masks . . . 84
6.11 Effect of fabrication phase errors on coronagraph contrast performance 85
7.1 Plano-concave cavity architecture with a DBR metamirror for YVO_4 quantum transduction . . . 89
7.2 Metamirror phase library and spatially varying pillar diameter profile 92
7.3 Spatially resolved finesse map confirming metamirror-enhanced cavity performance . . . 94

LIST OF TABLES

Number *Page*

4.1 Summary of grating coupler designs reported in the literature, including peak coupling efficiency, optimization method, and primary design objective. 61

7.1 Principal cavity and beam parameters. 91

Chapter 1

INTRODUCTION

The ability to shape, redirect, and confine light with precision underpins virtually every modern photonic technology, from the optical fiber networks that carry global internet traffic to the telescopes searching for biosignatures on distant exoplanets. For most of the history of optics, this control has been exercised by bulk refractive elements. These components impose strict limits on system size, weight, and functional reconfigurability, motivating a decades-long search for thinner, lighter, and more versatile alternatives [1, 2].

Optical metasurfaces, planar arrays of subwavelength scatterers engineered to impart spatially varying responses to amplitude, phase, and polarization, have emerged as a compelling answer to this challenge [1, 3, 4, 5, 6]. By encoding an arbitrary phase or amplitude profile into the geometry of individual meta-atoms, a single lithographically patterned surface only hundreds of nanometers thick can replicate the function of a lens [7], a hologram [8, 9], a beam steerer, or a spectral filter [10], all within a planar, chip-compatible form factor. This shift from bulk optics to flat optics is not merely a matter of miniaturization: it opens qualitatively new capabilities in multifunctionality, integration density, and, critically, active reconfigurability. In this thesis, we address several of these challenges through the design, fabrication, and characterization of active and multilayer metasurfaces across a range of applications.

This introductory chapter reviews the concepts and prior art that motivate the subsequent chapters. We begin with a general introduction to optical metasurfaces and their operating principles. We then focus on high-contrast dielectric metasurfaces and their capabilities for controlling phase and polarization. Next, we discuss the physics and prior work on multilayer and volumetric metamaterial architectures. We follow with a review of active metasurfaces and their principal tuning mechanisms. The chapter concludes with an outline of the thesis.

1.1 Flat Optics: Metasurfaces

Optical metasurfaces are two-dimensional arrays of subwavelength scatterers designed to manipulate multiple properties of light [1, 4, 5]. The operating principle of a metasurface rests on the ability of a single subwavelength scatterer, or meta-atom,

to impart a well-defined amplitude, phase, and polarization response to an incident electromagnetic field. When such meta-atoms are arranged in a two-dimensional array with slowly varying geometry, the array acts as a locally periodic structure. By the local periodicity approximation, each region of the array can be treated as if it were an infinite periodic lattice with the local geometrical parameters [11]. This approximation, which becomes exact as the meta-atom period decreases relative to the wavelength, allows a continuous phase or amplitude profile to be encoded spatially across the device aperture by varying the geometry from pixel to pixel.

Phase control in metasurfaces is achieved through three broad mechanisms. The geometric parameters of the meta-atoms can be used to control the amount of propagation phase imparted locally for applications where slowly varying phase distribuitions and/or a large bandwidth are needed. In geometric phase (Pancharatnam-Berry) metasurfaces, the phase shift is imparted purely by rotating a birefringent meta-atom, producing a geometric phase of twice the rotation angle [12, 13]. Geometric phase metasurfaces are inherently broadband, however they act only on circularly polarized light. Another approach is to tune the meta-atom geometry so that we hit one of the eigenmodes of the electromagnetic system, i.e. a resonance, accumulating a phase shift that varies steeply near the resonant wavelength [14, 15]. With resonant metasurfaces, although strong phase responses can be achieved, it is generally limited to a narrow bandwidth. In this thesis, NEMS based reconfigurable beam steering metasurface mentioned in Chapter 2 and multilayer optical filters mentioned in Chapter 3 rely on resonant metasurfaces for phase and amplitude modulation respectively. Multilayer vertical coupler mentioned in Chapter 4 and metamirror designed for stable cavities mentioned in Chapter 7 rely on propagation phase delay to locally modify the wavefront across the device. Finally, phase abberation correction masks designed for coronograph mentioned in Chapter 6 utilizes geometric phase, controlling the circularly polarized light locally through the orientation of the half-wave plate meta-atoms.

1.2 High-Contrast Dielectric Metasurfaces

Metasurface conceptual lineage traces to the reflect- and transmit-arrays that have been studied in the microwave community for several decades [16], and to conventional diffractive optical elements (DOEs) such as Fresnel lenses, holograms, and blazed gratings [17]. The early demonstrations of optical metasurfaces were based on plasmonic meta-atoms, where the resonances of metallic nanostructures were exploited to engineer a spatially varying phase profile [18, 19]. These early

devices demonstrated the basic operating principles convincingly, but the intrinsic ohmic losses of metals combined with fundamental limits on the achievable phase coverage in a single thin layer [20] restricted their efficiency, particularly in transmission. These limitations motivated the shift toward all-dielectric metasurfaces, which use high-refractive-index dielectric nanostructures such as silicon, titanium dioxide (TiO_2), or gallium nitride (GaN) to achieve low-loss wavefront control [21, 22, 7]. Such metasurfaces have been demonstrated enabling thin metalenses [7, 23], holograms [8, 9], beam deflectors [1], and spectral filters [10], all in a planar, chip-compatible geometry. Owing to the high refractive index contrast between the meta-atoms and their surrounding medium, the electric field is highly confined inside each nanopost, reducing inter-post coupling and making the phase response of each post largely insensitive to its neighbors [11]. This local-sampling property allows an arbitrary phase map to be constructed by spatially varying the post cross-sections across the aperture, a design methodology that has been validated for a wide range of applications from lensing to holography and beyond [7, 11, 23].

High-contrast metasurfaces also support a variety of optical resonances that dramatically enrich their spectral response. When the meta-atom structure is perturbed away from a high-symmetry configuration, modes that were formerly decoupled from free-space radiation, such as guided mode resonances (GMRs) and quasi-bound states in the continuum (q-BICs) become accessible to an incident field [24, 14, 15]. These resonances are characterized by high quality factors (Q-factors) and strong electromagnetic field enhancements in and around the nanostructures. The Q-factor is continuously tunable through the degree of symmetry breaking in the unit cell, offering direct and independent control over the spectral linewidth of the resonance while its central wavelength can be independently adjusted through the lattice geometry [25, 26, 14]. This precise spectral engineering makes high-Q resonant metasurfaces particularly attractive for biosensing [27, 25, 26], nonlinear optical interactions, spectral filtering, and mechanically reconfigurable metasurfaces. Chapter 3 of this thesis discusses the use of q-BIC resonances for multiresonant optical filters due to the obvious geometric knobs that can control the speactral features of the resonances. Similarly, Chapter 2 covers a NEMS reconfigurable metasurface that utilizes guided slot mode resonance which becomes accessible only through grating-like perturbations to the device geometry for free-space radiation.

Despite these promises, a number of key challenges have limited the deployment of metasurfaces in real systems. First, conventional passive metasurfaces are locked

into a single function at fabrication time, whereas many practical applications demand dynamic, user-programmable optical responses, a requirement addressed by the emerging field of active metasurfaces [28]. Second, single-layer metasurfaces offer a limited design space; achieving multi-spectral, multifunctional, or better performing optical devices generally requires the additional degrees of freedom available only in multilayer or volumetric photonic architectures, yet fabricating high-quality multilayer metasurfaces at visible and near-infrared wavelengths has remained a major bottleneck [29]. The remainder of this Introduction reviews key developments in multilayer and volumetric metamaterials, as well as active and reconfigurable metasurfaces.

1.3 Multilayer and Volumetric Metamaterials for Multifunctionality

Single-layer metasurfaces, despite their impressive capabilities, are constrained by a fundamental limitation in the design space available for a single two-dimensional array of meta-atoms. Achieving simultaneously high transmission or reflection efficiency, broad spectral bandwidth, multifunctionality across several optical degrees of freedom, and high spectral selectivity within a single layer is generally not possible [29]. The most natural route to overcome these limitations is to stack multiple metasurface layers vertically, allowing each layer to contribute an independent degree of freedom to the overall device response [30, 31].

Earlier demonstrations of multilayer dielectric metasurfaces showed that achromatic operation at multiple discrete wavelengths could be achieved by designing separate layers for each color [30]. This strategy was subsequently extended to dispersion engineering, where the sign and magnitude of chromatic aberration in a diffractive lens could be tailored by co-designing two cascaded metasurface layers [32]. More broadly, vertical integration of metasurfaces has enabled wider field-of-view imaging [33], folded optical systems for compact spectrometers [34], multi-wavelength phase control [35], and inverse-designed 3D metmaterials that simultaneously perform multiple independent optical functions [36]. Switching from stacked/cascaded metasurfaces where each metasurface layer is designed for a desired function and combined, to designing metamaterials in 3D all together provided the extra degrees of freedom needed to achieve multifunctional optics. Through advanced optimization algorithms like adjoint inverse design with gradient descent and Adam (Adaptive Moment Estimation), all these degrees of freedom can be iteratively tuned together to optimize the design space for a certain complex optical objective function. Chapters 3, 4, and 5 cover Sb_2S_3 multilayer metasurfaces for multiresonant optical filters,

vertical fiber-to-chip coupling, and visible Bayer color routing respectively.

Despite their promise, multilayer metasurfaces remain far less explored than single-layer designs, primarily due to the lack of a scalable, high-yield nanofabrication platform. With standard CMOS nanofabrication techniques, multilayer metasurfaces would require repeated cycles of lithography, deposition, etch, lift-off processes, which makes the overall fabrication time consuming, high cost and low yield. Several commercially available fabrication platforms aim to reduce process complexity for multilayer structures, including direct laser writing techniques such as two-photon lithography (TPL), as well as imprint-based approaches. Nevertheless, these methods either lack the resolution required for operation in the visible and NIR regimes or restrict the device architecture to a limited set of polymers with relatively low refractive indices for optical applications. In Chapter 3 and 4, we use a precursor based direct e-beam write based fabrication platforms which is integrated into multilayer metasurface fabrication for the first time. Using this fabrication platform, all the other fabrication steps other than lithography, such as deposition, etch and lift-off can be avoided, which makes the overall fabrication quick, low cost and higher yield.

1.4 Active Metasurfaces

While passive metasurfaces have demonstrated a remarkable range of optical functionalities, their fixed optical response after fabrication precludes their use in applications that require dynamic, programmable wavefront control. The realization of active metasurfaces, devices capable of changing their optical function in real time under external stimuli, has therefore become one of the central challenges in the field [28, 37]. Compared to conventional spatial light modulators based on liquid crystals or digital micromirror devices, active metasurfaces offer a potentially compact form factor, a wide field of view, sub-wavelength spatial resolution, and the ability to exploit novel optical modes with no classical counterpart. A large number of tuning mechanisms have been explored in recent years, each with distinct trade-offs in modulation speed, efficiency, power consumption, and compatibility with semiconductor fabrication.

Electro-optic approaches based on transparent conducting oxides (TCOs), such as indium tin oxide (ITO), exploit the epsilon-near-zero (ENZ) effect to achieve large changes in refractive index under an applied voltage [38, 39]. These devices have demonstrated high-speed modulation and, in some implementations, continuous

beam steering, but their efficiency is limited because operation near the ENZ regime is inherently associated with strong free-carrier absorption, and such plasmonic devices are generally limited to operate in reflection. Phase-change materials such as $Ge_2Sb_2Te_5$ (GST) and Sb_2S_3 offer large, non-volatile refractive index changes upon heating, making them attractive for reconfigurable static patterns and logic operations [40, 41]; however, their typically discrete (binary) switching and limited endurance impose constraints on their use as continuously tunable platforms. Liquid-crystal-integrated metasurfaces achieve large and continuous phase modulation with relatively low driving voltages and have been commercialized in devices such as the LiDAR systems, but their modulation speed is typically limited to the kHz range, and achieving uniform liquid crystal alignment over a large metasurface aperture is challenging [42, 43].

Nanoelectromechanical systems (NEMS) offer a complementary set of trade-offs that are particularly well-suited to metasurface tuning. Prior demonstrations have largely relied on suspended silicon bars [44, 45, 46, 47], whose suspension allows large displacements but introduces fragility and low fabrication yield due to the absence of a supporting substrate. Chapter 2 of this thesis proposes and computationally investigates an on-substrate architecture that addresses these limitations while preserving high optical performance using highly confined guided slot mode resonances that are highly sensitive to mechanical displacement.

Beyond the NEMS and electro-optic platforms, several other tuning approaches merit mention. Two-dimensional materials such as graphene and transition metal dichalcogenides (TMDs) offer strong light-matter interactions in atomically thin layers and can be gated to achieve significant modulation of optical absorption and phase, particularly in the mid-infrared and at cryogenic temperatures [48]. Photonic cavities and microresonators integrated with all-optical excitation have demonstrated high-speed amplitude modulation using photoexcited free carriers, at the cost of additional optical pump complexity [49]. Thermally tunable metasurfaces exploit the large thermo-optic coefficients of materials such as silicon or vanadium dioxide [50] near their phase transition temperature to achieve passive temperature-dependent modulation, though the slow thermal response and global (rather than pixel-level) tuning typically limit their utility for wavefront control.

Across all these platforms, the fundamental challenge is the same: maximizing the achievable modulation depth (both amplitude and phase) per unit of applied stimulus, while maintaining low optical loss, high spatial resolution, and compatibility with

standard photonic fabrication processes. The resonant enhancement provided by high-Q optical modes, such as GMRs, q-BICs, slot modes, or hybrid resonances, is a general strategy for amplifying the sensitivity of the optical response to small physical perturbations, and therefore unifies the design philosophy of the active devices presented in Chapters 2 of this thesis.

1.5 Thesis Outline

The central goal of this thesis is to develop active and multilayer metasurface platforms and to demonstrate their potential across a range of photonic systems. The thesis is organized as follows.

Chapter 2 proposes and computationally investigates nano-electromechanically tunable dielectric metasurfaces based on slot-mode resonances at telecom wavelengths. An on-substrate architecture using high-aspect-ratio doped silicon slabs circumvents the mechanical fragility of prior suspended designs, while achieving beam steering with high efficiency. Chapter 3 introduces a high-throughput direct-write electron-beam lithography platform where Sb_2S_3 patterns can be created in situ, during lithography without any pattern transfer through hard mask deposition and etching. Using this platform, three-layer q-BIC–derived optical filter devices with independently tunable resonance wavelengths and linewidths are designed and experimentally demonstrated for compressive hyperspectral reconstruction applications. Chapter 4 applies the Sb_2S_3 direct-write platform to the problem of fiber-to-chip coupling in integrated photonics. An augmented two-layer grating coupler is optimized using adjoint inverse design and the Adam stochastic gradient optimizer, achieving vertical coupling with a high efficiency while imposing no modification whatsoever on the underlying photonic circuit. Chapter 5 extends the Sb_2S_3 direct-write platform to ten-layer volumetric Bayer color routers operating in the visible spectrum. To our knowledge, this represents the first free-form multilayer meta-optic Bayer color router in the visible spectrum. Chapter 6 presents the design, fabrication, and testing of geometric-phase aberration correction metasurface masks in TiO_2 and amorphous silicon for optical vortex coronagraphs targeting exoplanet detection. Broadband unit-cell optimization is carried out in simulation, and Mueller-matrix polarimetry confirms spatially uniform retardance and high transmission across centimeter-scale devices. The performance sensitivity to fabrication errors is quantified and future directions for broadband improvement are discussed. Chapter 7 describes the design and experimental characterization of a planar a-Si metamirror that stabilizes a Fabry-Pérot cavity enclosing a $YVO_4{:}Yb^{3+}$ crystal intended for microwave-to-

optical quantum transduction. A quadratic reflection phase profile is encoded into a subwavelength pillar array on a distributed Bragg reflector substrate, replacing the role of a concave mirror, which is experimentally confirmed to contribute to a significant improvement in the cavity finesse, approaching the theoretical limit. Finally, Chapter 7 concludes the thesis with summary and outlook.

Chapter 2

NANO-ELECTROMECHANICALLY TUNABLE DIELECTRIC METASURFACES FOR RECONFIGURABLE WAVEFRONT SHAPING

The material in this chapter was in part presented in [51].

Active metasurfaces promise lightweight and compact reconfigurable optics. Among many other reconfigurable architectures, nanoelectromechanical effects are one of the most effective tuning methods. Various nanoelectromechanical implementations have been demonstrated, but they generally rely on suspended structures that lead to mechanical fragility. In this work, we propose and computationally investigate an on-substrate design with high aspect ratio doped silicon slabs that can achieve a near-2π phase response in reflection, utilizing a slot mode at telecom wavelength. An amplitude modulation of 80% and a phase modulation of 1.4π can be achieved within 10V. By adjusting the voltage configuration, switchable beam steering can be achieved reaching up to 58% efficiency utilizing a back-mirror. Beam steering with up to 42% efficiency can be performed by eliminating the back mirror, with the added advantage of easier fabrication. This work paves the way for a solid-state nano-electromechanical platform for amplitude and phase modulation, wavefront shaping, and beam steering.

2.1 Introduction

Metasurfaces are flat optical devices composed of arrays of subwavelength scatterers that enable precise spatial control of optical fields in amplitude, phase, and polarization [3, 1, 4]. They hold great promise in replacing traditional bulky optical components across many applications that use free space optics, including lensing [52, 23, 7], holography [9, 8] and spectroscopy [10]. Conventional passive metasurfaces are inherently constrained by their fixed optical functionality, established during the fabrication process. In contrast, active metasurfaces [28] offer the flexibility to create tunable devices, responding to user-defined stimuli such as electrical gating [38, 39], phase-change materials [40, 41], liquid crystals [42, 43]. Among all these tuning mechanisms, there has been an increasing interest in nano-electromechanical/microelectromechanical systems (NEMS/MEMS) [53, 54, 55]. Although NEMS/MEMS had first been developed for transistor-based electronic ap-

plications [56, 57], they proved to be promising platforms in optics as well, to achieve ultra-compact, low power consumption and highly tunable metasurfaces [57, 58]. There is growing attention towards active metasurfaces in general due to the rise in interactive and feedback-based technologies such as augmented and virtual reality (AR/VR), light detection and ranging (LIDAR) and optical communication [37].

Despite the advantages of the NEMS platform, the optical response sensitivity needs to be improved due to the short distance induced by the mechanical actuation. There are different ways of increasing the tunability of active metasurfaces such as operating near resonances that have a moderately high quality factor (Q-factor) in addition to confining and amplifying the electric field by designing the device to employ certain optical modes. In integrated photonics, slot modes have been used to confine light in narrow and low refractive index spaces to amplify the electric field due to the continuity of the electric displacement field [59]. Slot modes are promising candidates for various applications [60, 61, 62] including NEMS/MEMS [47] as they can increase the sensitivity to the electromechanical stimuli because of the amplified electric field in the low refractive index medium.

In this paper, we propose nano-electromechanically tunable metasurfaces based on slot mode resonances at telecom wavelengths. Utilizing high aspect ratio silicon slabs that can bend towards each other on a substrate, we computationally demonstrate a potentially robust device that can cover large areas and have a higher fabrication yield compared to similar architectures using suspended bars [47, 46, 44, 45]. An amplitude modulation of 80% and a phase modulation of 1.4π can be achieved within 10 V. The proposed design can perform a near-2π phase response without the help of a back mirror due to utilization of tall structures whereas most of the previous work had to utilize back mirrors to achieve a strong phase response [47, 63]. Consequently, the proposed design constitutes a good candidate for phase modulation and wavefront shaping whereas the aforementioned suspended architectures lack that ability. As a proof of concept, beam steering can be achieved computationally reaching up to 58% efficiency with the help of a back mirror. On the other hand, it can be performed by eliminating the back mirror up to 42% efficiency but with a much less complicated fabrication.

2.2 Results and Discussion

The system being proposed consists of doped silicon slabs (device layer) connected to different contact electrodes, laying on a substrate layer (silicon dioxide/silicon) as

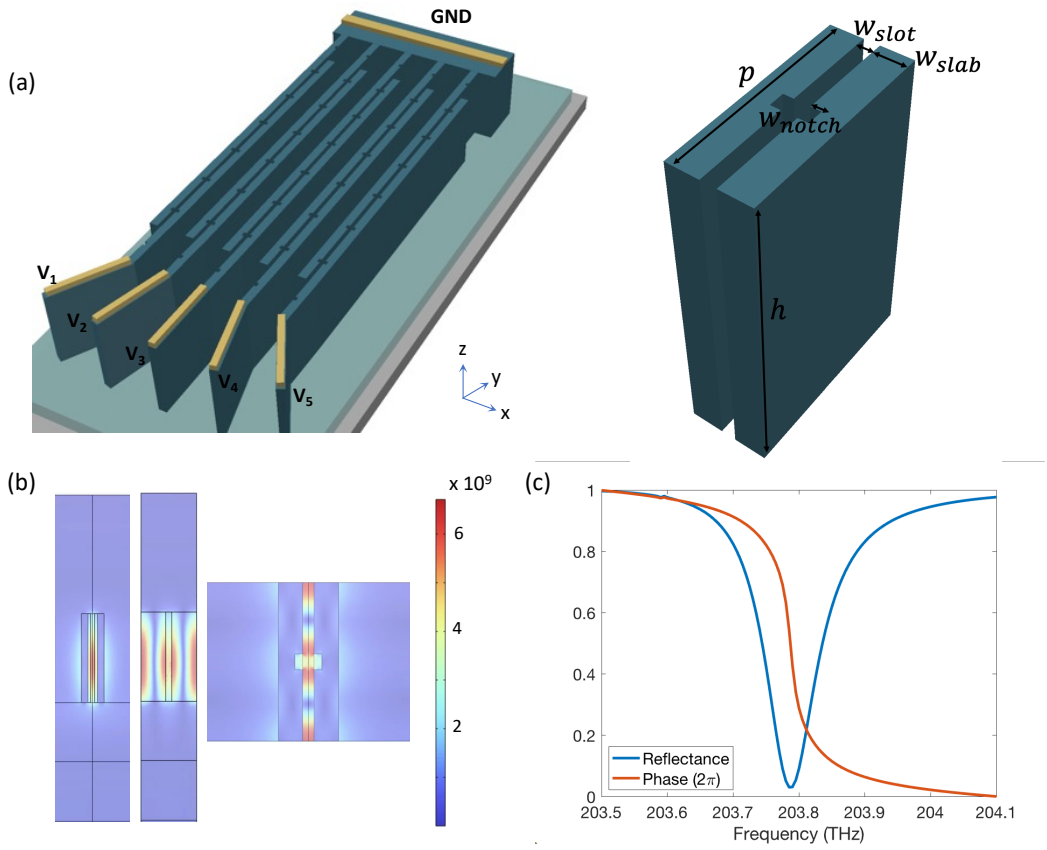


Figure 2.1: **NEMS metasurface architecture and slot mode characteristics.** (a) The overall device design where the slabs that have GND are all connected to the same electrode and the other slabs are connected to independent contacts on the left. The unit cell and the device parameters are shown on the right (b) The slot mode electric field profile (electric field norm) from front, side and top view (left to right). (c) The reflected power and phase of the fully periodic and un-deformed device (no applied voltage) that shows a critically-coupled resonance.

in a silicon-on-insulator (SOI) wafer setting (Figure 2.1.a). The voltage difference between the slabs in a unit cell leads to Coulomb forces that cause the slabs to attract each other, resulting in a bending motion where the bottom of the slabs is fixed on the substrate and the maximum displacement occurs at the tips of the slabs. The device layer is preferred to be doped to optimize the Coulombian attraction by transferring voltage applied to the slabs. By adjusting the amount of bias voltage applied, we adjust the amount of slab displacement. Therefore, the slot width and shape can be altered, which has a direct effect on the wavelength of the slot mode resonance that the device is designed to host. There has been previous research for similar architectures that involve suspending silicon bars to increase displacement

per applied voltage [47, 46, 44, 45]. Nonetheless, these devices exhibit mechanical fragility and encounter challenges related to low fabrication yield, primarily arising from the constraints inherent to their suspended structural configurations. In this paper, the architecture is proposed to be on-substrate to address these issues, and high aspect ratio slabs are utilized to counterbalance the displacement limitations imposed by their attachment to a substrate.

The electric field is enhanced and confined in the narrow and low refractive index region (the air slot) in between the slabs, creating a slot mode due to the continuity of the electric displacement field and high refractive index contrast [64], as opposed to a slab mode where the electric field is mostly inside the high refractive index slab region [65]. The gap between the neighboring slabs within the same unit cell has been intentionally kept under 100 nm in order to utilize slot modes (Figure 2.1b) and maximize the amplitude of electrostatic force. Slot modes have been extensively used in integrated optical devices [64, 66, 67], however, free-space coupling is not possible without introducing any perturbations due to momentum unmatching. Similar to the idea behind the grating coupler, free-space coupling is achieved through periodic perturbations (notches) as can be seen from the device diagram (Figure 2.1.a) to satisfy momentum conservation from air to silicon [63]. The period of the notches (p) is chosen such that the device is coupled to the slot mode at the telecom wavelength λ, using the grating equation for normal incidence $n_{\text{eff}} = \lambda/p$, where n_{eff} is the effective mode index of the slot mode without notches at wavelength λ.

Unit Cell Design

The unit cell is designed to host a slot mode at telecom wavelengths and is composed of two long slabs (simulated as infinitely long) that are separated by a narrow air gap (slot). Employing periodic boundary conditions, our simulations reveal that in its undeformed state (i.e., with no voltage applied), the unit cell hosts a critically coupled resonance characterized by a 2π phase response (Figure 2.1.c). The silicon slabs are oriented along the y-direction, while x-polarized incident light is introduced from the $-z$ direction, coupling to the slot mode (Figure 2.1.b). Having precise control over the slot's width and shape makes it practical to use the slot mode, as the electric field predominantly resides within this region, where mechanical displacement yields maximum perturbation. Therefore, even minor changes in slot parameters can induce significant spectral shifts and enable effective amplitude and phase modulation in reflection. The current unit cell design (Figure 2.1.a) has a

750 nm lattice size (w_l) and 1.5 μm tall slabs with 50 nm notch depth (w_{notch}), 75 nm slot width (w_{slot}) and 160 nm slab width (w_{slab}). An amplitude modulation of 80% (Figure 2.2.a-b) and phase modulation of 1.4π (Figure 2.2.c-d) can be achieved within 10 V using the current unit cell design. The parameters of the unit cell have been chosen based on how the characteristics of the device such as the coupling strength, Q factor, effective refractive index, phase coverage and tunability, change with varying device parameters. The device parameters include the notch depth, slot, slab and lattice size as they are defined in Figure 2.1.a, a detailed analysis of which will be provided in subsequent sections of this manuscript.

Coupling to the slot mode is achieved by introducing perturbations to the slabs through notches. Therefore, the notch size (notch depth and width) affects the Q factor of the resonator as well as the coupling strength to the slot mode. From a fabrication perspective, the feature sizes are much smaller, and the spatial frequency is much higher in the x-direction, so it is easier to make small changes in the notch depth compared to the notch width. Therefore, this change has been examined by keeping the notch width constant at 100 nm and varying the notch depth (w_{notch})

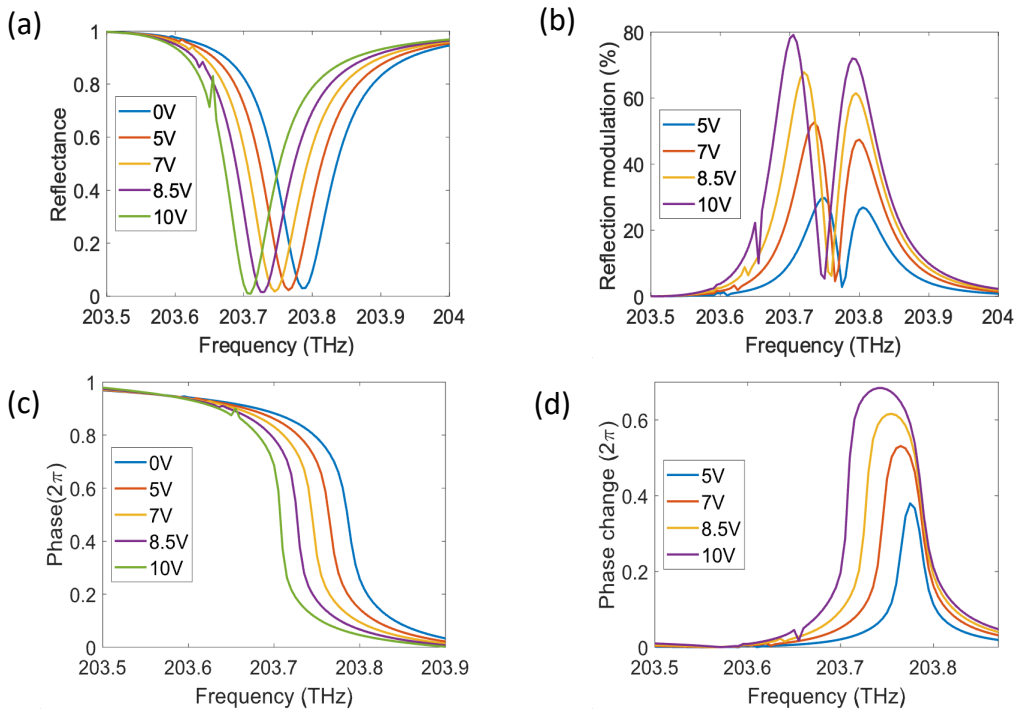


Figure 2.2: **Amplitude and phase modulation under applied voltage.** Reflection (a) and reflected phase (c) for 0,5,7,8.5,10 V, and reflection modulation (b) and phase modulation (d) for 5,7,8.5,10 V.

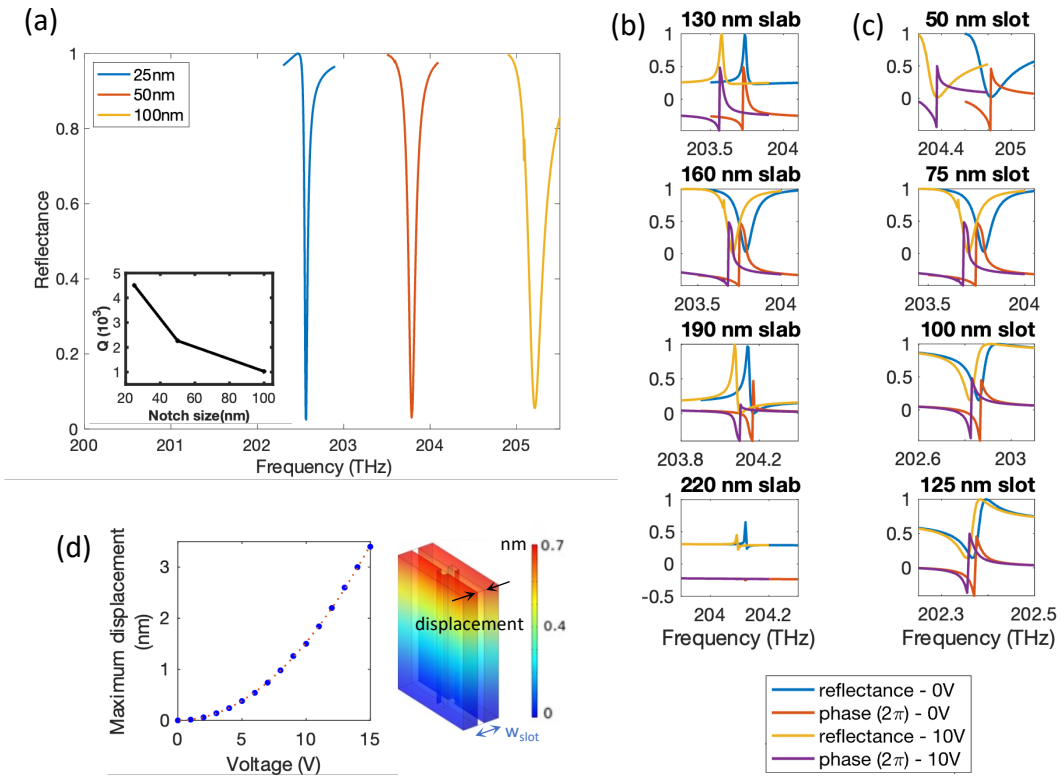


Figure 2.3: **Dependence of optical response on slab, slot, and notch parameters.** (a) The reflectance spectra for w_{notch} = 25, 50 and 100 nm for w_{slab} = 160 nm and w_{slot} = 75 nm. The change in the Q-factor w.r.t. w_{notch} is given in the inset. (b) Reflected power and phase for 0V and 10V for 130, 160, 190 and 220 nm w_{slab} (w_{slot} = 75 nm and w_{notch} = 50 nm). Legend is given both for panels b and c. (c) Reflected power and phase for 0V and 10V for 50, 75, 100 and 125 nm w_{slot} (w_{slab} = 160 nm and w_{notch} = 50 nm), with Q-factors 525, 2.264×10^3, 2.705×10^3, 6.745×10^3 respectively. (d) The schematic shows the displacement in the slabs in nm.

(w_{slot} = 75 nm, w_{slab} = 160 nm, h = 1.5 μm, w_l = 750 nm). As illustrated with 25, 50 and 100 nm deep notches (w_{notch}) (Figure 2.3.a), the Q factor of the resonator decreases with the increasing notch depth, and the coupling strength increases. As the amount of perturbation (the notch depth, w_{notch}) increases, the coupling to the slot mode gets stronger and the slot mode resonance transitions from critically coupled to slightly overcoupled as can be seen from the reflection spectra (Figure 2.3.a). The tunability figure of merit (FoM) which is defined here as the ratio of the shift in resonance frequency and the full width at half maximum (FWHM) of the resonance, is proportional to the Q factor and it decreases with an increase in the notch depth (Figure 2.4.a). Therefore, the notch depth (w_{notch} = 50 nm) is kept small enough to have a large Q factor and tunability, and at the same time large enough to

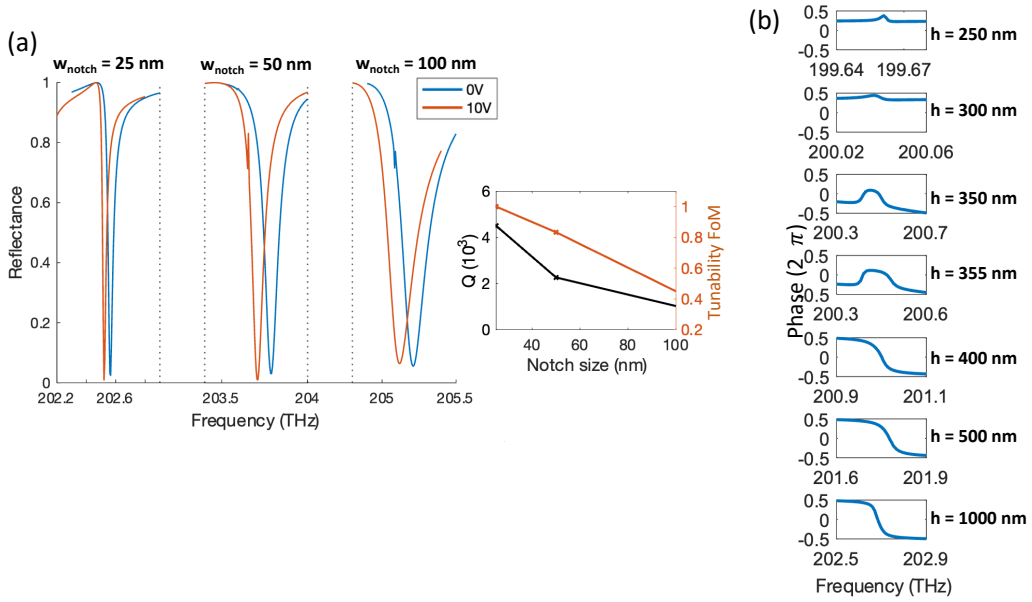


Figure 2.4: **Effect of notch depth and thickness on Q-factor, tunability, and phase coverage.** (a) The shift in the reflectance spectrum for 25 nm, 50 nm, 100 nm w_{notch} for 0V and 10V applied. The dependence of the Q-factor and the tunability FoM (frequency shift/FWHM) on w_{notch} for w_{slab} = 160 nm and w_{slot} = 75 nm is given on the right (b) Reflected phase for h = 250, 300, 350, 355, 400, 500 and 1000 nm respectively in units of 2π.

have a high coupling strength not to compromise the near-2π phase coverage.

Since high aspect ratio slabs are utilized to maximize the amount of slab bending, the proposed design can easily perform a near-2π phase response without the help of a back mirror as opposed to similar previous architectures [47, 63]. This can be achieved with the right set of parameters since 1.5 μm tall silicon bars have a large enough propagation distance to provide a strong phase delay. Previous work [47, 44, 45] was not able to achieve this strong phase response without using a back-mirror due to the mirror symmetry in the z-direction of the suspended structures. The fact that the high aspect ratio slabs lay on the bottom oxide layer in this work, plays a role in breaking the z-symmetry to achieve this [46]. Using the same parameters as the design, when the height of the bars is varied, one can see that the phase response of the resonator gets progressively stronger with the increasing height of the slabs which settles around 500 nm height (Figure 2.4.b) while the other parameters are preserved (w_{slot} = 75 nm, w_{slab} = 160 nm, w_{notch} = 50 nm, h = 1.5 μm, w_l = 750 nm). Given that our design features even taller slabs, it becomes evident that these structures can

indeed achieve near-2π phase response without relying on a back mirror, potentially affording a much easier fabrication process.

As for the slab parameters, when the slab thickness (w_{slab}) is varied while keeping all the other parameters the same (Figure 2.3.b), one can see that the slabs should be on the thinner side to achieve near-2π phase response and higher tunability (w_{slot} = 75 nm, w_{notch} = 50 nm, h = 1.5 μm, w_l = 750 nm). However, it is imperative to exercise caution, as excessively thin slabs result in an effective refractive index of the overall mode that becomes impractically small. In the context of our design objectives, this index should ideally exceed the refractive index of SiO_2 to prevent undesirable leakage of the slot mode into the substrate, a criterion that we find to be met with a slab thickness of w_{slab} = 160 nm. In addition, the background reflection is high when w_{slab} = 160 nm compared to w_{slab} = 130, 190 and 220 nm. Coming to the slot parameters, as shown in Figure 2.3.c, the Q-factor of the resonator increases with an increase in the slot size. However, as opposed to the effect of the Q-factor on the tunability when changing the notch depth, we can see here that the tunability does not have a direct relationship with the Q-factor. Although the Q-factor decreases with the decreasing slot size, the effective change in the unit cell geometry, which is defined here as the ratio of the mechanical displacement and the slot size (w_{slot}) is larger compared to the case where the slot size is larger. It varies as maximum displacement of 3.4 nm for 50 nm slot, 1.5 nm for 75 nm slot, 0.84 nm for 100 nm slot and 0.56 nm for 125 nm slot for 10 V (Figure 2.3.d). Both the total displacement and the effective change in the slot size (the ratio of the total displacement and the slot size (w_{slot})) decrease with the increasing slot size (for more details regarding the mechanics, please see Supporting Information: Mechanics of the Architecture). Considering that the tunability is not proportional to the displacement but the effective displacement, narrower slots result in higher tunability, as long as they also provide a high enough Q-factor, which motivates us to find a sweet spot for the slot size (w_{slot} = 75 nm).

Device Design

Beam steering can be effectively realized through the emulation of the phase profile characteristic of a blazed grating, albeit in a discretized manner, enabling the precise optimization of power directed into a specific diffraction order. This controlled 0 to 2π phase gradient can be systematically achieved by selecting a suitable number of discrete steps. In the context of our beam steering design, we opted for a configuration featuring four phase steps, each separated by a $\pi/2$ difference. Moreover,

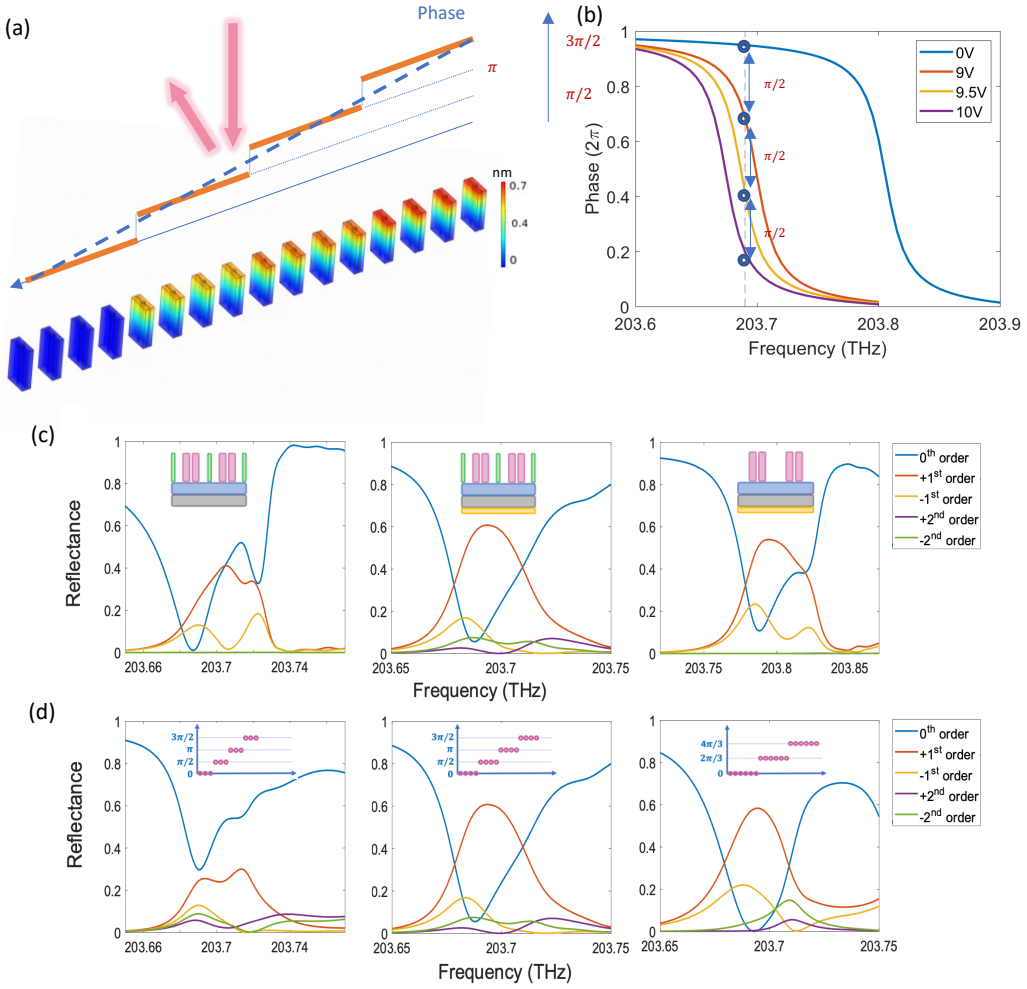


Figure 2.5: **Beam steering and steering efficiency optimization.** (a) Sampling the phase ramp at 4 points to achieve beam steering into +1st order. The coloring used on the slabs represent the amount of displacement that they perform for 0V, 9V, 9.5V and 10V in groups of four unit cells. (b) The library used when designing the beam steering device: 0V, 9V, 9.5V and 10V bias voltages correspond to the 4 phase points with $\pi/2$ separation on the 0 to 2π phase ramp. (c) The optimal voltage configuration in terms of steering efficiency (4 phase steps and each step is made out of 4 cells) when there is no gold mirror but isolating walls, when there are both gold mirror and isolating walls, when there are no isolating walls but a gold mirror (from left to right). (d) The reflectance given for 4 phase steps that are made out of 3 cells (5.1 deg of steering angle), 4 phase steps that are made out of 4 cells (3.8 deg of steering angle) and 3 phase steps that are made out of 6 cells (3.4 deg of steering angle) (from left to right), all utilizing isolating walls and back-mirror.

for the optimal design, each of these phase steps is meticulously constructed using four individual unit cells (Figure 2.5.a). Using the library shown in Figure 2.5.b, to achieve the phase steps with $\pi/2$ jumps, 0 V, 9 V, 9.5 V and 10 V are applied to the four groups of cells. Here, even 0.5 V jumps result in $\pi/2$ phase increments due to the quadratic relationship with the maximum slab displacement and applied voltage demonstrated in Figure 2.3.d.

The optimal scenario entails the utilization of a single unit cell for each phase step, affording the advantages of reduced pixel size and expanded steering angles. The electric field amplitude at the edge of the unit cell is 10–15 times smaller than the maximum electric field amplitude (the center of the slot) (Figure 2.1.b) for different parameters. However, there is still significant crosstalk between the adjacent unit cells observed since the electric field is not perfectly localized in the narrow slots which results in the loss of addressability of the individual antennas [63]. This argument is supported by quite low steering efficiencies when there are one to two unit cells per phase step. The crosstalk between the adjacent unit cells becomes less and less important for the overall gradient when there are more cells for each phase step, and the diffraction efficiency into the +1st order increases significantly with respect to −1st order.

To reduce the crosstalk, a few strategies are utilized: The lattice size is increased from 750 nm to 1400 nm in order to enlarge the spacing between adjacent pairs of cells. 60 nm wide isolating walls are introduced to each unit cell as in previous work [63] to suppress coupling between the neighbor cells. A direct comparison between the last two plots presented in Figure 2.5.c demonstrates the favorable impact of these isolating walls, manifesting as an increase in the steering efficiency from 43% to 58%. We define the beam steering efficiency here as the difference between the reflectance of the +1st order and −1st order. Improving the final steering performance without reducing the crosstalk is also explored using a 100 nm thick gold back mirror that keeps the reflection amplitude almost uniform by eliminating the transmittance channel. Although there is no need to use a mirror for achieving a strong phase, uniform reflected amplitude helps increase the efficiency from 42% to 58%, comparing the first two plots of Figure 2.5.c.

As mentioned earlier, each phase step in the phase gradient is formed out of multiple cells to diminish the pronounced crosstalk effects. This phenomenon is readily evident when comparing the first two plots presented in Figure 2.5.d, which exhibit identical phase gradient sampling but differ in the number of cells sharing the

same phase delay. However, a higher number of overall cells does not guarantee a better performance all the time. Both how large each phase step is represented in the metasurface and how smooth the phase gradient is sampled influence the steering performance. In Figure 2.5.d, the last two plots show that an 18-cell pixel is outperformed by a 16-cell pixel device since the latter has a smoother phase profile despite having a smaller number of cells.

While different voltage configurations yield varying steering efficiencies, altering the applied voltage setup also allows for the adjustment of the device's steering angle. Among the configurations explored thus far, the one exhibiting optimal steering efficiency (characterized by a pixel size of 4 and featuring 4 phase steps) has yielded a steering angle of 3.8 degrees with an accompanying efficiency of 58%. This angle can be enlarged at the expense of efficiency as in the case of the 12-cell pixel device that can go up to 5.1° with 32% efficiency. By sacrificing some of the efficiency, it is also possible to make these devices without a back mirror with a much simpler fabrication.

Compared to its counterparts using suspended platforms, the on-substrate architecture proposed in this paper is expected to be more mechanically robust and have larger device apertures due to the difference in the fabrication abilities. The suspended structures surrounded by air are not the best candidates for phase modulation and wavefront shaping applications either. The z-symmetry they have hinders overcoupling as it is hard to support the coupling through one radiation channel in such platforms. On the other hand, the on-substrate architecture breaks this symmetry simply by using a substrate and high aspect ratio structures. Therefore, reported modulation values exceed both intensity and phase modulation reported in [44].

2.3 Conclusion

In this article, we propose nano-electromechanically tunable metasurfaces based on slot mode resonances at telecom wavelengths. Using this device, an amplitude modulation of 80% and a phase modulation of 1.4π can be achieved within 10 V. By changing the voltage configuration and therefore the phase delay each cell imposes onto the input field, this device can be tuned to achieve any kind of wavefront shaping in principle. To exemplify that, a beam steering voltage configuration has been demonstrated reaching up to 58% efficiency with the help of a back-mirror as well as 42% efficiency by eliminating the back mirror with a much less complicated fabrication.

While prior proposals have explored similar architectures, they often relied on suspended bars to maximize the inter-bar distance change. However, this approach came at the expense of mechanical fragility and limited fabrication yield, which motivated the transition to an on-chip design, employing slabs with higher aspect ratios. Our proposed system entails elongated silicon bars paired with narrow slots, designed to host slot modes at telecom wavelengths. We systematically investigate the impact of various device parameters on a spectrum of optical characteristics, elucidating the rationale behind our parameter choices. This design can achieve a strong phase response due to using tall silicon bars that have a larger propagation distance, which potentially eases the fabrication compared to the previous work that utilized back-mirrors. Using this unit cell design and modifying it in order to reduce the crosstalk between the cells using strategies such as enlarging the lattice and adding isolating walls, a beam steering configuration is proposed. The optimal steering efficiency (58%) has been shown by sampling 0 to 2π phase ramp at 4 points and using 4 cells for each sample point. The steering angle of the optimal voltage configuration in terms of efficiency has been shown at 3.8 degrees of steering angle because of the large pixel size due to the effort made to reduce the coupling between the adjacent cells. This steering angle can be altered by changing the voltage configuration and therefore the effective pixel size, but with varying steering efficiency. This performance is either on the same order or better compared to other beam steering devices in the literature which are mostly liquid crystal (LC) based [68] such as LC optical phase arrays (OPAs) which achieve approximately 58% diffraction efficiency within $\pm 5^\circ$ range [69, 70] or compound blazed gratings that can achieve around 40% efficiency for 0–2.3° steering angle [71].

Although considerably high aspect ratio gratings have been demonstrated so far in experiment, especially for X-ray imaging [72, 73, 74] going up to 200:1, the proposed design which has trenches of different widths (slots and the gaps between unit cells) makes the fabrication more challenging without optimizing a high aspect ratio etch recipe. The etch rate of slots has been observed to be lower than that of wider gaps in our experimental attempts (see Supporting Information: Experimental Attempts), which results in overetching/undercutting of the slab pairs whereas the slots are not fully etched during an inductively coupled plasma reactive ion etching (ICP-RIE) pseudo-Bosch process. On the other hand, aspect ratios as high as 60:1 have already been achieved for nanoscale structures such as nanowires [75] and gratings [76]. Therefore, it is feasible to successfully fabricate the proposed structures by process engineering: optimizing the etchant and passivation gas amount and ratio, ICP

and forward power [75]. Our numerical results pave the way for a solid-state NEMS platform in amplitude and phase modulation, wavefront shaping and beam steering, and therefore for numerous applications like AR/VR, LIDAR and optical communication.

2.4 Methods

Simulation

The reflected spectra of the metasurface were computed utilizing the commercial software COMSOL, which employs the finite element method (FEM). For the calculation of the effective refractive index of the slot mode, we employed 2D simulations to calculate the notch period (p), while 3D simulations were employed for all other aspects of our analysis. 3D simulations can be examined under electrical, mechanical and electromagnetics categories. For both 2D and 3D simulations, the unit cell was represented as the silicon slabs with notches (Figure 2.1.a, right panel) on top of silicon dioxide/silicon. 1.5 μm/3 μm thicknesses are used for silicon dioxide/silicon substrate for part I of the manuscript where it is reduced to 1 μm/1 μm for part II to reduce the simulation time since the reflected power and phase are not significantly affected by that change.

To simulate the application of a bias voltage to the silicon slabs, we employed the Electrostatics physics interface (PI). In this simulation, the entire slab was designated as a terminal for both ground (GND) and voltage (V) contacts, assuming the loss in the doped silicon slabs is negligible due to low resistivity and small distances. To enable the deformation of the slabs, we incorporated the Solid Mechanics PI within the region corresponding to the slabs. Surface attachment was represented through the imposition of fixed constraints at the lower surface of the slabs. The unit cell's box shape was preserved by prescribing a displacement of zero in the y-direction, an option readily available in Solid Mechanics.

To establish a connection between Electrostatics and Solid Mechanics and subsequently calculate the slab displacement arising from the applied voltage difference, we harnessed the capabilities of the Multiphysics PI. Subsequently, the deformed mesh was exported, and electromagnetic simulations were performed on these deformed meshes to compute the reflected spectra resulting from the application of a bias voltage.

For our electromagnetic simulations, we deployed the Electromagnetic Waves, Frequency Domain PI. These simulations featured a periodic input port, which received

normally incident, x-polarized input fields, as well as a periodic output port. Floquet periodic boundary conditions were applied to the lateral sides of the simulations, ensuring an accurate representation of the metasurface's behavior.

2.5 Appendix

Experimental Attempts

The proposed design with the given parameters is feasible to fabricate once a high aspect ratio etch process is optimized. During our optimization attempts, the etch rate was different for narrow slots and larger gaps between the unit cells which resulted in the underetching of the narrow slots (Figure 2.6.a) although we were able to fabricate notches with accurate size and period (Figure 2.6.b). However, when we etch more to compensate for that, the slab pairs in the same unit cell start to get undercut together and detach from the substrate even for the lower Q designs we had with 130 nm slot width. When we take a FIB cross-section of the structures,

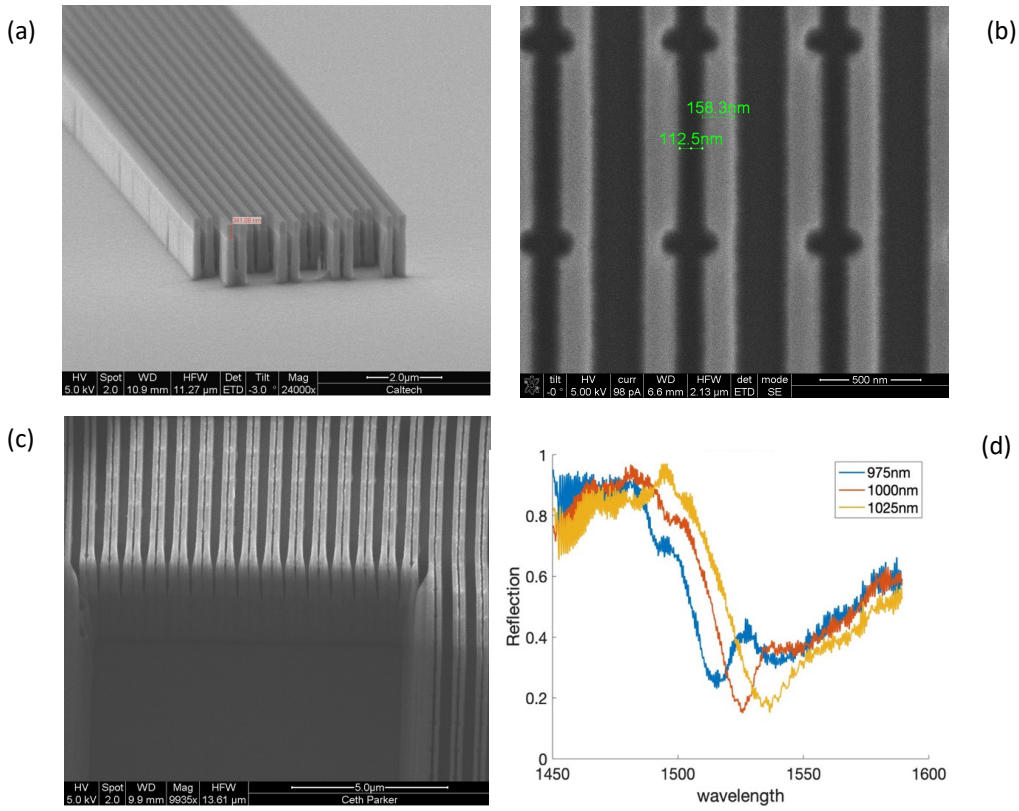


Figure 2.6: **SEM characterization and experimental slot mode coupling.** (a) Tilted SEM view of test structures. (b) Top view of the slots, slabs and notches. (c) FIB cross-section of the structures. (d) Slot mode resonance for notch periods 975 nm, 1000 nm and 1025 nm.

although the slabs are deformed due to ion bombardment, we can still see that the slabs are not separated from each other at the bottom and therefore, the electrical isolation fails (Figure 2.6.c).

We confirm that we can experimentally couple to the slot mode from the experiments done with different notch periods. Figure 2.6.d shows that as the notch period we fabricate changes, the slot mode resonance wavelength shifts. Therefore, we can say that our devices can couple to the slot mode intended at telecom wavelengths. Consequently, the failure happens in the electromechanical part of the experiments, not the optical part. To confirm that, we designed and fabricated (using the same etching techniques and recipe) that have the same gap size everywhere across the device (the slots and the gaps between the unit cells) without the notches so that there is only one slab in the smallest periodic unit (lattice size a). If the structures are electrically isolated, then the lattice size should double (2a) since neighboring bars should be attracted to each other and diffraction pattern of these grating should change significantly. We built a simple optical setup to observe the Fourier plane of these gratings yet observed no changes. Similarly, we tested the original devices on a probe station inside an SEM and saw no mechanical change in the device upon electrical excitation.

Mechanics of the Architecture

One limiting factor of this platform is the pull-in limit which is a well-known phenomenon in electrical engineering and MEMS world. Pull-in occurs when the capacitor plates that are d apart from each other are attracted to each other by d/3. For our structures that are separated by 75 nm slots, Figure 2.7.a shows that

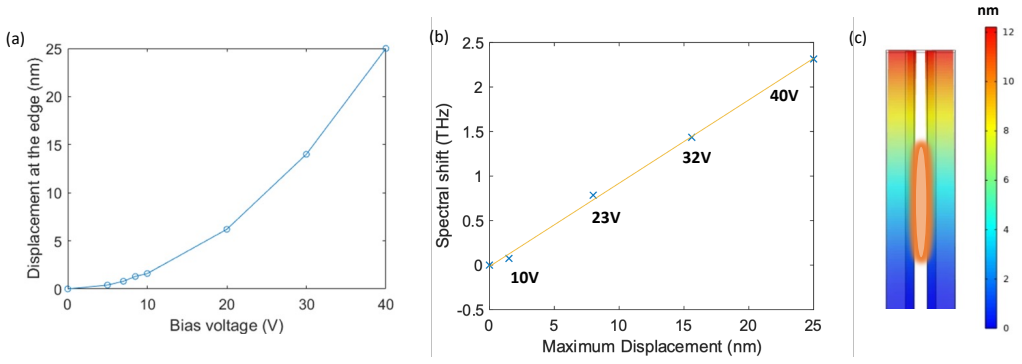


Figure 2.7: **Mechanical response and spectral tuning of the NEMS architecture.** (a) Maximum displacement w.r.t. applied voltage. (b) Spectral shift w.r.t. maximum displacement. (c) Slab movement chart and the region where the slot mode resides.

we can apply voltages up to 40 V. One can question whether this would result in dielectric breakdown of the air and device breakage. However, experiments show that dielectric breakdown for small dimensions does not follow the Paschen curve and even 10^{-3} atm.mm has a breakdown voltage more than 1 kV [77].

The maximum displacement changes quadratically with the applied voltage (Figure 2.7.a). As for the relationship between the amount of attraction (maximum displacement of the slabs towards each other) and the modulation, Figure 2.7.b shows that spectral shift of the resonance changes linearly with respect to the attraction (maximum displacement). This seems unexpected at first sight since the bending of the slabs does not increase linearly from bottom to top for higher voltages (it can be approximated as linear for lower voltages). However, we should draw attention to the fact that the majority of the electric field amplitude resides at the center of the slot where the displacement is much smaller than the maximum displacement (Figure 2.7.c). The parts of the slabs that surround the confined electric field move in the approximate range of 0 - maximum displacement/2.

Chapter 3

MULTILAYER Q-BIC-LIKE OPTICAL FILTERS WITH HIGH THROUGHPUT DIRECT-WRITE MULTILAYER LITHOGRAPHY

The material in this chapter was in part presented in [78].

Multilayer metasurfaces provide substantially greater spectral design freedom than single-layer devices, yet their implementation in the visible and near-infrared remains limited by the complexity, cost, and low throughput of conventional nanofabrication. Here, we establish a recently proposed direct-write electron-beam lithography approach as a high-throughput fabrication platform for multilayer resonant metasurfaces, based on an antimony precursor that decomposes in situ into high-index Sb_2S_3. This method eliminates deposition–etch cycles and reduces each layer to only two fabrication steps, enabling efficient realization of multilayer architectures. Using this platform, we demonstrate multilayer q-BIC–derived metasurfaces with independently tunable resonance wavelengths and linewidths, allowing the construction of compact multi-resonant filters with spectrally decoupled layers. We experimentally demonstrate three-layer devices supporting three resonances and show independent control of resonance wavelength and Q factor across layers. Leveraging this capability, we generate decorrelated filter arrays for compressive sensing and hyperspectral reconstruction, achieving sets of 9 and 36 filters with average absolute Pearson correlation coefficients of 0.11 and 0.21, surpassing prior metasurface and photonic-crystal implementations. These results establish a practical route toward scalable multilayer resonant metasurfaces for spectral filtering, on-chip spectroscopy, and computational imaging.

3.1 Introduction

Optical metasurfaces are planar optical devices composed of arrays of subwavelength scatterers that enable precise spatial control of light. While single-layer metasurfaces have demonstrated functionality comparable to that of conventional optical components and more in a compact form factor, more complex and multifunctional objectives such as achromatic responses [30, 79, 80, 81, 31], optical sorting [82, 83, 84, 85, 36], and optical computation [86, 87, 88, 89, 90] require additional degrees of freedom in the design and optimization space. Volumetric

and multilayer metamaterials provide such expanded design freedom [29]. However, this design space remains largely unexplored in the visible and near-infrared (NIR) spectral regimes, primarily due to the challenges associated with fabricating high-resolution three-dimensional and multilayer nanostructures. Conventional nanofabrication workflows which typically involve repeated cycles of deposition, electron-beam or photolithography, etching, and planarization, become increasingly complex, costly, and low throughput when extended to multilayer metasurface architectures. Several commercially available fabrication platforms aim to reduce process complexity for multilayer structures, including direct laser writing techniques such as two-photon lithography (TPL), as well as imprint-based approaches. Nevertheless, these methods either lack the resolution required for operation in the visible and NIR regimes or restrict the device architecture to a limited set of polymers with relatively low refractive indices for optical applications. As a result, despite their promise, multilayer metasurfaces remain far less explored than single-layer designs, primarily due to the lack of a scalable, high-yield nanofabrication platform.

Thermal decomposition of metal–organic molecular precursors has been widely employed to form metal chalcogenide films via post-deposition annealing, particularly in the context of solar cell research [91, 92, 93, 94, 95]. To the best of our knowledge, this chemistry was first adapted for direct-write patterning in Ref. [96], where nanostructures were realized using electron-beam lithography (EBL) and photolithography. More recently, this approach also has been extended to the realization of Fresnel zone plates and metalenses [97]. In this work, we establish this fabrication method as a high-throughput direct-write platform for multilayer metasurfaces, as well as resonant metasurfaces, using an antimony-based organic precursor that decomposes in situ into antimony (III) sulfide (Sb_2S_3). By leveraging this platform, a conventional multilayer nanofabrication process can be simplified to only two steps per layer: direct EBL writing of the spin-coated antimony-based precursor and spin-coating of the planarization layer.

Quasi-bound states in the continuum (q-BIC) metasurfaces have emerged as a powerful platform for realizing high quality factor (Q) optical resonances in subwavelength photonic structures. By perturbing symmetry-protected BIC modes, these metasurfaces enable strong light–matter interactions with precisely engineered radiative coupling, allowing narrow linewidths and large field enhancements to be achieved in compact, planar geometries [98, 14, 15, 99, 100, 101, 102]. Owing to their high spectral selectivity and geometrically tunable Q factors, q-BIC metasurfaces are

promising candidates for constructing filter arrays with directly controllable spectral features for hyperspectral imaging and spectral reconstruction. In such systems, wavelength information is encoded through spectrally decorrelated filters, and the ability to generate low-correlation spectral responses directly determines the reconstruction performance and achievable device compactness [103, 104, 105, 106, 107, 108, 109]. In this work, we design a multilayer q-BIC–derived optical filter architecture with independently tunable spectral features and propose its application to spectral reconstruction and compressive sensing within a compact multilayer metasurface platform.

3.2 Results and Discussion

Fabrication Flow

The fabrication approach employed in this work is a direct-write lithography method in which the exposure-sensitive medium is not a conventional resist, but rather the optical material itself. Direct patterning has been explored as an efficient route for transferring nanoscale features; however, prior demonstrations have largely focused on metals and metal oxides for electronic applications [110, 111, 112, 113, 114, 115], with comparatively limited exploration in optical devices. Thermal decomposition of metal–organic molecular precursors, such as metal–BDCA (butyldithiocarbamic acid) complexes, has been widely employed in solar cell research, where metal chalcogenide films are formed via annealing-induced decomposition of the metal-organic complexes [93, 116, 117, 118, 94]. In particular, antimony-BDCA precursor solutions have been used to produce Sb_2S_3 thin films through thermal decomposition for photovoltaic applications [95, 92, 91]. More recently, it was demonstrated that Sb_2S_3, along with other metal/ semiconductor chalcogenides, can be directly patterned through lithography-induced chemical decomposition of metal/ semiconductor–organic precursors [96]. We focus on Sb_2S_3, selected for its optical transparency and high refractive index in the visible and NIR spectral regimes [119, 120, 121], and establish the Sb_2S_3 direct-write as a fast fabrication approach for multilayer metasurfaces.

This fast multilayer lithography process is based on a solution-processed antimony-BDCA precursor that decomposes into Sb_2S_3 and organic byproducts upon exposure during electron-beam lithography (EBL). Once synthesized, the precursor remains stable for several weeks and can be readily used by spin-coating the liquid solution onto the substrate and directly patterning it into Sb_2S_3 (Reaction 3 in Supporting Information, Precursor Solution Synthesis). In the exposed regions, the precur-

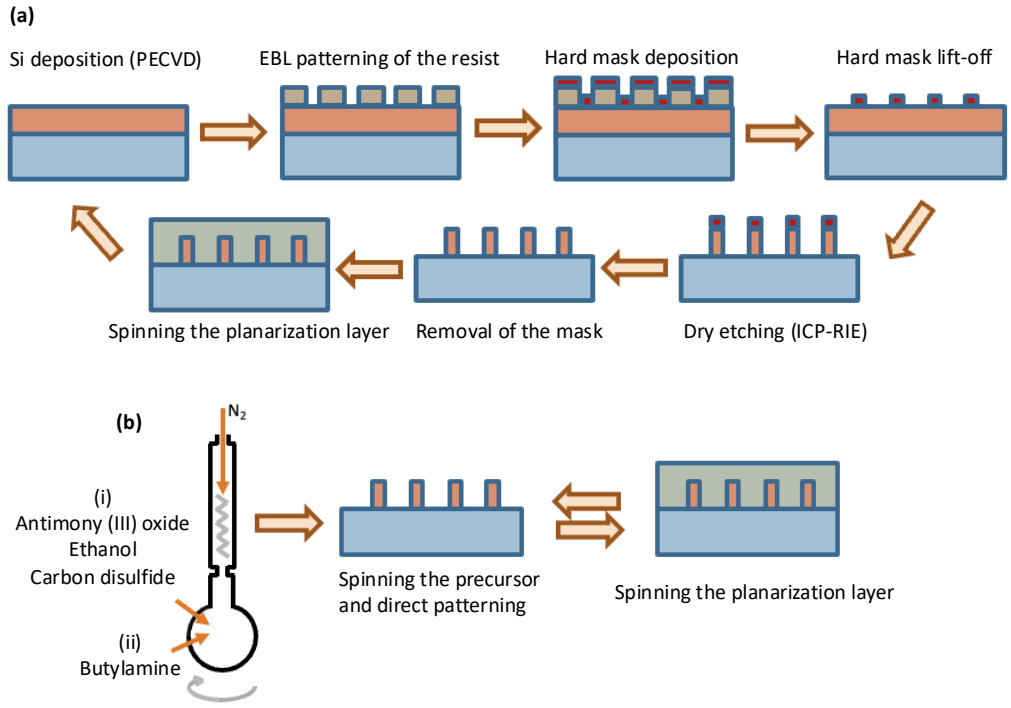


Figure 3.1: **Comparison of conventional nanofabrication and Sb_2S_3 direct-write multilayer fabrication flows.** (a) An example flow of standard nanofabrication processes to fabricate a multilayer metasurface. (b) Proposed Sb_2S_3 direct-write process for multilayer metasurfaces.

sor undergoes in situ conversion into the target chalcogenide material, while the unexposed precursor and organic decomposition byproducts are removed during development by immersing in isopropanol (IPA) (see the details in Fabrication Details section of Supporting Information). For planarization, hydrogen silsesquioxane (HSQ) is employed. HSQ is a negative-tone electron-beam resist that also functions as a spin-on glass owing to the similarity of its chemical composition to that of silica (SiO_2). It is a mechanically robust material with a low refractive index, providing a high refractive-index contrast with the Sb_2S_3 nanostructures. Following planarization, an additional layer of the precursor can be spin-coated, and the direct-write process can be repeated using the same fabrication steps.

This approach eliminates both the material deposition and etching steps for each layer, thereby significantly accelerating the overall fabrication process. For comparison, a conventional multilayer EBL process employing materials such as amorphous silicon (a-Si) and spin-on glass typically involves: (1) a-Si deposition using

plasma-enhanced chemical vapor deposition (PECVD); (2) electron-beam resist spin-coating; (3) EBL exposure; (4) development; (5) hard-mask deposition; (6) hard-mask lift-off; (7) plasma etching; (8) mask removal; and (9) spin-coating of the planarization layer, such as a spin-on glass or a polymer. These steps must be repeated from step (1) for each additional layer (Figure 3.1.a). In contrast, the multilayer process introduced here consists of only four steps per layer: (1) spin-coating of the precursor; (2) EBL exposure; (3) development and annealing; and (4) spin-coating of a planarization layer, after which the process is repeated from step (1) for subsequent layers (Figure 3.1.b). As a result, three time-intensive and costly steps, PECVD, etching, and material deposition, are completely eliminated while the interlayer alignment accuracy is still ultimately limited by the lithographic resolution (below 10 nm).

Device Design and Experimental Results

Compressive sensing seeks to recover an unknown signal from a small number of linear measurements, often obtained through randomized or weakly correlated sensing functions [122]. Because the number of collected measurements is usually much smaller than the signal's dimensionality, the reconstruction problem becomes an underdetermined linear inversion. The quality of the reconstructed signal depends critically on the degree of randomness and mutual incoherence among the basis functions. In the context of spectral reconstruction, this requirement motivates the use of basis elements with diverse spectral responses, encompassing both broadband and narrowband features, in order to enable high-resolution and robust reconstruction performance.

Leveraging our high-throughput direct-write multilayer lithography platform, we design multilayer, multi-resonant optical filters in which each layer comprises q-BIC–derived metasurfaces with distinct resonance wavelengths and Q factors. The patterned Sb_2S_3 layers are separated by spacer layers that are sufficiently thick to ensure minimal interlayer coupling. As a result, an N-layer device provides $2N$ independent degrees of freedom for spectral control, since both the resonance wavelength and the Q factor of each layer can be independently engineered. This expanded design space is particularly advantageous for spectral reconstruction applications. In the following section, we construct a synthetic set of optical filters with low pairwise spectral correlations to quantitatively demonstrate the effectiveness of these high-throughput multilayer optical filters for compressive sensing and reconstruction.

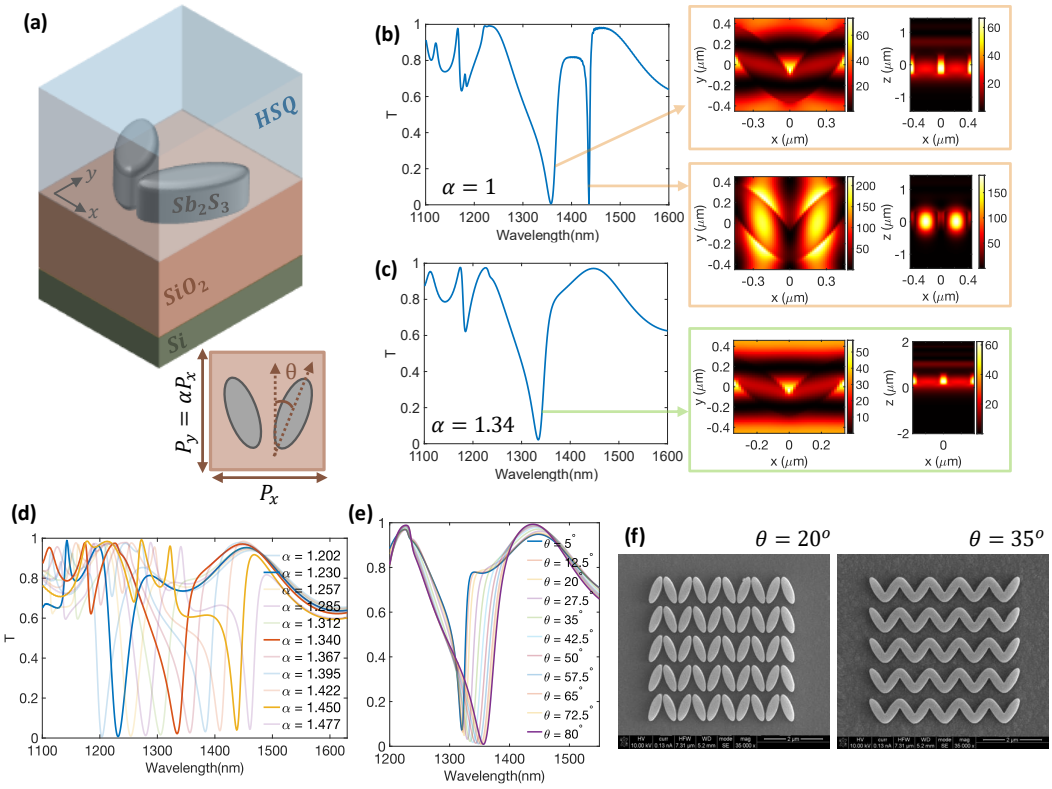


Figure 3.2: **Unit cell design and spectral tuning of q-BIC-derived Sb_2S_3 metasurfaces.** (a) The unit cell of the metasurface made of two Sb_2S_3 tilted posts on top of a 1.3 µm thick SiO_2 spacer on Si substrate and the definition of parameters α and θ. (b) Simulated transmission for the square lattice (α=1, P_y=P_x=887 nm, θ=35°), and the norm of the electric field for the inter-post (top) and intra-post (bottom) modes given in the orange boxes. (c) Simulated transmission for the rectangular lattice (α=1.34, P_x=673 nm, P_y=αP_x=902 nm, θ=35°), and the norm of the electric field for the inter-post mode given in the green box. (d) Simulated transmission shown for θ=35° and α=1.202, 1.230, . . . , 1.477. The solid lines refer to the parameter configurations used in Figure 3.3.b. (e) The change in the resonance linewidth with θ=5°, 12.5°, . . . , 80°. (f) SEM images of the fabricated Sb_2S_3 elliptical posts for θ=20° (left) and θ=35° (right).

The fundamental building block of the metasurface design is a rectangular unit cell with lateral dimensions P_x and P_y, as illustrated in Figure 3.2.a. Each unit cell contains two elliptical Sb_2S_3 resonators with a height of 400 nm, positioned on a 1300 nm thick SiO_2 spacer layer atop a silicon substrate as shown in Figure 3.2.a (see details in Optical Design with FDTD section of Supporting Information). The refractive index of Sb_2S_3 is taken as 2.1 (Chemical and Optical Characterization section in the Supporting Information), and normally incident light is x-polarized. The major axes of the ellipses are rotated by an angle θ with respect to the normal, forming a zigzag-like arrangement across the array. This tilted-ellipse geometry has been widely employed to realize q-BIC resonances and has proven effective in a range of applications including biomolecular sensing, optofluidic manipulation of nanoparticles via enhanced electromagnetic fields, and molecular fingerprint detection [27, 25, 123, 26].

In this design, the resonance wavelength is predominantly controlled by the ratio of the lattice constants P_y and P_x, defined as $\alpha = P_y/P_x$, while the quality factor Q (or equivalently, the resonance linewidth) is controlled by the tilt angle θ. These resonances can be observed in the transmission spectrum shown in Figure 3.2.b and c. Within the explored parameter space, α is varied from 1.147 to 1.587, enabling tuning of the resonance wavelength from 1150 nm to 1550 nm, a subset of which is shown in Figure 3.2.d. Independently, the quality factor is tuned from $Q = 15$ to $Q = 82$ by varying the rotation angle θ between 5° and 80° (Figure 3.2.e). At larger angles, the two elliptical resonators within a unit cell begin to merge (Figure 3.2.f); numerical simulations indicate that this geometric transition does not qualitatively alter the overall evolution of the resonance characteristics.

While the tilted-ellipse geometry supports a single q-BIC resonance when the structure is air-clad, this resonance splits into two distinct modes when embedded in the dielectric environment used here. As shown in Figure 3.2.b, the first mode is localized primarily in the gap region between the resonators, exhibits stronger coupling to external radiation, and therefore possesses a lower Q. The second mode is predominantly confined within the resonators themselves, couples more weakly to out-of-plane radiation channels, and exhibits a higher Q. We refer to these modes as the inter-post and intra-post resonances, respectively.

This resonance splitting arises from the modified dielectric environment relative to the air-clad case, which alters the vertical boundary conditions and redistributes the balance between upward and downward radiation channels [124, 125]. As a result,

the inter-post branch no longer follows the ideal q-BIC behavior in which radiative loss vanishes as the perturbation angle approaches zero. Instead, the modified index loading introduces a residual radiative pathway that produces a finite linewidth even at $\theta = 0°$ (hence the "q-BIC derived" terminology). Although the Q still can be controlled via the rotation-induced perturbations, the presence of this loss channel imposes an upper bound, which is advantageous for practical spectral filtering by improving robustness and signal throughput.

When the lattice is kept square ($\alpha = 1$), both resonances are present within the transmission spectrum (Figure 3.2.b). In contrast, when the lattice is elongated along the y direction ($\alpha > 1$), the intra-post resonance undergoes a blue shift and is pushed outside the operational wavelength band, as shown in Figure 3.2.c. Retaining a square lattice thereby enables a richer spectral response with multiple resonance dips exhibiting diverse features. However, numerical simulations indicate that the quality factor of the intra-post resonances can reach values in the range of $Q \approx 450$–500 (Figure 3.4.c). Experimentally, we find that such high-Q resonances are not supported by the present material platform and fabrication approach, as the high-Q intra-post resonances predicted by simulation do not appear in the measured transmission spectra (Figure 3.4.c and d). Despite this limitation, it is still possible to design devices targeting $2N$ resonances in simulation in order to experimentally realize an effective N-resonance device, a strategy that will be discussed later in this section. While this design methodology can be extended to an arbitrary number of layers, we focus on three-layer devices for the remainder of this manuscript for clarity and experimental practicality.

Three-layer device simulations are performed using structures in which each layer has a different lattice constant P_y, while P_x is kept fixed for computational simplicity. Consequently, for each three-layer device simulation, a periodic supercell is constructed in which different unit-cell repetition counts are assigned to each layer. These repetition counts are chosen to introduce only a small deviation from the target lattice constant P_y per each layer (deviation less than 0.6%), thereby enabling the use of periodic boundary conditions in the finite-difference time-domain (FDTD) simulations, as illustrated in Figure 3.3.a (see details in Optical Design with FDTD in Supporting Information). The primary design parameters in this framework are the lattice-scaling parameter α and the post rotation angle θ, as defined earlier. Using this design space, we design and experimentally demonstrate two representative devices to illustrate the full range of achievable spectral tuning. Device 1 (Fig-

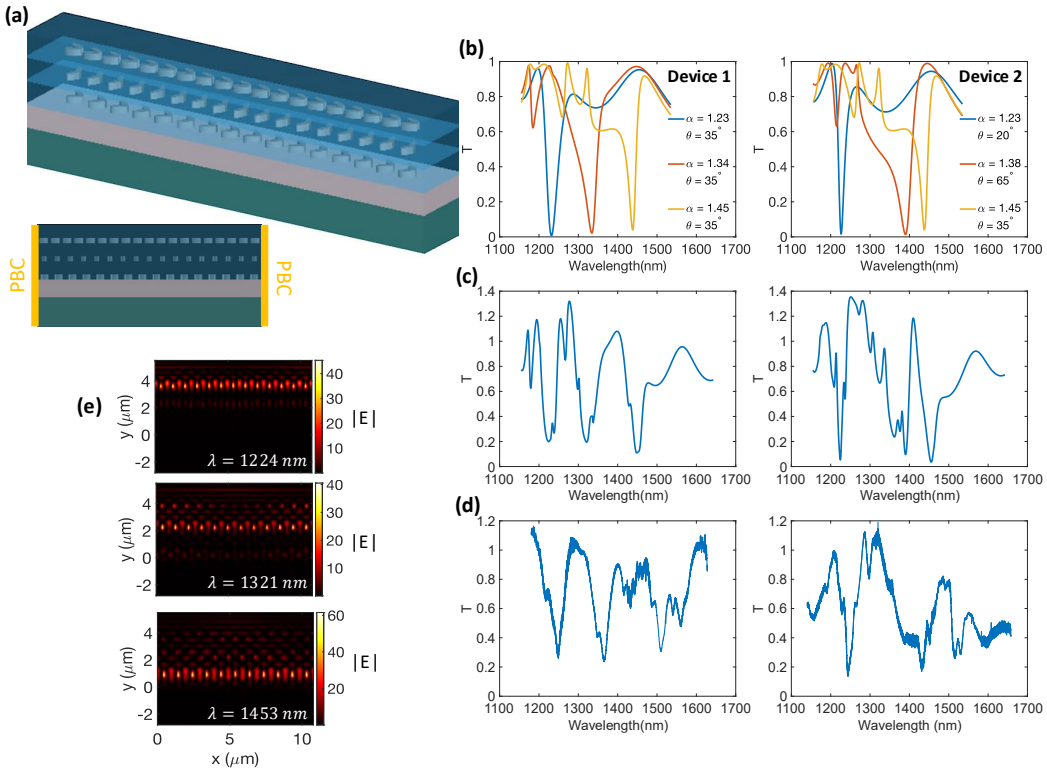


Figure 3.3: **Three-layer rectangular-lattice device: simulation, measurement, and field profiles.** (a) The supercell for the rectangular lattice 3 layer device simulation; the side view shows the different number of iterations per layer and the periodic boundary conditions used on sides in FDTD. (b) Single layer simulations for (α=1.23, θ=35°), (α=1.34, θ=35°), and (α=1.45, θ=35°) on the left; (α=1.23, θ=20°), (α=1.38, θ=65°), and (α=1.45, θ=35°) on the right, while P_x=673 nm is kept constant. (c) Simulated device transmission normalized with respect to the transmission through SiO_2/Si substrate for the 3 layer supercell simulation with the parameters given in (b). (d) Measured device transmission normalized with respect to the measured transmission through the SiO_2/Si substrate, for the devices simulated in (c). (e) The norm of the electric field for the resonances given in (c); the largest wavelength resonators sit at the bottom layer and the smallest wavelength resonators sit at the top layer.

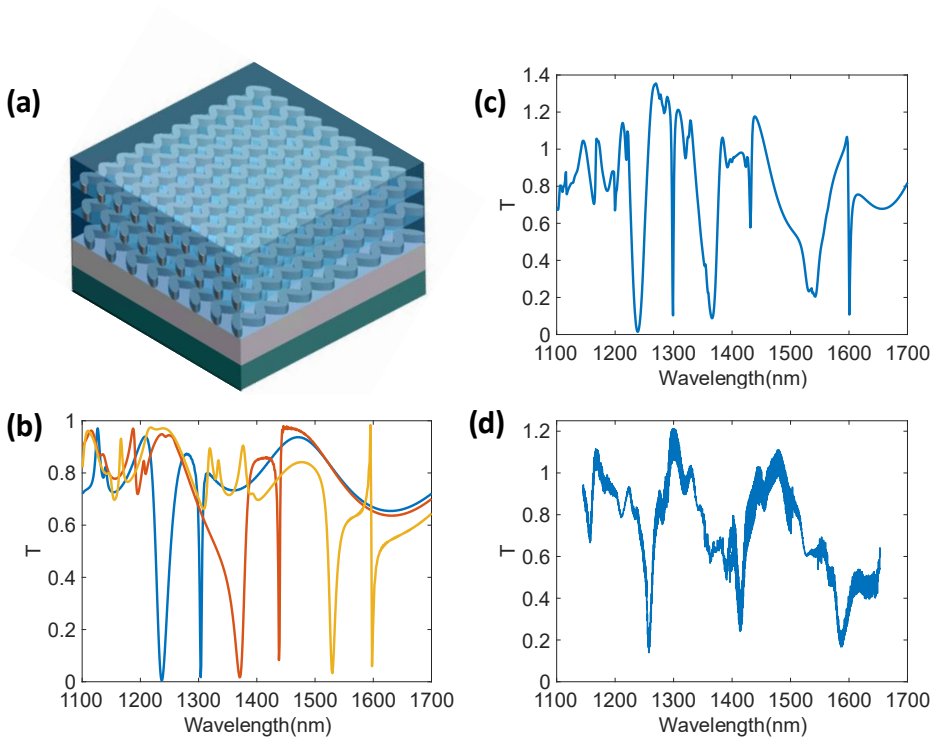


Figure 3.4: **Three-layer square-lattice device targeting six resonances.** (a) The supercell for the square lattice 3 layer device simulation. (b) Single layer simulations for (P_y=P_x=802 nm, θ=35°), (P_y=P_x=893 nm, θ=35°), and (P_y=P_x=1002 nm, θ=35°). (c) Simulated device transmission normalized with respect to the transmission through SiO_2/Si substrate for the 3 layer supercell simulation with the parameters given in (b). (d) Measured device transmission normalized with respect to the measured transmission through the SiO_2/Si substrate, for the device simulated in (c).

ure 3.3.b, left) serves as a reference design, featuring uniform resonance wavelength spacing and similar quality factors across all layers. In device 2 (Figure 3.3.b, right), selective parameter variations are introduced: the rotation angle θ is modified only in the first (top) layer, both θ and α are adjusted in the second (middle) layer, and the third (bottom) layer is kept identical to that of device 1. This layer-wise parameter variation demonstrates that the resonance wavelength and quality factor Q can be tuned independently on a per-layer basis, while leaving the spectral response of the unmodified layers essentially unchanged. As will be shown, this result highlights the decoupled nature of the multilayer design and its suitability for constructing independently programmable spectral filters.

Device 1 consists of three layers in which α takes values of 1.23, 1.34, and 1.45 from

the first (top) to the third (bottom) layer (fabricated device shown in Figure 3.6), while θ is kept at 35° throughout the device. On the other hand, device 2 consists of three layers in which α is set to 1.23, 1.38, and 1.45, and θ is set to 20°, 65°, and 35° from top to bottom. The parameters required for targeting specific wavelengths are calculated by first conducting single-layer simulations (Figure 3.3.b). The three-layer device simulations for device 1 exhibit resonance dips at 1224, 1321, and 1453 nm (Figure 3.3.c, left), while the experimentally measured dips occur at 1247 nm (23 nm shift), 1364 nm (43 nm shift), and 1509 nm (56 nm shift), respectively (Figure 3.3.d, left). For device 2, simulations show resonances at 1224, 1390, and 1455 nm (Figure 3.3.c, right), whereas the experimentally observed dips occur at 1243 nm (19 nm shift), 1431 nm (41 nm shift), and 1512 nm (57 nm shift) (Figure 3.3.d, right). The 23 nm and 19 nm shifts of the first resonances can be attributed to fabrication discrepancies, as these values are reasonably close to the simulated wavelengths. In contrast, the wavelength shifts increase for the lower layers. This behavior can be explained by the bottom spacer layers being exposed multiple times as additional layers are added and patterned. We observe average redshifts of 21 nm and 35.5 nm for layers 1 and 2, respectively, when fabricated geometry discrepancies are taken into account. HSQ is an electron-sensitive material, and its refractive index changes upon electron exposure. As shown in Figure 3.7, a change in the HSQ refractive index of 0.045 results in a 21 nm shift, while a change of 0.067 results in a 35.5 nm shift. These values are reasonable when compared with the limited literature on refractive index changes in HSQ as a function of electron-beam dosage [126]. Finally, we note that 1.4 μm thick HSQ spacers are used between layers, as this thickness was found to be the minimum required for the layers to remain sufficiently decoupled from one another. This is evidenced by the electric-field profiles shown in Figure 3.3.e for the resonances in Figure 3.3.c (left). The 1453 nm resonators reside in the bottom layer, the 1321 nm resonators in the middle layer, and the 1224 nm resonators in the top layer, as indicated in Figure 3.3.e.

As mentioned above, we also designed a six-wavelength device. In this case, the repetition of the unit cells for each layer is performed along both the x and y directions due to the square lattice configuration (Figure 3.4.a). As before, single-layer simulations are first conducted to determine the appropriate design parameters (Figure 3.4.b). The three-layer device simulations exhibit inter-post resonance dips at 1239, 1370, and 1533 nm (Figure 3.4.c), whereas experimentally the resonances appear at 1257 nm (18 nm shift), 1413 nm (43 nm shift), and 1588 nm (55 nm shift) (Figure 3.4.d). As before, the 18 nm shift of the first resonance can be

attributed to geometric deformations during fabrication, while the larger relative shifts of 25 nm and 37 nm are comparable to those observed in the three-wavelength device and can be explained by refractive index changes in the HSQ spacer upon the addition and exposure of subsequent layers. In addition, higher-order hybrid modes appear as shallow dips in the transmission spectrum of the three-layer device. It can be observed that the six-wavelength design layers are both numerically and experimentally more decoupled than the three-wavelength design, as evidenced by the absence of additional resonances with coupling strengths comparable to those of the primary resonances. Compared to the three-wavelength design, the six-wavelength design displays a simpler transmission response with three dominant resonances, while additional coupling-induced features remain weaker. Although the high-Q intra-post modes do not appear experimentally, this behavior results in a cleaner measured spectrum compared to the three-wavelength design. Consequently, depending on the target application, either design strategy may be employed to realize a multi-resonant filter with three operational resonance wavelengths. From a spectral construction perspective, as long as direct and independent control over the filter spectrum is maintained through the available design parameters (α and θ), the presence of additional higher-order modes at distinct wavelengths can further enrich the spectral response and enhance compressive sensing performance.

Filter Array for Compressive Sensing

In addition to having diverse spectral features for compressive sensing, a second parameter needed for such reconstruction is to have a set of basis functions with minimum correlation. In spectral reconstruction, the goal is to estimate the incident optical spectrum from measurements obtained using a limited number of arrayed filters. Designing metasurface filters with decorrelated or minimally overlapping spectra reduces the mutual correlation of the measurement matrix, thereby stabilizing the inversion problem and improving noise robustness [127, 128, 129, 130]. Moreover, low-correlation basis spectra increase the system's ability to resolve narrow spectral features and reduce the number of measurements required for compressed sensing-based recovery. Owing to their capability for precise tailoring of transmission and reflection spectra, metasurfaces have emerged as particularly promising platforms for constructing such spectral basis sets [131, 132, 133, 134].

By enabling fine control over resonance wavelengths and Q-factors across multiple layers, our multi-resonant metasurfaces naturally generate a set of decorrelated spectral transfer functions that serve as an advantageous basis for stable and high-fidelity

spectral reconstruction. Each multilayer filter exhibits a rich spectral response, combining both broadband and narrowband features arising from resonances localized in individual layers, as well as from higher-order hybrid modes. A key advantage of this platform is the direct and independent control over the shape of each basis spectrum through deterministic tuning of the resonance wavelengths and their associated Q factors. Previous approaches have demonstrated the use of single-layer photonic crystal slabs [128] and free-form inverse-designed metasurfaces [135, 136, 131] for spectral reconstruction. Multilayer filter architectures have also been proposed to further reduce mutual correlations between basis spectra; however, these implementations typically rely on stacks of thin films or combinations of metasurface pillars and thin-film layers to achieve spectral diversity [104, 137, 129, 130]. Such architectures are generally not well suited for single-chip operation, as different filter regions require different overall thicknesses. In contrast, the approach presented here maintains identical spacer thicknesses across all filters and achieves spectral tuning exclusively through geometric modification of the elliptical resonators. This uniform-thickness design is inherently compatible with single-chip integration.

In literature, the correlation coefficient of such basis functions has been used as the main metric to characterize and justify such spectra [128, 131, 135, 136]. Here we use Pearson correlation coefficient to calculate the extent to which the spectrum set is linearly independent using the expression:

$$r_{xy} = \frac{\sum_{i=1}^{n}(x_i - \bar{x})(y_i - \bar{y})}{\sqrt{\sum_{i=1}^{n}(x_i - \bar{x})^2}\sqrt{\sum_{i=1}^{n}(y_i - \bar{y})^2}} \tag{3.1}$$

where $x_i(y_i)$ is the transmission value at wavelength λ_i for arbitrary two filters, and $\bar{x}(\bar{y})$ is the mean of $x_i(y_i)$ values for i=1,2,..,601 (from 1100nm to 1700nm). Changing the parameters α from 1.147 to 1.587 (17 points) and θ from 5° to 80° (6 points), we chose the set of filters shown in Figure 3.5. Again, to be able to operate on a single chip, spacer thicknesses are kept the same (1.4 um) throughout the filter array.

In order to do an extensive literature comparison, we generate a set of 9 and a set of 36 filters with average absolute values of the pairwise correlation coefficients r_{xy} 0.11 (Figure 3.5.a) and 0.21 (Figure 3.5.b) respectively in the 1100-1700 nm band. To efficiently design a diverse set of multi-resonant filters, we first approximate three-resonance transmission spectra using 102 single-layer simulations (17 values of α and 6 values of θ). For every combination of three single-layer resonances, an

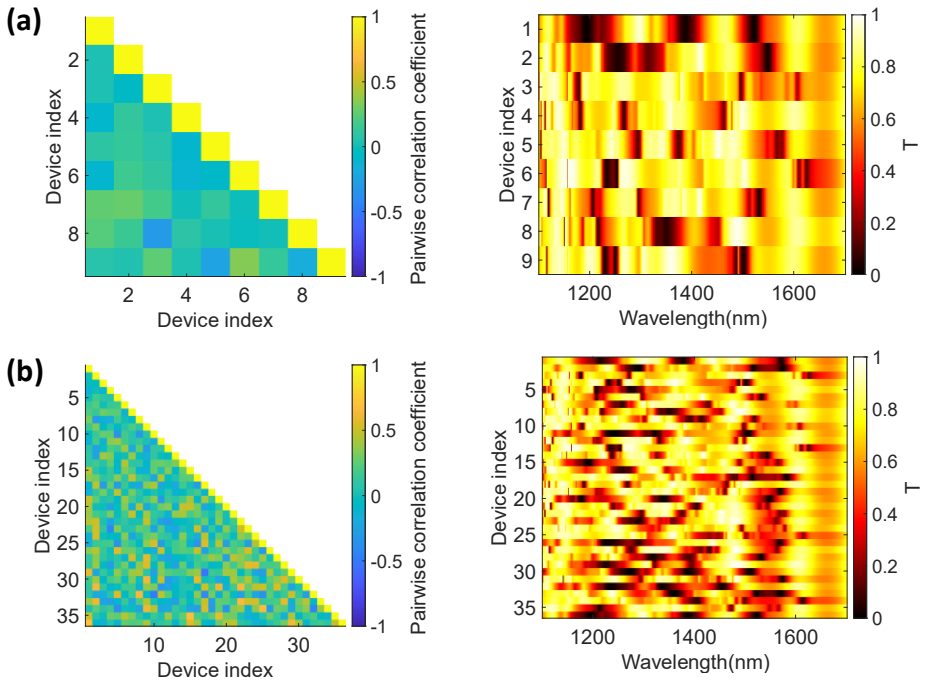


Figure 3.5: **Decorrelated filter arrays for compressive spectral sensing.** (a) Pairwise correlation coefficients for the selected 9 devices with average absolute value of the pairwise correlation coefficients 0.11 (left) and the heatmap for the transmission spectra of these filters (right). (b) Pairwise correlation coefficients for the selected 36 devices with average absolute value of the pairwise correlation coefficients 0.21 (left) and the heatmap for the transmission spectra of these filters (right).

estimated multilayer response was constructed by taking the point-wise minimum of the corresponding single-layer transmission curves, which provides a fast surrogate for the composite three-layer device spectrum. The Pearson correlation coefficients between all estimated spectra were then computed, and a greedy max–min diversity selection algorithm [138] was applied to extract subsets of 9 and 36 candidate parameter sets that minimize pairwise spectral similarity. In this algorithm, the first spectrum is chosen based on its overall variance, and subsequent spectra are added iteratively by selecting, at each step, the candidate whose maximum absolute correlation with all previously selected spectra is the smallest. This ensures that each newly added spectrum contributes maximal additional diversity to the selected set. The resulting set of 9 and 36 filters were subsequently validated through full 3D simulations of the actual three-layer devices, confirming that the greedy selection

procedure reliably identifies parameter sets that yield low-correlated, spectrally distinct filter responses. When we compare the average correlation values with the literature examples mentioned above, we see that Wang et *al.* design a 3x3 array with average correlation coefficient 0.17 with photonic crystal slabs for 8-11.5 um wavelength band [128]; Hu et *al.* design a 5x5 array with average correlation coefficient 0.22 with freeform metasurfaces for 380nm-680nm wavelength band [131]; Chen et *al.* design a 7x7 array with average correlation coefficient 0.41 with freeform metasurfaces for 400nm-700nm wavelength band [135]; and, Chen et *al.* design a 6x6 array with average correlation coefficient 0.49 with freeform metasurfaces for 500nm-700nm wavelength band [136]. Our filters (both set of 9 and 36) surpass these studies in terms of decorrelation within a comparable operation band.

3.3 Conclusion

In conclusion, we have demonstrated a high-throughput direct-write fabrication platform based on an antimony–BDCA precursor for multilayer resonant metasurfaces. This work greatly expands the design space of multilayer devices that has remained comparatively unexplored due to the complexity and low yield of standard nanofabrication flows. By combining Sb_2S_3 q-BIC–derived metasurfaces with HSQ planarization layers, we realize three-layer architectures in which each layer remains largely decoupled, enabling independent control of multiple resonances through the geometric parameters α and θ while keeping all spacer thicknesses identical across the chip. This yields compact multi-resonant filters whose transmission spectra can be arbitrarily tailored at design time, providing rich combinations of broad and narrow features that are directly encoded by device geometry rather than by varying film thickness. We leveraged this capability to generate decorrelated filter arrays that are well suited for spectral reconstruction based on compressive sensing, demonstrating sets of 9 and 36 filters with average absolute pairwise Pearson correlation coefficients of $|r_{xy}| = 0.11$ and 0.21, respectively, surpassing previously reported metasurface and photonic-crystal–based implementations in both decorrelation and operational bandwidth. Beyond the specific 3 and 6 wavelength devices realized here, this platform paves the way towards structures with more patterned layers to enable densely-spaced resonances and integration with on-chip detector arrays. Ultimately, we envision application-specific metasurface filters where arbitrary low-correlated spectral basis arrays can be co-designed and monolithically fabricated for compact, high-performance hyperspectral imaging and compressive spectroscopy

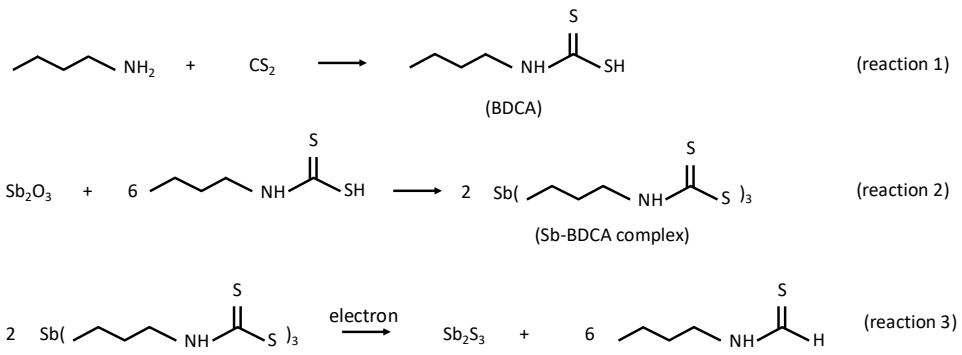
systems.

3.4 Appendix

Fabrication Details

Precursor Solution Synthesis

The precursor was synthesized by reacting 1-butylamine (2 mL) with carbon disulfide (1.5 mL) to get BDCA (reaction 1). The precursor, which is a Sb-BDCA complex is created mixing antimony (III) oxide (1 mmol) dissolved in ethanol (2 mL), and BDCA (reaction 2). When this complex is exposed to an electron bombardment, it decomposes into Sb_2S_3 in addition to other organic byproducts (reaction 3). Unexposed area and the byproducts of the exposed area remain organic and washed away by immersing in isopropanol (IPA) for 10 mins.



The synthesis procedure follows: In a round-bottom flask, antimony (III) oxide is dissolved in ethanol and carbon disulfide at room temperature as reported in Ref. [96]. The flask was connected to a Schlenk line (nitrogen flow, no vacuum applied) through a glass condenser, and the mixture was stirred under nitrogen. Subsequently, 1-butylamine was added to the flask drop-by-drop since the reaction is exothermic, after which the reaction was allowed to proceed under continuous stirring overnight.

Preparation of the Substrate

1300 nm of silica was deposited using PECVD on a double sided polished (DSP) doped silicon wafer. We fabricated gold markers on silica deposited silicon chips by patterning an electron beam resist ZEP520A using EBL, depositing 50 nm gold with electron beam deposition, and lifting off the excess gold. We used these markers

sitting on the substrate for all of the layers patterned and no additional markers were fabricated per added layer.

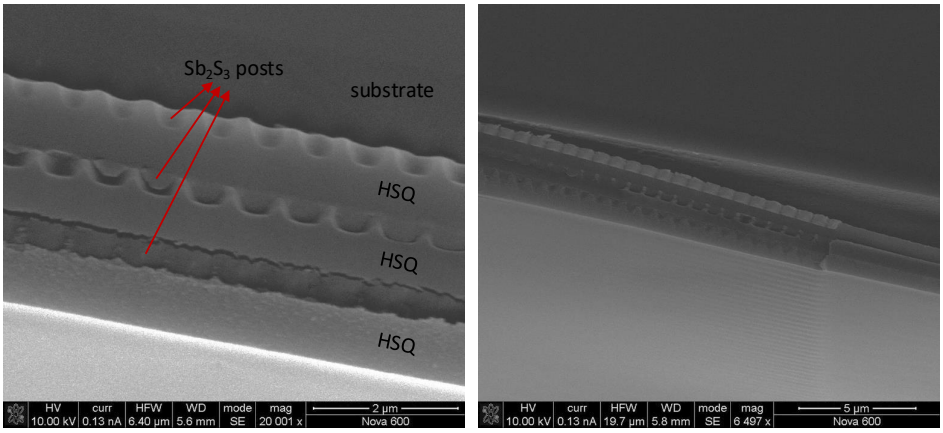


Figure 3.6: **Cross-sectional SEM of the fabricated three-layer Sb_2S_3 device.** SEM image of the cleaved 3 layer device given in main manuscript Figure 3.3.c and d on the left; zoomed out cross section SEM where the posts are still intact on the right (edge lifted during cleaving).

EBL Patterning

For film deposition, 1 mL of the precursor solution was diluted with 2 mL of ethanol and spin-coated at 6500 rpm to form a uniform thin film. This spin-coating step is repeated once more before exposure to have a thicker spin-coated film. The coated substrates were then patterned using a 100 kV EBL system with a beam current of 20 nA. A multipass exposure strategy was employed, consisting of 10 passes with a dose of 50 mC/cm^2 per pass (total accumulated dose of 500 mC/cm^2). A multipass approach is preferred to avoid dumping all the exposure energy at a single location and then switch to the next writing grid. Instead energy exposure is done bit by bit over all patterned region. This makes the resulting patterns much closer to the intended write patterns. For continuous pattern that are larger than the subfield of the EBL tool (4 um), this becomes a neccessity to avoid cracks.

Following the exposure, the samples were developed in IPA, and subsequently annealed at 180 °C for 2 min on a hotplate inside a nitrogen glovebox. For planarization, HSQ (FOx-16) was spun at 5000 rpm for 60s twice to reach to a thickness of approximately 1.4 um on the Sb2S3 structures. Here, HSQ was used only as a spin-on-glass for planarization (not as an electron beam sensitive medium). The spun HSQ was annealed at 180 °C for 2 mins for partial curing. These steps are

repeated to fabricate each layer. The 3 layer device mentioned in the manuscript can be seen in Figure 3.6, left. Here, since P_y in each layer is different, the cross section of the ziczac pattern appears as post cross sections with different sizes. We note that the posts in the first and second layer fell due to cleaving, however, we also maned to image regions of the device where the posts were still intact (Figure 3.6, right).

Chemical and Optical Characterization

Although there are several reports on the refractive index of Sb_2S_3 (n), the value of n depends strongly on the synthesis conditions of the precursor as well as subsequent processing parameters such as precursor dilution during spin coating and the phase of the resulting material [119, 120, 121].

Direct determination of the refractive index using ellipsometry is impractical in this

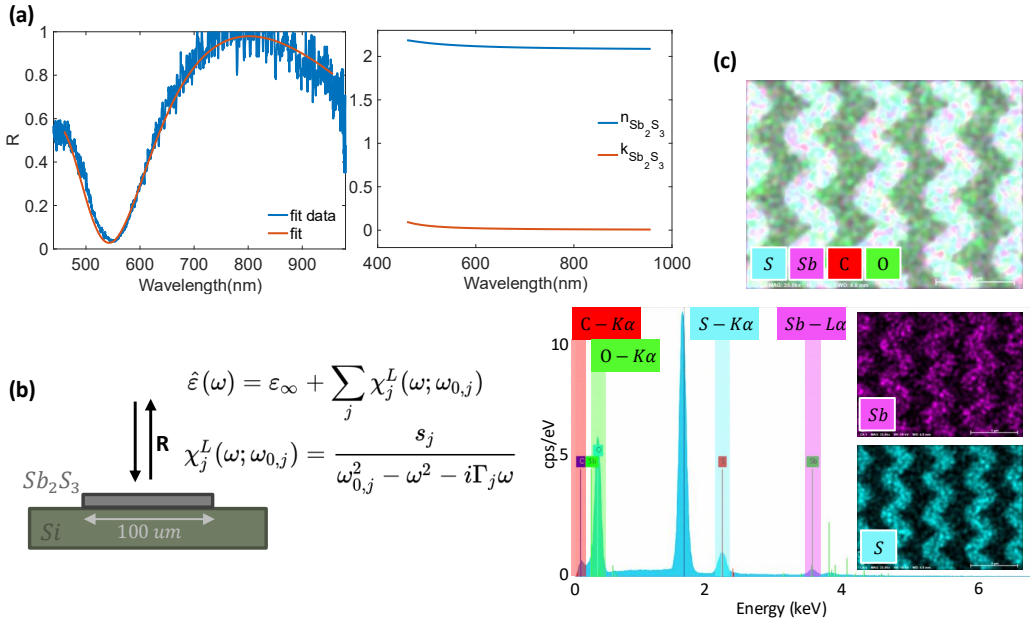


Figure 3.7: **Optical and chemical characterization of Sb_2S_3 thin films.** (a) Measured reflection from the sample and the fit with the oscillator model (left) and the consequent n, k data (right). (b) 100 µm × 100 µm large Sb_2S_3 pattern on Si substrate for the reflection measurements and the Lorentz oscillator model used, where ε_∞ is a parameter that captures the effects of higher energy contributions to the dielectric function, and s, ω_0, ω, Γ are the oscillator strength, resonant frequency, optical frequency, and oscillator linewidth, respectively. (c) EDS measurement showing the chemical composition of the nanostructures patterned on the substrate, where cyan denotes sulfur (S), magenta denotes antimony (Sb), red denotes carbon (C), and green denotes oxygen (O).

case, as it would require patterning a continuous, centimeter-scale Sb_2S_3 film, which is prohibitively time-consuming due to the high electron beam doses involved. Instead, the dielectric function of Sb_2S_3 is extracted by fitting reflection measurements performed on a thin Sb_2S_3 film using the transfer matrix method (TMM) (Figure 3.7.a).

To this end, we fabricated continuous 100 μm × 100 μm square Sb_2S_3 patterns on a silicon substrate and performed reflection measurements using a supercontinuum source coupled to a spectrometer over the wavelength range of 450–950 nm. The incident beam was focused to a spot size of approximately $\sim$ 70 μm on the Sb_2S_3 film. The measured reflectance spectrum was fit using a thin-film interference model based on TMM [139], enabling extraction of both the real (n) and imaginary (k) components of the refractive index. Specifically, the dispersive response of the film is parameterized using a Lorentz oscillator model, with the functional form shown in Figure 3.7.b. Model fitting is performed using a particle swarm optimization (PSO) algorithm. The fitting wavelength range is chosen to be 450–950 nm, rather than the device operation band, as the reflectance data in this region exhibits stronger spectral features that enable more reliable extraction of the dielectric function. Given the monotonic behavior of the extracted refractive index, a constant value of $n = 2.1$ is assumed over the device operation band, which will be shown to agree with the experimental results.

The chemical composition of the patterned Sb_2S_3 structures is further confirmed using energy-dispersive X-ray spectroscopy (EDS). As shown in Figure 3.7.c, the EDS spectra clearly indicate the presence of antimony and sulfur, confirming the chemical decomposition of the precursor into Sb_2S_3. Additional signals corresponding to silicon, oxygen, and carbon arise from the substrate, the underlying spacer layer, and the conductive coating used for scanning electron microscopy (SEM), respectively.

Optical Design with FDTD

For single layer simulations two rotated Sb_2S_3 elliptical posts (n=2.1) that are 400 nm thick (rotated by θ) are placed on a 1.3 um thick SiO_2 bottom spacer on a Si substrate. Here, the lattice constants are set as $P_x = s * 1020$ nm and $P_y = \alpha * P_x$. The length of the semi-major axes of the elliptical posts are set as $s * 165$ nm and $s * 500$ nm respectively where s is the scaling factor for all lateral features. This constant scaling factor s is applied to all lateral features including the ellipses and the lattice to make Q of the resonance only depend on the tilt angle θ. In Figure 3.b,

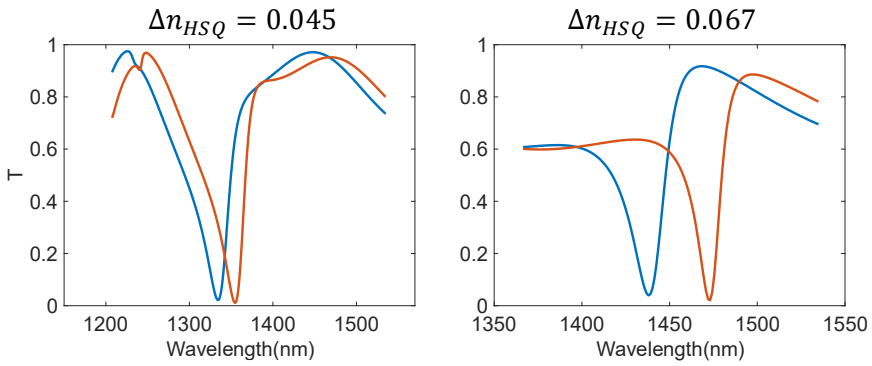


Figure 3.8: **Resonance wavelength shift due to HSQ refractive index change upon electron exposure.** The shift of the resonance with the change in the HSQ refractive index Δn_{HSQ}=0.045 and Δn_{HSQ}=0.067.

for the square lattice simulation, s=0.870 and α=1, and for the rectangular lattice simulation shown in Figure 3.c, s=0.660 and α=1.34. The planarization layer is set to HSQ with n=1.4. The top and the bottom boundary conditions are set as perfectly matched layer (PML) where the side surfaces are set to Bloch periodic boundary conditions. As for the 3 layer simulations, for each layer i with nominal lattice constant $P_{y,i}$, we choose an integer repetition number N_i and define a common supercell length L_y such that $L_y = N_i P'_{y,i}$, where $P'_{y,i}$ is a slightly adjusted lattice constant. Because the nominal periods $P_{y,i}$ generally do not form an exact integer ratio, we select $\{N_i\}$ so that the adjusted values $P'_{y,i} = L_y/N_i$ deviate minimally from the design values (less than 0.6%).

HSQ Refractive Index Change

The shift between the simulated resonance wavelength and what is measured can be explained by the index change of HSQ with the exposure per added layer as shown in Figure 3.8.

Coupling Between Layers

While the 1.4 μm HSQ spacer thickness is chosen to minimize interlayer coupling, perfect decoupling between layers is not achievable in practice for any finite spacer thickness. As evidenced by the electric field profiles in Figure 3.e, the resonant modes are predominantly localized within their respective layers; however, the evanescent tails of each mode extend into adjacent layers, giving rise to weakly coupled hybrid higher-order modes that manifest as additional spectral features in

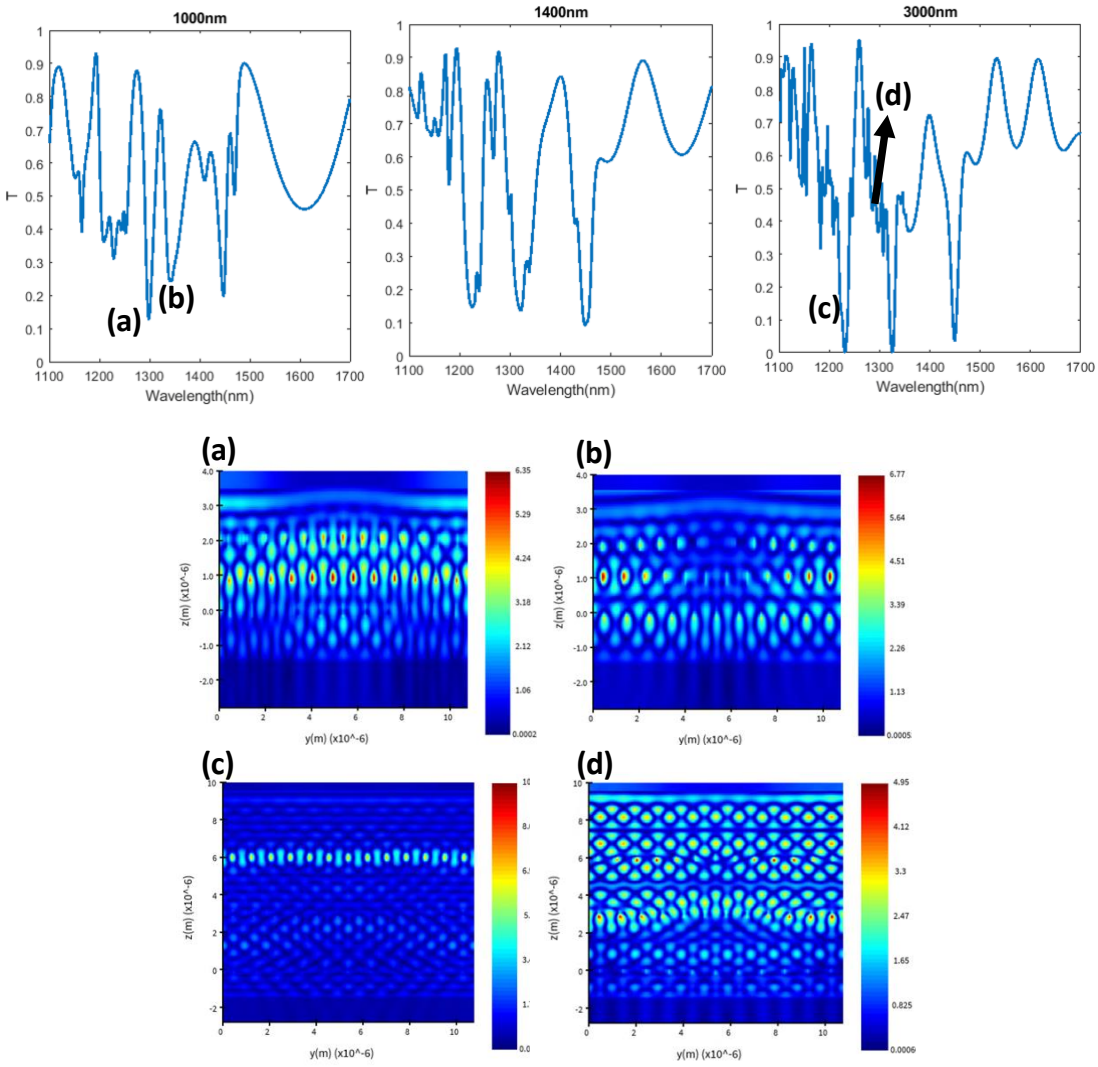


Figure 3.9: **Effect of HSQ spacer thickness on interlayer coupling and transmission spectra.** The transmission spectrum of the filter shown in Figure 3.c in the main manuscript for HSQ spacer thicknesses of 1000, 1400, and 3000 and 3000 nm. (a), (b), (c) and (d) are the electric field profiles corresponding to the resonance dips pointed in these spectra for HSQ thickness of 1000 and 3000 nm.

the transmission spectra. The spacer thickness of 1.4 μm represents a practical optimum: sufficiently thick to suppress strong interlayer coupling and limit the number of prominent hybrid modes, yet thin enough to avoid the dense higher order modes that emerges at larger spacer thicknesses where the cavity resonances of the dielectric stack begin to dominate the transmission response. Figure 3.9 shows the simulated three-layer transmission spectrum for a range of HSQ spacer thickness varying between 1000nm and 3000nm. This figure demonstrates that when the spacer is not thick enough, different layers that were designed to host

independent resonances are coupled with each other. The resonances appear at the target resonance wavelengths (Figure 3.9.a) and the extra features appeared (Figure 3.9.b) have similar electric field profiles. On the other hand, when the spacer is too thick, the layers are mostly decoupled from each other as the optical field mostly resides within its layer (Figure 3.9.c). However, Fabry-Perot variations become more significant and many higher order hybrid modes appear (Figure 3.9.d), which shows itself as shallow, high frequency variations in the transmission spectrum. Therefore, a 1400 nm sweet spot is chosen for the spacer thickness as the layers are fairly decoupled from each other as shown in Figure 3.9.e in the main manuscript, yet the filter response is a clean multi-resonant spectrum with minimal small hybrid mode variations.

Experimental Absence of High-Q Intra-Post Resonances

The absence of high-Q intra-post resonances in the measured spectra can be attributed to several compounding loss mechanisms. We performed additional simulations incorporating a finite imaginary part of the refractive index (k>0) for Sb2S3, which show that the intra-post resonance is indeed quite sensitive to absorption loss, and mostly suppressed at k=0.05 (Figure 3.10). Although zero k is expected at operation bandwidth, the Lorentz model fit to our reflection measurement might

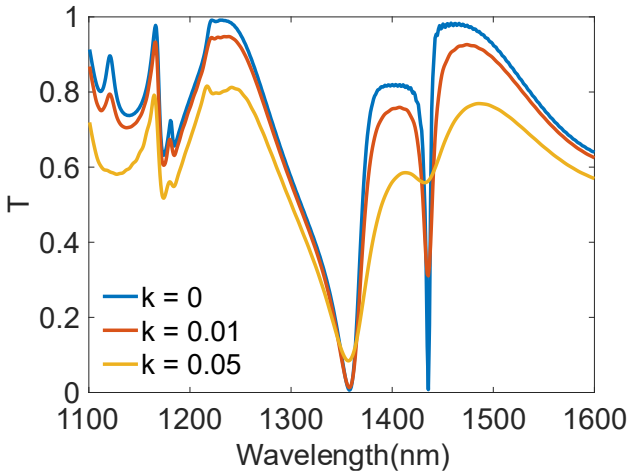


Figure 3.10: **Suppression of high-Q intra-post resonances under material absorption loss.** The transmission spectrum of the square lattice filter given in the main manuscript in Figure 2.b for k = 0, 0.01 and 0.05.

not be perfectly accurate and the refractive index fit can slightly vary based on the fit parameters. On the other hand, the lower-Q inter-post resonance remains largely unaffected, which supports the hypotheses that the high Q resonances disappear experimentally due to a loss mechanism.

Second, geometric imperfections introduced during fabrication including edge roughness and ellipticity deviations from the target dimensions could act as scattering centers that couple energy out of the confined intra-post mode. Because the intra-post resonance is predominantly confined within the resonators themselves and couples weakly to external radiation channels by design, it is inherently more sensitive to such perturbations than the inter-post mode.

Taken together, these effects collectively explain why the high-Q intra-post resonances ($Q \approx 450$–500 in simulation) are not observed experimentally (or observed similar to one of the shallow hybrid-mode in the spectrum, which is hard to differentiate), while the inter-post resonances with their lower Q values remain robustly detectable.

Chapter 4

SUB-DECIBEL EFFICIENCY AUGMENTED MULTILAYER VERTICAL GRATING COUPLER VIA ADJOINT INVERSE DESIGN AND SB_2S_3 DIRECT-WRITE E-BEAM LITHOGRAPHY

The material in this chapter is part of an ongoing work, and will be presented in Ref. [140].

We present a design study of an augmented two-layer Sb_2S_3 grating coupler that enables efficient vertical coupling of free-space light into the fundamental transverse-electric (TE) mode of a silicon-on-insulator waveguide without any modification to the host photonic integrated circuit, attaching only through a feature-free taper. Using adjoint-based inverse design with the Adam optimizer in Tidy3D FDTD, we co-optimize 204 geometric and source-position parameters under a bandwidth-averaged figure of merit. The optimized structure achieves a simulated peak coupling efficiency of 89.5% (−0.48 dB) at 1550 nm, and retains ≥ 50% efficiency under cumulative fabrication deviations.

4.1 Introduction

Efficient coupling between free-space or fiber-guided light and on-chip photonic waveguides is a fundamental requirement in integrated photonic systems spanning optical communications [141, 142], LiDAR [143, 144], quantum information processing [145, 146], and biosensing [147, 148]. Grating couplers remain the most widely deployed interface for this purpose owing to their compatibility with standard wafer-level testing and their relaxed fiber-alignment tolerances compared with edge couplers. Nevertheless, single-layer grating couplers are fundamentally limited in coupling efficiency (CE) because diffraction from a periodic grating is inherently bidirectional: a significant fraction of the incident power is scattered downward into the substrate rather than into the guided mode [149]. Apodized designs [150, 151], blazed profiles [152, 153], and integrated back-reflectors [154, 155, 156] can partially recover these losses but typically require specialized process steps that are incompatible with commodity foundry platforms [157].

A complementary strategy is to *augment* an existing grating coupler by depositing additional patterned layers directly on top of the host photonic circuit [158, 159,

160, 161]. This augmentation paradigm offers a decisive practical advantage: the underlying PIC requires no modification whatsoever beyond the inclusion of a conventional taper that transitions from the waveguide to the grating region without additional grating features. As a result, the same set of augmentation layers can, in principle, be applied to different photonic platforms or swapped out to achieve distinct coupling objectives, including oblique coupling, broadband response, or polarization insensitivity, without altering the foundry-defined waveguide layer. This flexibility is particularly valuable in heterogeneous integration scenarios where the target PIC is fabricated under a locked process design kit (PDK) such as those offered by commercial silicon-photonics foundries, where modifying the device layer or adding a back-side mirror is either prohibited or prohibitively expensive. Despite this potential, performatively competitive non-invasively augmentable vertical couplers remain rare, as multilayer photonic devices are often avoided in practice due to their fabrication complexity. A multilayer architecture is nevertheless essential if augmentation is to deliver coupling efficiencies on par with conventional chip-level couplers.

To navigate the high-dimensional parameter space of such a multilayer structure, we employ gradient-based inverse design via the adjoint method [162, 163, 164] in a parametric shape-optimization scheme. The adjoint method computes the exact gradient of a scalar objective with respect to all design parameters from only two electromagnetic simulations per iteration (one forward and one adjoint) regardless of the number of free parameters. Automatic differentiation through the post-processing pipeline is handled by the AUTOGRAD package [165], which propagates gradients from the coupling-efficiency figure of merit back through the mode-overlap calculation. Combined with the Adam optimizer [166], which adapts per-parameter learning rates using first- and second-moment estimates of the gradient, the framework efficiently explores non-convex loss landscapes and avoids premature convergence to shallow local minima. Adjoint optimization has been applied to grating-coupler design previously [167, 168, 169, 170], but, to our knowledge, not in combination with a non-invasive augmentation layer stack of the type considered here.

The contributions of this work are threefold. First, we propose a non-invasive two-layer Sb_2S_3 augmentation architecture in which the host PIC requires only a feature-free taper, enabling deployment on locked foundry process flows. Second, we develop and apply an adjoint-based shape-optimization framework that

simultaneously co-optimizes 204 geometric and source-position parameters under a bandwidth-averaged figure of merit, yielding a simulated peak CE of −0.48 dB at 1550 nm. Third, we quantify the design's robustness to cumulative fabrication variations and identify the dominant sensitivity channels, providing a concrete path to experimental validation.

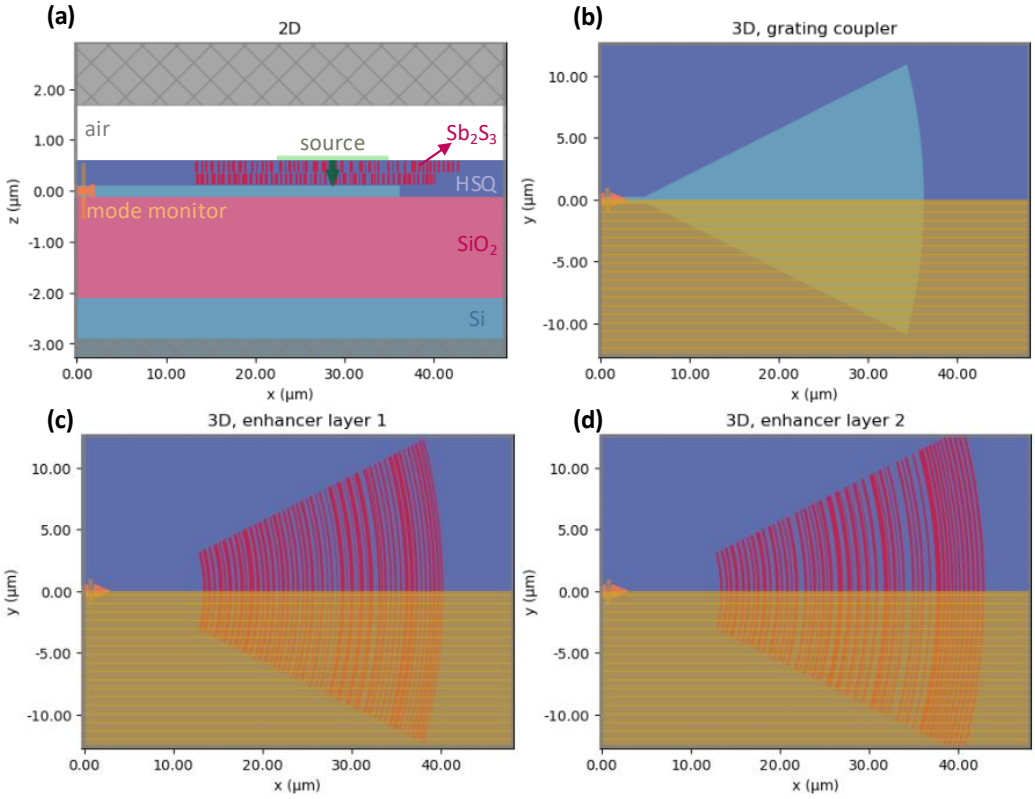


Figure 4.1: **Layer stack and simulation setup of the augmented two-layer grating coupler.** (a) Side view of the SOI waveguide and the two-layer Sb_2S_3 augmentation grating coupler. The green line with a downward arrow represents the vertically incident Gaussian source, and the orange mark indicates the mode monitor used to evaluate coupling efficiency into the fundamental TE waveguide mode. The top and bottom gray regions denote the perfectly matched layers (PML). (b) Three-dimensional schematic of the full device, including the input single-mode waveguide, the feature-free taper, and the two stacked Sb_2S_3 grating apertures embedded in the HSQ planarization layer. (c,d) Top-view profiles of the first and second optimized Sb_2S_3 grating layers, respectively.

4.2 Device Design

The simulated device is built on a silicon-on-insulator (SOI) substrate. The silicon device layer is 220 nm thick, a common thickness across commercial silicon-photonics foundries, and sits on a 2 μm buried oxide (BOX) layer that serves as the lower cladding (Figure 4.1.a). The host photonic circuit consists of a single-mode silicon waveguide that fans out through a 28 μm taper into a grating-coupler aperture, followed by a 5 μm unpatterned waveguide section on which the mode-overlap monitor is placed (Figure 4.1.b). Crucially, the host circuit contains no grating features: all the nano structures used for phase matching between the free-space light and the TE mode of the silicon photonic waveguide resides in the augmentation layers above. This separation allows the same SOI layout to host any augmentation stack tailored to a different coupling objective.

Above the device layer, a hydrogen silsesquioxane (HSQ) planarization film is used which increases the total silicon photonic layer thickness to 235 nm. HSQ is selected because it converts to a near-SiO_2 matrix after exposure and thermal cure, yielding an optically homogeneous spacer between the silicon waveguide and the augmentation grating [78]. On top of the planarized surface, two 230 nm thick Sb_2S_3 layers are patterned independently, where Figure 4.1.c and d shows the top view of the two Sb_2S_3 patterned layers. The two patterned Sb_2S_3 grating layers occupy the same footprint as the underlying taper aperture but are laterally offset with respect to the host waveguide by independently optimized amounts; these offsets set the inter-layer phase relationship that drives constructive interference into the guided mode. These two Sb_2S_3 grating layers also have a total 235 nm thickness each, separated by only a 5 nm HSQ spacer layer between to maximize the interaction of the layers to increase the degrees of freedom to optimize for in the device design space. Here, 230 nm thickness for the patterned Sb_2S_3 layer is determined by the optimized spin coating and Sb_2S_3 based direct e-beam lithography write conditions that result with the ideal film uniformity and the non-uniform grating pattern resolution. Although the optimization starts from a 70 nm thick HSQ spacer layer in between Sb_2S_3 layers, the optimization converges to the minimum limit set for the HSQ layer, which is 5 nm. The reason why a planarization layer to only fill in the voids with no extra thickness in between layers is not used is two fold. First, for a later experimental demonstration, that would increase the risk for over-etching the HSQ layer, hence the Sb_2S_3 layer which would create non-volatile byproducts in a typical fluorine based SiO_2 pseudo-Bosch etch. Second, a device that is designed for no extra propagation in between the grating layers could be more sensitive to experimental

HSQ thickness deviations. Although small (5 nm), if this is already taken into account in an optimization like the current design parameters, the performance will be more tolerant for the fabricated HSQ thickness deviations.

Sb_2S_3 is selected as the augmentation material for three reasons. First, its refractive index ($n \approx 2.2$ at 1550 nm) lies between that of the SOI silicon device layer ($n \approx 3.48$) and the HSQ cladding ($n \approx 1.44$), which improves impedance matching for free-space coupling and reduces back-reflection compared with grating features etched directly into the silicon layer. Second, it is transparent across the visible and near-infrared, enabling the same augmentation strategy to be ported to shorter operating wavelengths without changing the material. Third, Sb_2S_3 is patternable through a precursor based high throughput direct electron-beam write fabrication platform [78], which allows the two grating layers to be fabricated by a single-step lithography on each layer rather than going through the full cycle of PECVD, patterning a electron beam resist, depositing hard mask, lift-off, plasma etching required for conventional dielectrics [171, 172]. This is the intended fabrication pathway for future experimental validation; the present work concerns only the electromagnetic design.

4.3 Methods

Simulation Setup

All electromagnetic simulations are performed in Tidy3D [173], a GPU-accelerated implementation of the finite-difference time-domain (FDTD) method. As can be seen in Figure 4.1.a, the simulation domain spans roughly 70 μm along the propagation direction (x) and 5.2 μm in the out-of-plane direction (z). The domain fully encloses the SOI waveguide and taper, the partially etched silicon grating, the two Sb_2S_3 augmentation gratings, the intervening HSQ spacer stack, the 2 μm buried oxide, and a silicon substrate.

The spatial grid is non-uniform, generated by Tidy3D's automatic mesh-refinement engine at a target of 30 cells per free-space wavelength referenced to $\lambda_0 = 1.55\,\mu$m. This yields a minimum cell size of approximately 15 nm inside silicon and 24 nm inside the Sb_2S_3 regions, with coarser cells in the oxide and air. The domain is terminated by the default 12-layer perfectly matched layers (PMLs) along $\pm x$ and $\pm z$ to absorb radiation into the substrate, into free space above the cladding, and out through the truncated waveguide; periodic boundaries are used in y as appropriate for the 2D cross section.

The excitation is a vertically incident Gaussian beam with a $1/e^2$ diameter of 10 μm. The 10 μm beam waist is chosen to match both (i) the spot size produced by a typical focusing objective used in free-space characterization setups and (ii) the mode-field diameter of a standard single-mode fiber at 1550 nm, which is approximately in the range of 8–10 μm [174]. The Gaussian source is placed 50 nm above the top HSQ spacer at normal incidence ($\theta = 0°$), with TE polarization and a Gaussian temporal pulse centered at $\lambda_0 = 1.55\,\mu$m and a bandwidth covering the C-band window $\lambda \in [1.52, 1.58]\,\mu$m. Coupling efficiency is evaluated at a mode monitor placed in the silicon waveguide 5 μm downstream of the taper exit, computed as the fraction of the vertically incident optical power that is projected onto the fundamental TE mode of the 220 nm-thick silicon strip waveguide, sampling the same wavelength range at 61 wavelengths. The silicon, HSQ, and Sb_2S_3 refractive indices used are $n_{Si} = 3.476$, $n_{HSQ} = 1.44$, and $n_{Sb_2S_3} = 2.20$ at 1550 nm [175, 176].

Inverse-design Framework

Inverse-design methods for photonic devices fall into two paradigms: topology optimization and parametric shape optimization. In topology optimization, the refractive index at every pixel within a prescribed design region is treated as a free variable, enabling discovery of freeform geometries inaccessible to intuition-guided design [168, 177]. This approach has been applied to grating couplers [168, 167] and to a wide range of other integrated photonic components [177], often achieving compact footprints with competitive performance. However, the resulting geometries frequently contain disconnected islands, sub-wavelength voids, and feature sizes that violate the minimum-linewidth rules imposed by lithographic processes [178]. While density filtering, projection methods, and binarization schedules mitigate these issues, none guarantee design-rule compliance throughout the optimization trajectory. A further difficulty for lithographic processes is that proximity-effect correction depends on local pattern density; spatially varying lithographic biases are difficult to predict for the irregular freeform features produced by topology optimization, complicating the path from simulation to fabrication.

Parametric shape optimization takes a complementary approach: the design space is explicitly constrained to structures described by a physically motivated set of geometric parameters. In the present case, these parameters are the tooth and gap widths of each grating period, the lateral offsets of each Sb_2S_3 layer, the spacer thickness, and the in-plane source position. Because every parameter maps directly to a fabricable geometric quantity, the resulting structures are inherently manu-

facturable without topology sanitization. Gradients of the objective with respect to all parameters are computed via the adjoint method [164, 177], preserving the scalability advantage of topology optimization while operating within a physically interpretable and lithography-compatible design space. This paradigm has been applied successfully to grating-coupler design with tooth-and-gap parametrizations [167, 150, 151].

Optimization and Parameters

The design objective is to maximize coupling efficiency at 1550 nm. Rather than optimizing CE at a single wavelength, which can yield sharp, fabrication-sensitive spectral peaks, we define the figure of merit $\mathcal{F}$ as the spectrally averaged CE over a 10 nm band centered at the design wavelength:

$$\mathcal{F} = \frac{1}{\Delta\lambda} \int_{\lambda_0 - \Delta\lambda/2}^{\lambda_0 + \Delta\lambda/2} \mathrm{CE}(\lambda)\, \mathrm{d}\lambda, \tag{4.1}$$

where $\lambda_0 = 1550\,\mathrm{nm}$ and $\Delta\lambda = 10\,\mathrm{nm}$. This broadband formulation penalizes spectral sensitivity: a design that achieves high efficiency only over an extremely narrow band is inherently susceptible to lithographic feature-size biases, which manifest as a correlated shift of all grating tooth and gap widths and, equivalently, as a shift in the effective Bragg condition [151]. Requiring the optimizer to sustain high CE over a finite bandwidth therefore confers intrinsic tolerance to such fabrication errors. The quantitative impact of this choice is verified a posteriori in Section 4.5.

Each Sb_2S_3 enhancer layer comprises 50 grating periods. The etched width $w^{(\ell)}_{\mathrm{etch},i}$ and the unetched (tooth) width $w^{(\ell)}_{\mathrm{tooth},i}$ of the i-th period in layer ℓ ($\ell \in \{1, 2\}$, $i \in \{1, \ldots, 50\}$) are independently optimized, yielding 200 geometric parameters. This per-period parametrization allows the local duty cycle and period to vary along the grating aperture, enabling apodization of the scattered field amplitude to match the Gaussian envelope of the incident beam [151, 150]. Both layers are initialized with a uniform pitch of 580 nm and a duty cycle of 0.5.

Three additional parameters are co-optimized with the grating geometry. The independent lateral offsets of the two Sb_2S_3 layers with respect to the host waveguide set the phase relationship between fields scattered by the two layers, controlling lateral constructive interference into the guided mode. The vertical separation between the silicon device layer and the first Sb_2S_3 enhancer (the spacer thickness) controls the vertical phase-matching condition; during optimization, this parameter converged to its lower bound of 235 nm, indicating that a thinner spacer maximizes the near-

field interaction between the waveguide mode and the augmentation layers. The in-plane position of the Gaussian source relative to the grating aperture affects the overlap between the incident field profile and the inverse-designed grating scattering envelope, and is therefore included as an optimization variable rather than fixed by hand. The total parameter count is 204.

Gradients of $\mathcal{F}$ with respect to all 204 parameters are computed at each iteration using the adjoint method as implemented in Tidy3D [173], with automatic differentiation of the mode-overlap post-processing provided by Autograd [165]. Each iteration requires exactly one forward and one adjoint FDTD simulation, making the per-iteration cost independent of the number of free parameters. The Adam update rule used for maximization is

$$\mathbf{p}_{t+1} \;=\; \mathbf{p}_t \;+\; \alpha \,\frac{\hat{\mathbf{m}}_t}{\sqrt{\hat{\mathbf{v}}_t} + \epsilon}, \tag{4.2}$$

where $\hat{\mathbf{m}}_t$ and $\hat{\mathbf{v}}_t$ are the bias-corrected first- and second-moment estimates of the gradient, α is the learning rate, and ϵ is a small constant for numerical stability [166]. By scaling the effective step size for each parameter inversely with the square root of its historical gradient variance, Adam assigns larger updates to parameters in flat directions of the loss landscape and damps updates in steep directions. The accumulated first-moment term carries directional gradient information across iterations, facilitating escape from shallow local minima that would trap a standard gradient-descent scheme. For this reason, Adam is chosen over classical gradient descent in this work. Optimization is performed using the Adam optimizer as implemented in `optax`, run for 2750 iterations at a learning rate of $\alpha = 10^{-2}$. The remaining Adam hyperparameters are left at their `optax` defaults: $\beta_1 = 0.9$, $\beta_2 = 0.999$, and $\epsilon = 10^{-8}$.

4.4 Results

Figure 4.2 shows the evolution of $\mathcal{F}$ over 2750 optimizer iterations. Three qualitatively distinct phases are evident. The objective first rises rapidly from its initial value to an early maximum near $\mathcal{F} \approx 0.32$, after which Adam escapes this shallow optimum. The escape is driven by the first-moment (momentum) term in Eq. (4.2): the optimizer has accumulated a consistent gradient direction during the initial rise and overshoots the local optimum, causing the objective to drop sharply as the parameter configuration enters a destructively interfering regime. This behavior distinguishes Adam from standard gradient descent, which would have settled at the first encountered local optimum.

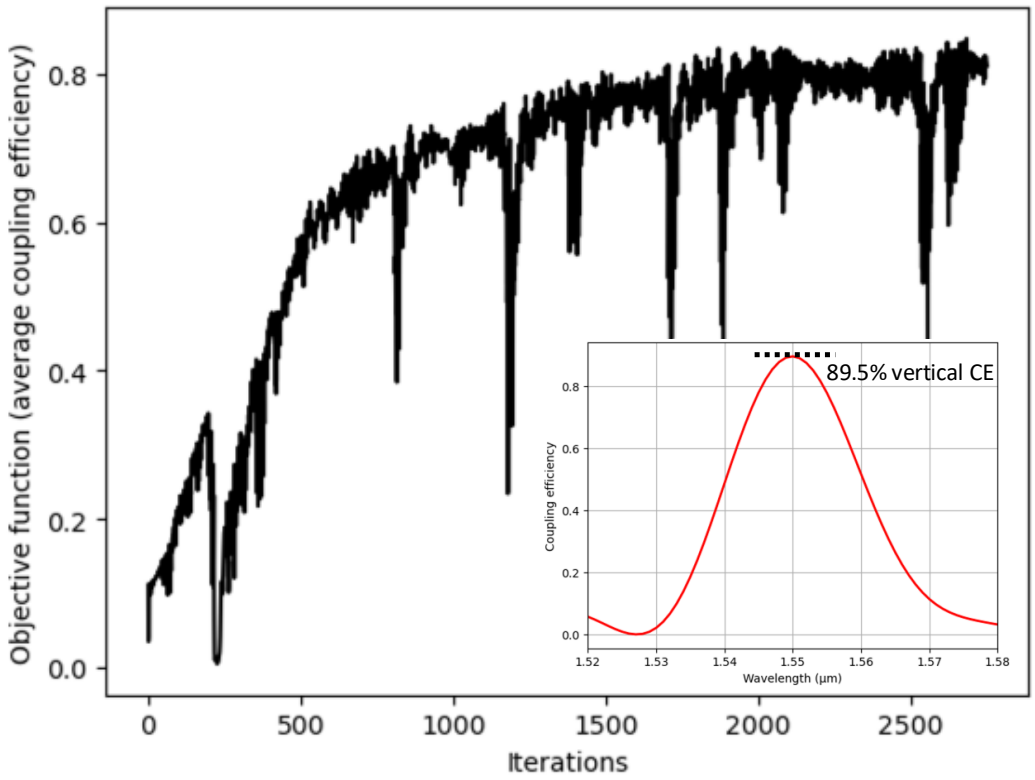


Figure 4.2: **Convergence of the adjoint optimization and final coupling efficiency spectrum.** Evolution of the bandwidth-averaged objective $\mathcal{F}$ in Eq. (4.1) over 2750 Adam iterations. The trajectory exhibits a rapid initial rise, a momentum-driven escape from a shallow local optimum near $\mathcal{F} \approx 0.32$, and convergence to a plateau in the range 0.80–0.83. The inset shows the simulated CE spectrum of the final design (parameter set from iteration 2682, the maximum among 2750), showing a peak CE of 89.5% (−0.48 dB) at 1550 nm and a 3-dB bandwidth of approximately 22 nm.

Following the escape, $\mathcal{F}$ rises steadily, reflecting the progressive co-refinement of the grating apodization profile and the inter-layer phase relationships across all 204 geometric parameters. Superimposed on the overall upward trend are transient dips in the figure of merit. These dips arise from the interplay between Adam's momentum and the non-convex loss landscape: when the optimizer overshoots a ridge in parameter space, the objective temporarily degrades before the adaptive second-moment correction redirects the trajectory toward a better configuration. The objective eventually plateaus and oscillates in the range $\mathcal{F} \approx 0.80$–0.83. We adopt the parameter set at iteration 2682, the maximum encountered during the

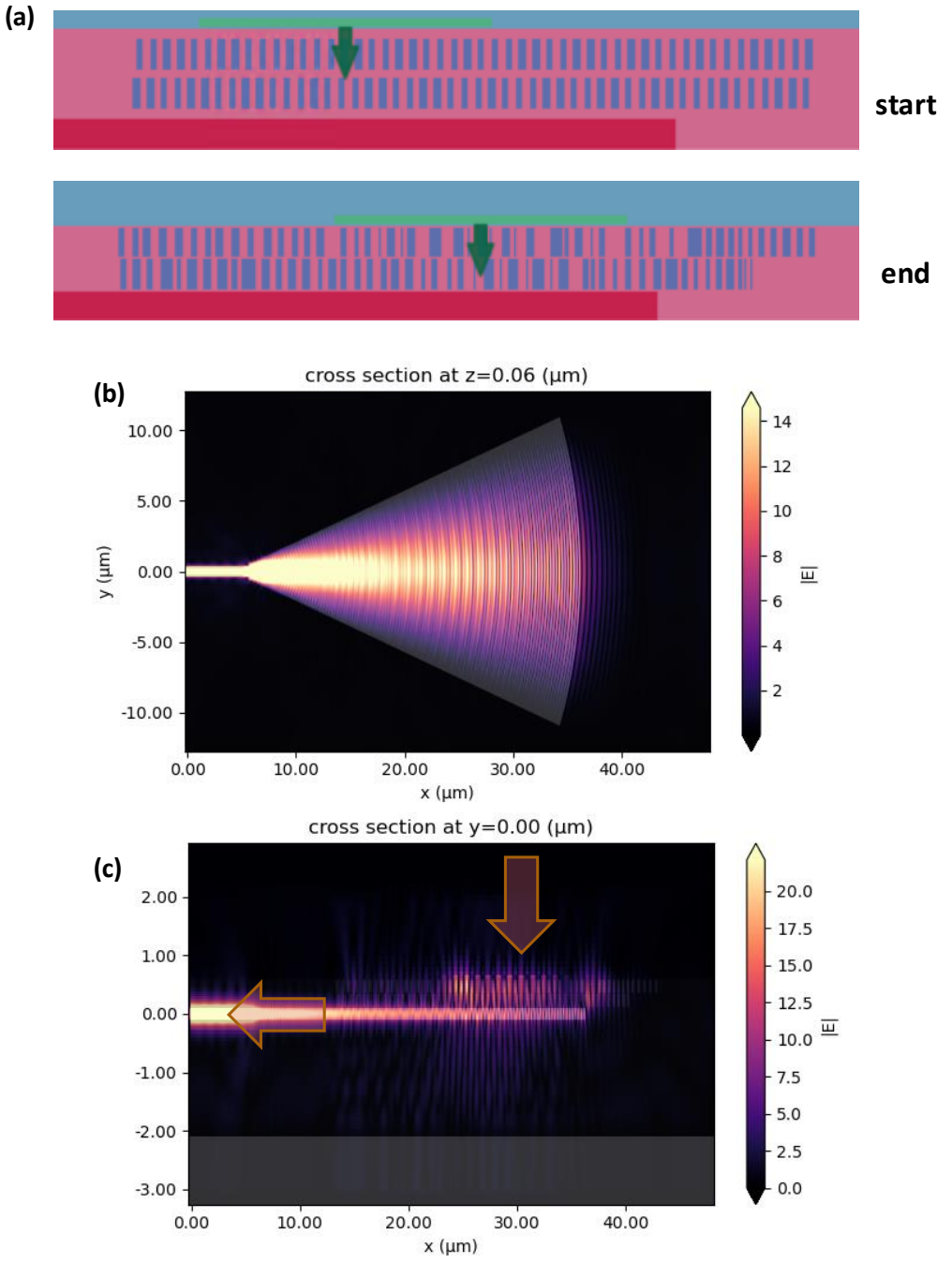


Figure 4.3: **Optimized grating coupler geometry and electric field distribution.**(a) Cross-sectional view of the multilayer vertical grating coupler at the start (top) and end (bottom) of the optimization, showing the optimized grating-element widths, source position, and lateral enhancer-layer offsets. (b,c) Electric-field amplitude at 1550 nm for vertically incident light, shown in (b) top view at the level of the silicon waveguide and (c) side view through the device center.

2750-iteration run, as the final design.

The simulated CE spectrum of the optimized structure is shown in Figure 4.2 inset. A smooth, near-Gaussian lineshape is centered at 1550 nm with a peak value of 89.5% (−0.48 dB) and a 3-dB bandwidth of approximately 22 nm. The absence of sharp spectral features confirms that the design exploits broadband constructive interference between the two Sb_2S_3 enhancer layers rather than a narrow-band resonance, consistent with the design intent of the bandwidth-averaged objective in Eq. (4.1). Figure 4.3.a shows the cross-sectional geometry of the device at the start and end of the optimization, illustrating the substantial reshaping of both grating layers and the convergence of the lateral offsets and source position. Figure 4.3.b,c show the electric-field amplitude at 1550 nm in top and side views, respectively. The field is strongly concentrated within the two Sb_2S_3 layers and along the underlying silicon waveguide; the near absence of downward-propagating field beneath the buried oxide confirms that the augmentation stack successfully redirects the scattered power into the waveguide rather than into the substrate.

To complete the description of where the incident power is routed, we report that power transmitted into the fundamental TE waveguide mode (the CE) is 89.5%, power reflected upward into the free-space half-space above the device is approximately $\sim$ 2%, power transmitted downward into the substrate beneath the BOX is approximately $\sim$ 8.5%.

4.5 Fabrication-tolerance Analysis

For a design that does not yet have an experimental counterpart, the strongest evidence of practical relevance is its robustness to the deviations that the structure will inevitably experience during fabrication. We therefore perform a series of cumulative-deviation checks in which the nominal design is perturbed simultaneously along several physically realistic axes, and the CE spectrum is recomputed without re-optimizing any parameter.

Four perturbation axes are considered: (i) deviation in HSQ spacer thickness, representing variability in the ICP-RIE blanket-etch endpoint; (ii) deviation in the silicon device-layer thickness, representing wafer-to-wafer variation of PECVD deposition; (iii) a uniform lateral feature-size bias applied to all tooth and gap widths in both Sb_2S_3 layers, representing exposure-dose or proximity-effect-correction inaccuracy in the direct-write lithography; and (iv) deviation in the HSQ refractive index, representing variability in the post-cure stoichiometry. Each perturbation is applied

cumulatively, so the last plot in Figure 4.4 corresponds to the design subjected to all four deviations simultaneously.

The principal result is that even under cumulative deviations on all four axes, the device retains a simulated peak CE of approximately 50% (Appendix, Figure 4.4). The amounts of deviations applied and showed in Figure 4.4 reflects the discrepancies observed during experimetal efforts. The effect of having a thicker t_{HSQ} shows itself as a 7% drop in the maximum coupling efficiency. On the other hand, the dominant effect of deviation from the target silicon photonic circuit thickness is to shift the spectral peak in wavelength rather than to suppress its magnitude due to the effective index change of the guided mode. When we also add a fabricated lateral feature size bias on top, it results with both a coupling wavelength band shift and a 38% maximum coupling efficiency drop, which is more significant than any effect explored in this section. The lateral feature size bias applied to the original design parameters are determined based on the measured feature sizes after SEM imaging the samples fabricated with the Sb_2S_3 based direct e-beam write platform. The applied feature size bias varies with the feature size itself and an interpolation is applied based on the observations: 100 nm features appear $\sim$ 30 nm; 190 nm features appear $\sim$ 15 nm; and 230 nm features appear $\sim$ 7 nm larger where features above 350 nm have no positive or negative bias. The spatially varying deviations in the individually optimized grating unit feature sizes modifies the full scattering picture which results with a more significant efficiency drop. Finally, the HSQ refractive index n_{HS} is also changed from the nominal 1.40 index to 1.45, which results with a slight coupling wavelength band shift in the spectrum. These effects preserve the broadband interference mechanism on which the design relies and are therefore well tolerated by the bandwidth-averaged objective of Eq. (4.1). A 50% peak CE (-3 dB) is readily measurable in a standard fiber-to-chip-to-fiber loop-back measurement and is well above the typical noise floor of a tunable-laser/photodiode characterization setup [78].

By contrast, the design is more sensitive to deviations in the refractive indices of the silicon device layer and of the direct-patterned Sb_2S_3 film (Appendix, Figure 4.4). This sensitivity is expected: n_{Si} and $n_{\mathrm{Sb_2S_3}}$ jointly govern the effective index of the guided mode and the scattering strength of the augmentation grating, and unlike geometric tolerances, they modify both the scattering amplitude and the interference condition. n_{Si} is well characterized for commercial SOI wafers and is not expected to deviate appreciably from the value used here. $n_{\mathrm{Sb_2S_3}}$, on the other hand, is relatively

more sensitive to the synthesis and the conditions of the direct-write process and can vary by several percent between samples [78, 176]. To mitigate this, design variants are pre-generated for nominal indices in the range $n = 2.0$–2.2 in steps of $\Delta n = 0.05$, planned to be fabricated alongside the baseline design, and selected a posteriori based on the measured film index. Importantly, this strategy does not alter the design framework itself; the robustness of the bandwidth-averaged objective ensures that each index-specific variant retains the geometric tolerance demonstrated above.

4.6 Discussion

Augmented grating couplers that impose no circuit-level modifications on the host PIC are less explored than conventional invasive couplers, in part because prior augmentation demonstrations have generally achieved lower coupling efficiencies than their invasive counterparts [158, 159, 160, 161]. The present design, with a simulated peak CE of 89.5% (−0.48 dB), falls within the top tier of *all* grating-coupler designs catalogued in Table 4.1 and, to our knowledge, is the highest reported peak CE for a non-invasive augmentation grating coupler in the C-band. Four design choices drive this performance. First, the Adam optimizer's momentum-driven dynamics allow it to escape the shallow local optima that trap classical gradient descent, as evidenced by the trajectory in Figure 4.2.a. Second, co-optimizing all 200 tooth-and-gap parameters jointly with the source position and inter-layer offsets exposes a much larger fraction of the relevant design space than the uniform or monotonically apodized parametrizations used in many earlier shape-based studies [150, 151]. Third, the two-layer augmentation provides additional degrees of freedom, in particular, the inter-layer phase, that single-layer designs simply do not have access to [169]. Fourth, the moderate refractive index of Sb_2S_3 ($n \approx 2.2$) compared with silicon ($n \approx 3.48$) reduces the impedance mismatch at the free-space/grating interface, suppressing upward back-reflection relative to direct-etch silicon gratings with higher refractive index.

Among the works in Table 4.1, only Huang & Barz [181] report a higher simulated peak CE (−0.35 dB), using topology optimization combined with an integrated back-mirror. We expect that, when reduced to practice, the present design will compare favorably for two reasons. First, the topology-optimized geometries of Ref. [181] contain sub-wavelength freeform features whose fabrication accuracy is limited by lithographic resolution and proximity-effect-correction fidelity; the present shape-optimized geometry is parametrized by tooth and gap widths that are

Table 4.1: Summary of grating coupler designs reported in the literature, including peak coupling efficiency, optimization method, and primary design objective.

Reference	**Peak CE (dB)**	**Optimization Method**	**Primary Objective**
Chen et al. [179]	−3.97[a]	Inverse design	High CE; fabrication tolerance
Hammond et al. [169]	−4.7 / −7.0[b]	Topology optimization	Foundry-compatible; dual polarization
Hansen et al. [180]	−6.6[a]/ −7.2[b]	Shape optimization	High CE; low back-reflection
Huang & Barz [181]	−0.35[a]	Topology optimization	Sub-dB CE; compact footprint
Jin et al. [182]	−2.0[a]/ −2.8[b]	Gradient-based optimization	Perfectly vertical; CMOS compatible
Marchetti et al. [151]	−0.8[a]/ −0.9[b]	Parameter sweep (apodized)	Peak CE without back-reflector
Sapra et al. [167]	−3.0 to −5.4[a]	Gradient-based inverse design	Broadband (>100 nm 3-dB bandwidth)
Shen et al. [183]	−0.65[a]	Nonlinear optimization	Compact coupler; polarization splitting
Van Lange et al. [184]	−9.2[b]	Analytical / parameter sweep	Free-space top-coupling for atom–photonic arrays
Xiong et al. [185]	−5.2[b]	Parameter sweep + metalens	Compact; achromatic S/C/L-band operation
Yang et al. [186]	−5.86[b]	Gradient-based inverse design	Perfectly vertical; back-reflection suppression
Zhong et al. [187]	−0.54 (TE)[a]	Adjoint-based inverse design	High CE; O-band TE and TM operation

[a] Simulated value.
[b] Experimental value. Where both are listed, simulated is given first.

individually well-resolved on a typical e-beam tool. Second, the integrated back-mirror of Ref. [181] requires backside processing or a buried metal layer, neither of which is available in a locked foundry process, whereas the present design adds only top-side patterned layers and is therefore compatible with deployed photonic chips. The remaining sub-dB designs in the table [151, 183, 187] are likewise invasive and either etch directly into the silicon layer or require multi-step etches of the silicon device layer.

A few caveats temper the present results and motivate near-term follow-on work. First, the design's sensitivity to the Sb_2S_3 refractive index (Section 4.5) means that experimental validation will need to be accompanied by careful film characterization, and the design-variant strategy outlined above will be used to bracket the as-deposited index. In addition, the present analysis treats the augmentation grating in isolation. In a deployed PIC, the coupler will sit adjacent to other components and the augmentation layers will extend over the full chip; cross-talk between adjacent couplers and the effect of a continuous top-side HSQ/Sb_2S_3 film on nearby waveguides will need to be evaluated separately. Although the effect of this is expected to be negligible as HSQ is chemically and optically very similar to a typical SiO_2 cladding, and the Sb_2S_3 grating coupler has a small footprint minimizing its intearction with other parts of the photonic circuit.

Because the photonic circuit is never altered in this work, the same waveguide layout can host different sets of augmentation layers tailored to distinct application requirements including oblique coupling for Doppler LiDAR, broadband coupling for wavelength-division-multiplexed systems, or polarization-insensitive coupling for coherent receivers, without requiring a new mask tape-out of the underlying silicon layer. We view this re-targetability, more than any single peak-efficiency number, as the most consequential implication of the augmentation framework demonstrated here.

4.7 Conclusion

We have presented a design study of an augmented two-layer Sb_2S_3 grating coupler that achieves a simulated peak coupling efficiency of 89.5% (−0.48 dB) at 1550 nm with a 3-dB bandwidth of 22 nm. The structure is engineered to sit on top of an existing SOI photonic circuit without any modification of the underlying device layer; the only requirement on the host PIC is a standard feature-free taper terminating the waveguide into the grating region. The design is obtained by adjoint-based shape

optimization with the Adam optimizer in Tidy3D, simultaneously co-optimizing 204 geometric and source-position parameters under a bandwidth-averaged figure of merit that intrinsically confers tolerance to lithographic feature-size biases. A cumulative-deviation tolerance analysis confirms that the design retains $\geq 50\%$ peak CE under simultaneous deviations in spacer thickness, silicon thickness, and lateral feature size, supporting its experimental viability. The augmentation paradigm, combined with a manufacturability-aware parametric design space, provides a scalable, high-efficiency coupling solution that is in principle compatible with post-fabrication augmentation of deployed photonic chips and with the locked process flows of commercial silicon-photonics foundries.

4.8 Appendix

The adjoint method implemented in tidy3D, combined with AUTOGRAD for differentiating through the mode-overlap post-processing chain, renders a 204-dimensional optimization tractable within a realistic simulation budget [173, 165]. The broadband objective function in Eq. (4.1) serves a dual purpose: it provides a smoother gradient signal compared with a single-frequency objective, and it naturally encodes fabrication robustness by penalizing spectral sensitivity. This can be seen in Figure 4.4.a. Even when four different parameters (HSQ thickness, Si layer thickness, lateral fab bias and HSQ refractive index), we can get a 50% coupling. On the other hand, the design seems sensitive to the refractive index discrepancies for Si and Sb_2S_3 as can be seen in Figure 4.4.b. This can be understood by noting that the refractive indices of these two materials directly govern the effective index of the guided mode and the scattering strength of the grating teeth, respectively. Unlike geometric tolerances such as linewidth bias or layer thickness, which predominantly shift the coupling efficiency peak in wavelength while preserving its magnitude, a refractive index error modifies both the scattering amplitude and the interference condition.

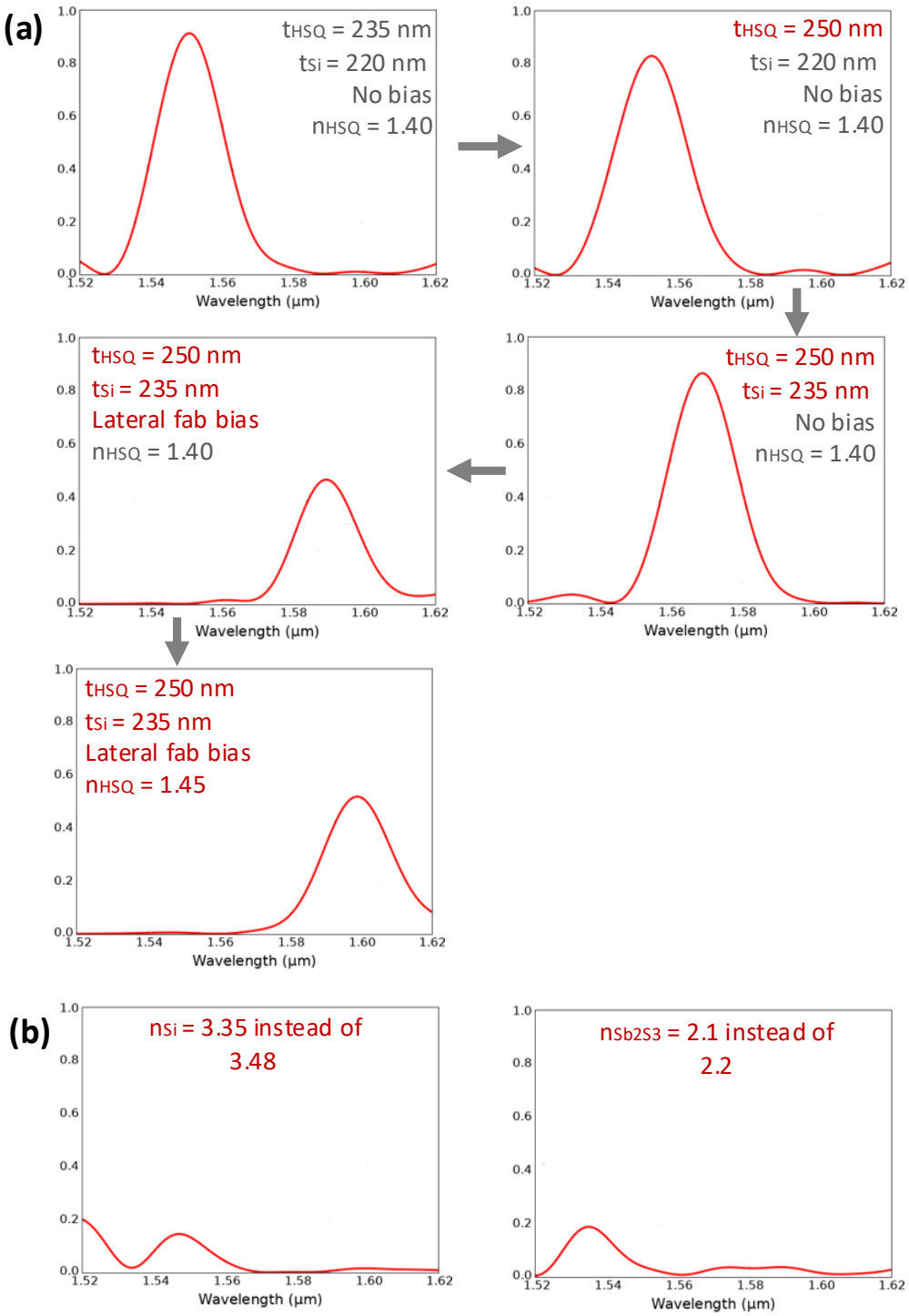


Figure 4.4: **Fabrication tolerance analysis for the optimized grating coupler.** (a) Coupling efficiency (CE) for the nominal design and for cumulative deviations (text given in red represents the deviations shown at each step) for the in HSQ thickness, Si thickness, lateral feature size, and HSQ refractive index. (b) CE for Si and Sb_2S_3 refractive index deviations.

Chapter 5

MULTILAYER BAYER COLOR ROUTER IN THE VISIBLE VIA DIRECT-WRITE E-BEAM LITHOGRAPHY

The material in this chapter is part of an ongoing collaboration with Ian Foo and will be presented in Ref. [188].

Conventional CMOS color image sensors employ Bayer color filter arrays in which dye-based or thin-film absorptive filters discard roughly two-thirds of the incident visible light to assign each pixel a single color channel. Volumetric metaa-optics as color routers offer a fundamentally different approach: rather than rejecting the unwanted spectral content, a multilayer dielectric structure is inverse-designed to spatially redirect each wavelength band toward a different sub-pixel of the detector array, in principle preserving the full incident photon budget. Demonstrating such routers in the visible spectrum requires a fabrication platform capable of producing many densely stacked patterned dielectric layers with sub-wavelength feature sizes. In this chapter, we apply the Sb_2S_3 direct-write electron-beam lithography platform introduced in Chapter 3 to the design and fabrication of ten-layer Bayer color routers operating at visible wavelengths. Six device variants are designed by adjoint-based optimization, spanning Sb_2S_3 refractive indices of $n = 2.0$, 2.1, and 2.2 and two RGB design wavelength sets centered on $(475, 550, 650)$ nm and $(550, 650, 750)$ nm. The devices are fabricated on a transparent doped-SiC substrate selected to support the high electron-beam doses required for the precursor chemistry while remaining sufficiently transmissive in the visible. This work is ongoing; experimental characterization is in progress, and we present here the design framework, the fabricated device set, and the simulated routing performance.

5.1 Introduction

Color image sensors built around Bayer-pattern absorptive filter arrays are nearly universal in consumer and scientific imaging, but the underlying paradigm is intrinsically lossy: each pixel records only one of the three primary color channels and discards the remaining incident light [83, 189, 190]. Each filter discards roughly two-thirds of the incident photons, directly reducing the signal-to-noise ratio, particularly under low-light conditions. Smaller pixel sizes in modern CMOS image sensors exacerbate these problems: as pixel dimensions approach the diffraction limit, photon

collection per pixel decreases, optical crosstalk between adjacent pixels intensifies, and the signal-to-noise ratio degrades substantially [191, 192, 193], which makes it hard to miniaturize pixels in image sensors to increase imaging resolution. Meta-optics can tackle this problem by optimizing the design space to minimize crosstalk to achieve smaller pixel sizes. Replacing absorptive filters with dispersive optical elements that spatially separate, rather than absorb, the spectral content has therefore emerged as a compelling route toward higher-throughput color imaging. Diffractive and metasurface-based color routers have been demonstrated using a range of architectures, including color-sorting metalenses [194], dispersion-engineered dielectric gratings [195], cascaded Huygens metasurfaces [83], and freeform inverse-designed structures [36, 85, 189, 190]. Among these, three-dimensional volumetric routers offer the largest design space with more degrees of freedom to engineer, and have been shown to outperform single-layer counterparts in routing efficiency and angular response [85, 29].

Despite their attractive performance, volumetric color routers in the visible spectrum remain difficult to fabricate. Two-photon lithography supports true three-dimensional patterning but is restricted to low-index polymers and has limited resolution where the minimum feature size is typically 500 nm [196], limiting the achievable contrast and routing efficiency for sub-wavelength visible features [85, 189, 197]. Conventional multilayer nanofabrication using high-index dielectrics such as TiO_2 or amorphous silicon requires repeated cycles of deposition, lithography, etching, and planarization, which becomes prohibitively expensive and low-yield as the layer count grows beyond a few. The Sb_2S_3 direct-write platform introduced in Chapter 3 [78] addresses this gap directly by patterning the high-index optical material in situ during electron-beam exposure, eliminating per-layer deposition and etch cycles and reducing each layer to a spincoat-expose-develop-planarize sequence. In Chapters 3 and 4, this platform was used to realize devices with a small number of patterned Sb_2S_3 layers (three resonant filter layers and two grating-coupler layers, respectively). Here we extend it to a substantially deeper stack of ten patterned Sb_2S_3 layers, demonstrating that the platform supports the layer counts and minimum feature sizes required for visible-band volumetric color routing.

5.2 Device Architecture

Although single layer inverse design color routers were demonstrated before using advanced optimization techniques [189, 190, 83], the free-form, multilayer meta-materials overperform their single layer counterparts as they provide more degrees

of freedom to engineer. Although such devices have been explored extensively in infra-red spectrum through fabrication techniques such as two-photon polymerization lithography, such designs in the visible have not been yet explored due to the difficulty in fabricating high resolution multilayer photonic devices that require high resolution patterning tools like e-beam lithography, and hence the full standard nanofabrication cycle. To our knowledge, this is first exploration of the free-form multilayer metaoptics to realize multilayer Bayer filter color routers in the visible spectrum, and this precursor based direct write lithography platforms makes that possible by simplifying the fabrication process and increasing the yield.

The device is a 4 μm $\times$ 4 μm $\times$ 6.325 μm volumetric Bayer router consisting of ten patterned Sb_2S_3 layers separated by nine HSQ planarization spacers. Each Sb_2S_3 layer is 340 nm thick, and each layer-plus-spacer unit cell in the vertical direction is 665 nm thick (corresponding to a 325 nm HSQ spacer above each Sb_2S_3 layer), and the minimum lateral feature size is set to 115 nm. The device is designed to focus and route the red, green, and blue spectral bands to spatially separated quadrants of a focal plane located below the substrate, mimicking the layout of a conventional Bayer color filter pixel cluster.

A central practical constraint of the Sb_2S_3 direct-write platform is the very high electron-beam dose required to drive the precursor decomposition reaction (a total accumulated dose of $\sim$ 500 mC/cm^2, as detailed in Chapter 3). For thin-film resist patterning, using a conductive antistatic agent over the resit layer, or a thin ITO layer on a glass substrate is the standard transparent conductive coating used to mitigate substrate charging during electron-beam exposure. However, at the doses required here, the ITO/glass combination proved insufficient: the ITO film is too thin to dissipate the accumulated charge due to the large exposure doses, leading to pattern distortion. Although different thicknesses of ITO films with reactivities as low as 20 ohm/sq are used, the experiments proved the need for a bulk conductive substrate rather than a thin film. To circumvent this limitation while retaining transparency in the visible, we adopt a bulk doped silicon carbide (SiC) wafer as the substrate with low resistivity. The bulk doping provides a continuous, low-resistance path for charge dissipation throughout the entire device write, while the SiC remains substantially transmissive in the majority of the visible spectrum. The principal limitation of this choice is that SiC absorbs significantly below $\sim$ 500 nm due to doping, which directly motivates the exploration of design wavelength sets centered above this absorption edge, as described below.

5.3 Inverse Design and Optimization

The ten-layer routers are designed by adjoint-based gradient optimization within a finite-difference time-domain (FDTD) framework, using an Adam optimizer [166], similar to the one employed in Chapter 4 for the vertical grating coupler. The simulation setup mirrors that of the previous Sb_2S_3 devices in this thesis: a normally incident Gaussian excitation with an 85 μm waist radius (effectively a plane wave at the device aperture) illuminates the structure from above; perfectly matched layer (PML) boundary conditions terminate all six faces of the simulation domain. Sb_2S_3 is treated as lossless with a single-valued real refractive index in the design band, and HSQ is treated as a lossless spacer with $n_{\mathrm{HSQ}} = 1.4$. Transmission into each color quadrant is normalized to the total power transmitted through an aperture of identical lateral dimensions in the absence of the device. The Adam optimizer is run with a learning rate of 0.01 and updates the in-plane Sb_2S_3 pattern of every layer simultaneously, so that interlayer coupling and constructive interference between layers are exploited rather than treated as parasitic effects.

Six device variants were generated to span the practical uncertainty in the as-deposited Sb_2S_3 refractive index and to evaluate two distinct visible-band design targets. The Sb_2S_3 index was swept across $n = 2.0$, 2.1, and 2.2, bracketing the values reported for the precursor-derived films in Chapter 3. Two RGB design wavelength sets were evaluated: $(475, 550, 650)$ nm, which targets a conventional R/G/B partition centered near the eye's photopic response; and $(550, 650, 750)$ nm, which is shifted to longer wavelengths to remain entirely within the high-transmission window of the SiC substrate. Each combination of $(n, \lambda_{\mathrm{RGB}})$ yields one full ten-layer optimization, for a total of six fabricated designs.

5.4 Fabrication

Fabrication follows the Sb_2S_3 direct-write process described in Chapter 3, with the substrate replaced by the bulk doped SiC wafer described above. After substrate cleaning and gold-marker patterning, each of the ten Sb_2S_3 layers is fabricated by (i) spin-coating the antimony-BDCA precursor solution (twice, to reach the target post-decomposition thickness of 340 nm), (ii) electron-beam exposure at 100 kV using the multipass strategy described in Chapter 3, (iii) IPA development and a brief annealing step to complete the precursor-to-Sb_2S_3 conversion, and (iv) spin-coating of an HSQ planarization layer followed by annealing for partial curing of the HSQ planarization layer. The same set of gold alignment markers patterned at the substrate level is reused for all ten layers, and interlayer registration is set by the

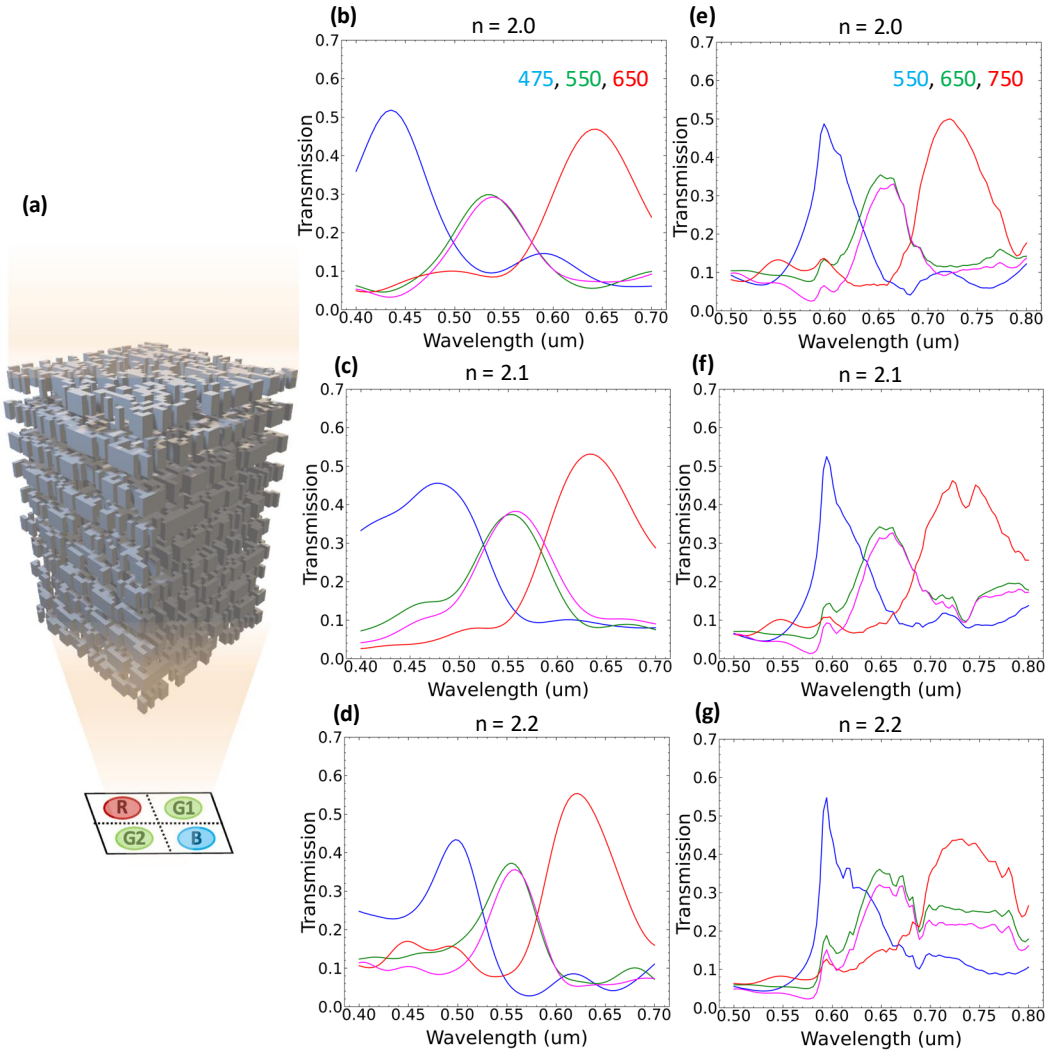


Figure 5.1: **Visible Bayer filter transmission spectra for different device design configuration.** (a) Ten layer Bayer filter optimized for n = 2.1 and (475, 550, 650) nm. Transmission spectrum for (b) n = 2.0 and (475, 550, 650) nm, (c) n = 2.1 and (475, 550, 650) nm, (d) n = 2.2 and (475, 550, 650) nm, (e) n = 2.0 and (550, 650, 750) nm, (f) n = 2.1 and (550, 650, 750) nm, (g) n = 2.2 and (550, 650, 750) nm. Red, green, pink and blue curves represent the R, G1, G2, and B.

lithographic alignment accuracy ($\lesssim$ 10 nm) of the EBL tool. The minimum patterned feature size of 115 nm is well within the resolution demonstrated previously for this precursor chemistry.

The resulting stack consists of ten layers of patterned Sb_2S_3 separated by nine HSQ spacers, with no deposition or etch step performed at any point in the process.

5.5 Design and Results

The simulated transmission spectra for the six fabricated device variants are presented in Figure 5.1, showing the routing efficiency into each of the R, G1, G2, and B quadrants as a function of wavelength for each combination of (n, λ_{RGB}). G1 and G2 channels mimick the two subpixels allocated to green color in conventional Bayer filters used in CMOS sensors as human eye is more susceptible to green compared to other colors (Figure 5.1.a). The designs given in Figure 5.1.b, c, and d assume Sb_2S_3 refractive index to be 2.0, 2.1 and 2.2 respectively for $(475, 550, 650)$ nm central design wavelengths while assuming no SiC absorption. The transmission spectra given in Figure 5.1 are normalized with respect to the total input power hitting the device aperture. Similarly, the designs given in Figure 5.1.e, f, and g assume Sb_2S_3 refractive index to be 2.0, 2.1 and 2.2 respectively for $(550, 650, 750)$ nm central design wavelengths while assuming nonzero k for SiC, which constitutes a more realistic modeling. That results with less symmetric transmission curves, especially for the B band, as the optimization tries to push the transmission bands to longer wavelength where there is less absorption, which is visible in Figure 5.1.e, f, and g. This has been done since it is not trivial to characterize the real and imaginary parts of the bulk SiC refractive index.

The two design wavelength sets produce qualitatively different responses: the

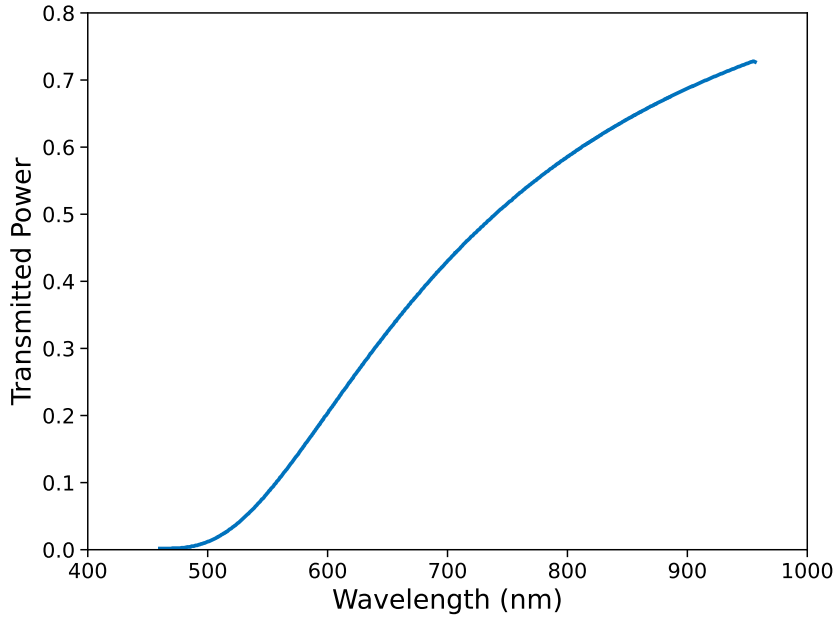


Figure 5.2: **Transmission through the doped SiC bulk substrate.** Simulated transmission through the 0.3 mm thick doped SiC substrate

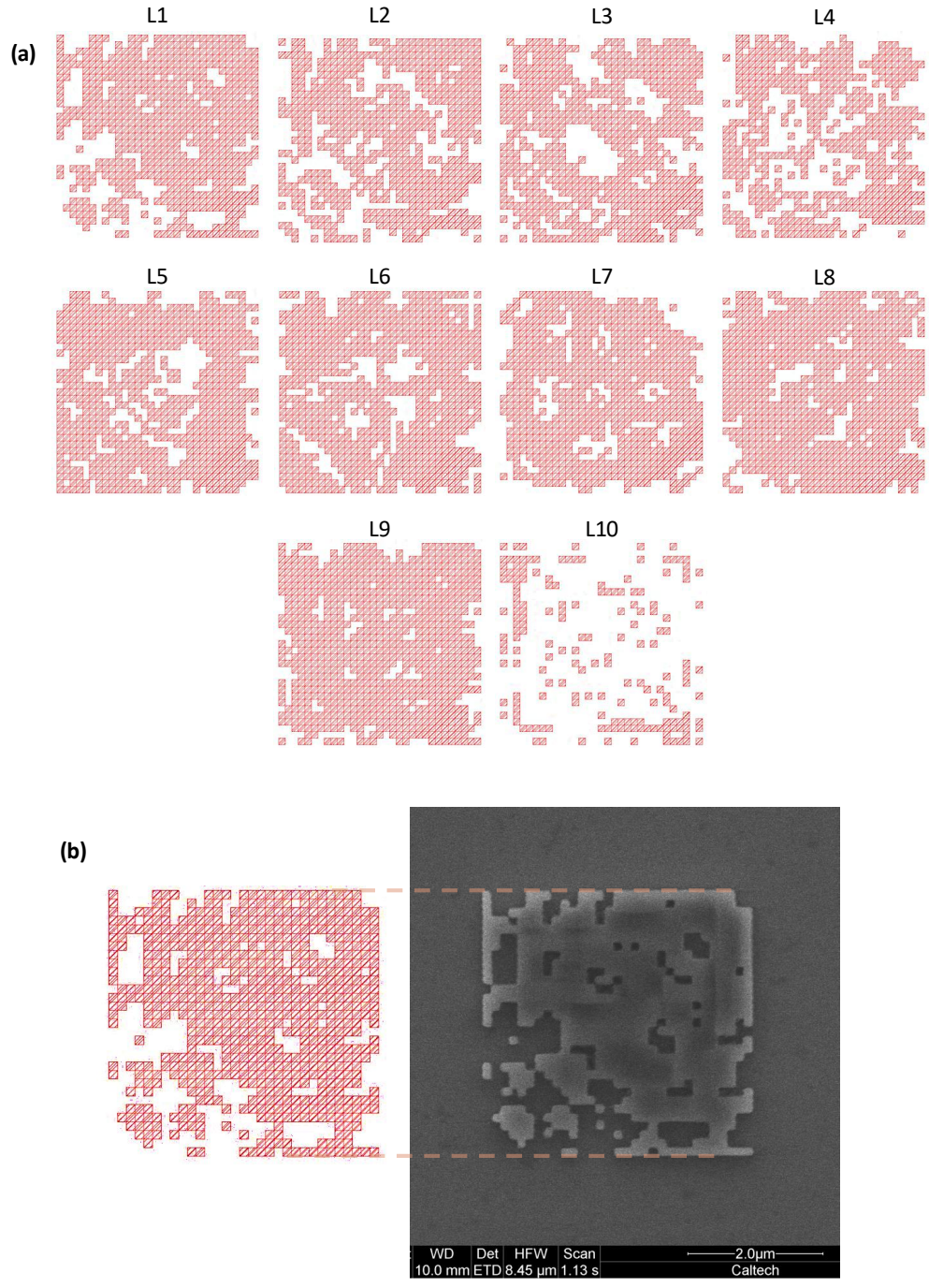


Figure 5.3: **Layers of the optimized design.** (a) Layers of the optimized design with Sb_2S_3 index of 2.2 and SiC loss, L1 represents the bottom layer and L10 represents the top layer. (b) Designed bottom layer given in a and the SEM image of the fabricated layer.

(475, 550, 650) nm designs spread the routed bands more evenly across the visible but partially overlap with the SiC absorption edge, while the (550, 650, 750) nm designs achieve cleaner spectral separation at the cost of shifting the blue channel into the green-yellow range. While different designs with the refractive indices 2.0, 2.1, and 2.2 are considered for the discrepancies in the fabricated Sb_2S_3 thin film refractive index, the choice of design wavelengths is directly motivated by the SiC substrate transmission. Transmission of the bare doped-SiC wafer as a function of wavelength can be seen in Figure 5.2 based on complex refractive index data available online. The substrate transmission decreases sharply below $\sim$ 500 nm and remains high through the rest of the visible, which sets the practical lower bound on the design wavelengths and motivates the longer-wavelength variant. As the complex refractive index of the SiC substrate can change with the purity in addition to doping type, and concentration, we designed for two aforementioned wavelength sets. The wavelength set (550, 650, 750) nm guarantees a 10% transmission in blue if the current refractive index agrees with the reported data, which makes experimental verification possible. Each design is fabricated with 6 different EBL feature size biases, and the measurements on the fabricated devices are ongoing.

The layers of the optimized design given in Figure 5.1.g can be seen in Figure 5.3.a. Due to the high electrical conductivity of the doped SiC substrate, the fabricated layers are consistent with the design patterns. Fabricated first layer (L1) is given in Figure 5.3.b, and it can be seen that although the design consists of non-intuitive shapes and sharp corners, it is translated well to the fabricated design through direct electron beam lithography write method.

In our preliminary experimental results, we observe that the trend in terms of the peak efficiencies for each R, G1, G2, and B quadrants, as well as the peak wavelengths (Figure 5.4.c), agree with the simulation results, except for a small $\approx$ 10 nm spectral shift in the B quadrant (Figure 5.4.b). The simulated sorting efficiency shown in Figure 5.4.b is calculated by the transmission in each quadrant (Figure 5.1.g) normalized by the total power in the focal plane. For this measurement, a spectrometer-based transmission setup was used, and the sorting efficiencies were calculated by taking the transmission per each quadrant and normalizing it with respect to the total power sent to the device aperture. We are currently working on the imaging results of this color sorting, but the simulation results show the color sorting for 593, 658 and 730 nm in their respective quadrants (Figure 5.4.a).

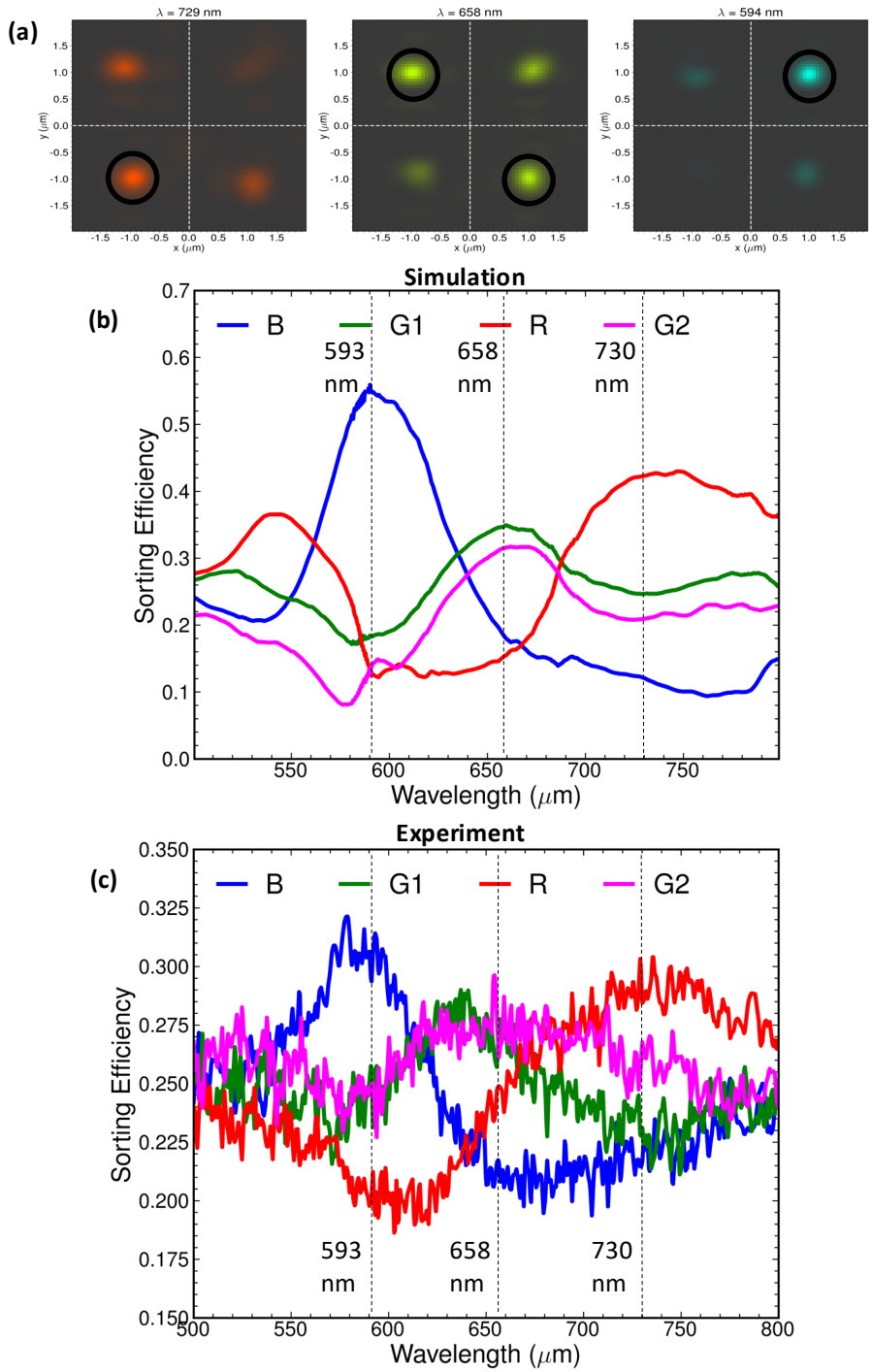


Figure 5.4: **Preliminary experimental results.** (a) Simulated color sorting for R, G1 & G2, and B quadrants respectively. (b) Simulated device transmission given in Figure 5.1.g and the peak wavelength locations. (c) The preliminary experimental sorting efficiency result with simulated peak wavelengths marked.

5.6 Conclusion and Outlook

We have applied the Sb_2S_3 direct-write electron-beam lithography platform to the design and fabrication of ten-layer Bayer color routers in the visible spectrum. Six device variants spanning Sb_2S_3 refractive indices of $n = 2.0$, 2.1, and 2.2 and two RGB design wavelength sets have been fabricated on a transparent doped-SiC substrate, with the substrate choice driven by the high electron-beam doses required for the precursor decomposition. To our knowledge, this is the highest number of Sb_2S_3 layers recorded for a a stack patterned with this direct-write approach to date, and it demonstrates that the platform can be extended to layer counts well beyond the three- and two-layer devices reported in Chapters 3 and 4.

Experimental characterization of the routing efficiency and spectral fidelity of the fabricated devices is in progress, and a direct comparison between the simulated and measured performance will be included in the publication accompanying this chapter [188]. This design can be improved by exploring alternative transparent conductive substrates to push the operating window further into the blue, and different types of application specific sorting can be explored (different combinations of wavelength, polarization, angular momentum etc.). Ultimately, integrating the Sb_2S_3 direct-write stack directly onto a back-illuminated CMOS image sensor die would close the loop from fabrication platform to functional device, and the low-temperature, spin-coat-based process flow introduced in Chapter 3 is in principle compatible with post-CMOS processing constraints.

Chapter 6

GEOMETRIC PHASE METASURFACES FOR OPTICAL VORTEX CORONOGRAPHS

The material in this chapter was also covered in Dr. Yiran Gu's thesis.

High-contrast imaging for exoplanet detection requires suppressing stellar light by factors exceeding 10^{10}, a challenge effectively addressed by optical vortex coronagraphs that redirect on-axis starlight. This work presents the design, fabrication, and characterization of geometric phase metasurfaces composed of TiO_2 and a-Si nanopillars, engineered to function as high-efficiency vortex phase masks or phase correctors. Broadband optimization of unit cell geometries was performed in simulations, with experimental validation confirming robustness against fabrication imperfections. The fabricated annular-ring masks exhibit uniform retardance and high transmission. These results establish metasurfaces as a compact and scalable platform for next-generation high-contrast imaging systems, while highlighting the need for future exploration into multilayer or inverse-designed structures to extend broadband performance.

6.1 Introduction

The detection of Earth-like exoplanets in the habitable zone of their stars and their spectroscopic characterization in a search for biosignatures requires planet-to-star brightness ratios of the order of 10^{-10} at visible wavelengths[198]. The stringent planet-to-star brightness ratio can be achieved by suppressing stellar photons using an internal occulter (e.g., coronagraph) within the telescope assembly [199, 200]. Therefore, high-contrast imaging coronagraphs are a key technology enabler in the search for biosignatures on an Earth-like exoplanet from a future space telescope [201, 202, 203].

Optical vortex coronographs (OVCs) have been identified as a highly effective tool for achieving a high planet-to-star brightness contrast [204, 205]. When an OVC is positioned at the focal plane of a telescope, as in Figure 6.1, the spatially varying phase induces a redistribution of incident starlight, diffracting the light originating from an on-axis star away from the telescope's reimaged pupil plane and allowing the transmission of light from a weaker, off-axis planet with minimal perturbation.

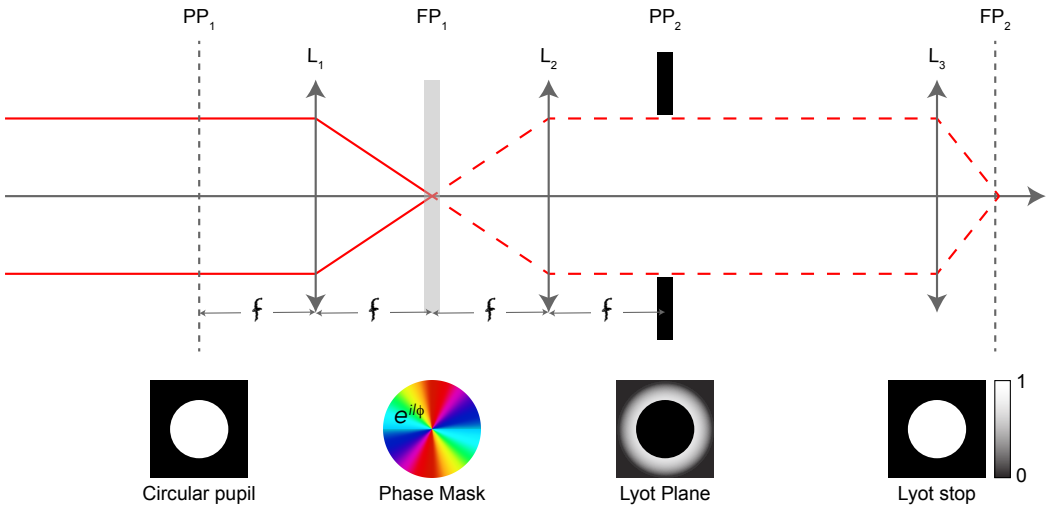


Figure 6.1: **Operating principle of a vector vortex coronagraph.** A vector vortex coronagraph concept with a vectorial phase mask. The coronagraph is placed at the first focal plane (FP1), and a Lyot stop is placed at the second pupil plane (PP2).

In this context, the coronagraph functions as a vectorial phase device, introducing a phase shift that varies between orthogonal polarization components of the incoming radiation.

Many efforts have been made to achieve the helical phase profile for OVCs [206, 207, 208, 12], including computer-generated holograms [209, 210], programmable liquid crystals [211, 212], and refractive spiral phase elements [213]. However, these methods are either optomechanically cumbersome, have low efficiency, or are difficult to manufacture uniformly. Phase profile control requires precision better than λ/n, where λ is the wavelength of the impinging light and n is the refractive index of the glass. In the most demanding applications, such as Earth-like planet detection, one would have to control the phase-ramping profile at the nanometer level. Here, we demonstrate the feasibility of using flat optical metasurfaces for these applications.

Metasurfaces consist of arrays of nanoscale elements, known as meta-atoms, and are artificially structured ultrathin surfaces designed to manipulate light at subwavelength scales [214, 6]. Among them, all-dielectric geometric phase (or Pancharatnam-Berry phase) metasurfaces (GP-MS) present advantages of low loss and high efficiency in manipulating polarization states of light [215, 13]. In this work, we numerically optimized for individual meta-atoms and utilized GP to construct both

an annular ring and a phase mask. Furthermore, in exoplanet research, visible-light coronagraphs are employed to directly image reflected light from planets or study circumstellar dust disks[216]. However, silicon, the most common material for GP-MS due to its large real part of refractive index, induces losses in this wavelength range. This work explored the design and fabrication of titanium dioxide (TiO_2) and amorphous silicon (a-Si) based GP-MS.

6.2 Design and Fabrication

Optimization of Meta-atoms

The Jones matrix for a geometric phase metasurface at a local position $\mathbf{r}$ and a single wavelength λ can be represented on the basis of circular polarization ($\hat{e}_R$ and $\hat{e}_L$) as[217]:

$$\mathbf{T}(\mathbf{r},\lambda) = (\frac{t_x + t_y e^{i\phi}}{2}) \begin{bmatrix} 1 & 0 \\ 0 & 1 \end{bmatrix} + (\frac{t_x - t_y e^{i\phi}}{2}) \begin{bmatrix} 0 & e^{i2\theta(\mathbf{r})} \\ e^{-i2\theta(\mathbf{r})} & 0 \end{bmatrix} \tag{6.1}$$

where t_x (t_y) is the amplitude of the complex transmission coefficient for the x(y) polarization, ϕ is the retardation between the two polarization ($\phi_y - \phi_x$), $\theta(\mathbf{r})$ is the rotation of local axis from x-axis, and $\pm i2\theta(\mathbf{r})$ is the local geometric phase. The term on the left represents the same handedness of the transmitted light or the co-polarized component, while the term on the right represents the cross-polarized component.

For a monochromatic unit cell, the absolute value of the coefficient for the cross-polarized component, $|\frac{t_x(\mathbf{r},\lambda) - t_y(\mathbf{r},\lambda)e^{i\phi}}{2}|$, should be maximized; while that for the co-polarized component, $|\frac{t_x(\mathbf{r},\lambda) + t_y(\mathbf{r},\lambda)e^{i\phi}}{2}|$, should be minimized. Thus, the optimal monochromatic metaatom should have ϕ of π and t_x (t_y) close to unity, which is essentially a half-wave plate (HWP). To design coronagraph phase masks with a 10% band, the following objective function is maximized:

$$f(\lambda_0) = \int_{0.95\lambda_0}^{1.05\lambda_0} |\frac{t_x(\lambda) - t_y(\lambda)e^{i\phi(\lambda)}}{2}|^2 - |\frac{t_x(\lambda) + t_y(\lambda)e^{i\phi(\lambda)}}{2}|^2 \, d\lambda \tag{6.2}$$

where λ_0 is the designated center wavelength.

Many materials have a small to negligible loss in visible wavelengths[218], and thus are suitable for coronagraph phase masks. In this work, we optimized unit cells using both amorphous silicon (a-Si) and titanium dioxide (TiO_2), as shown in Figure 6.2 (a, d and g). For a-Si structures, the center wavelength λ_0 is set at 750 nm, while for TiO_2, λ_0 = 600 nm. The corresponding broadband objective

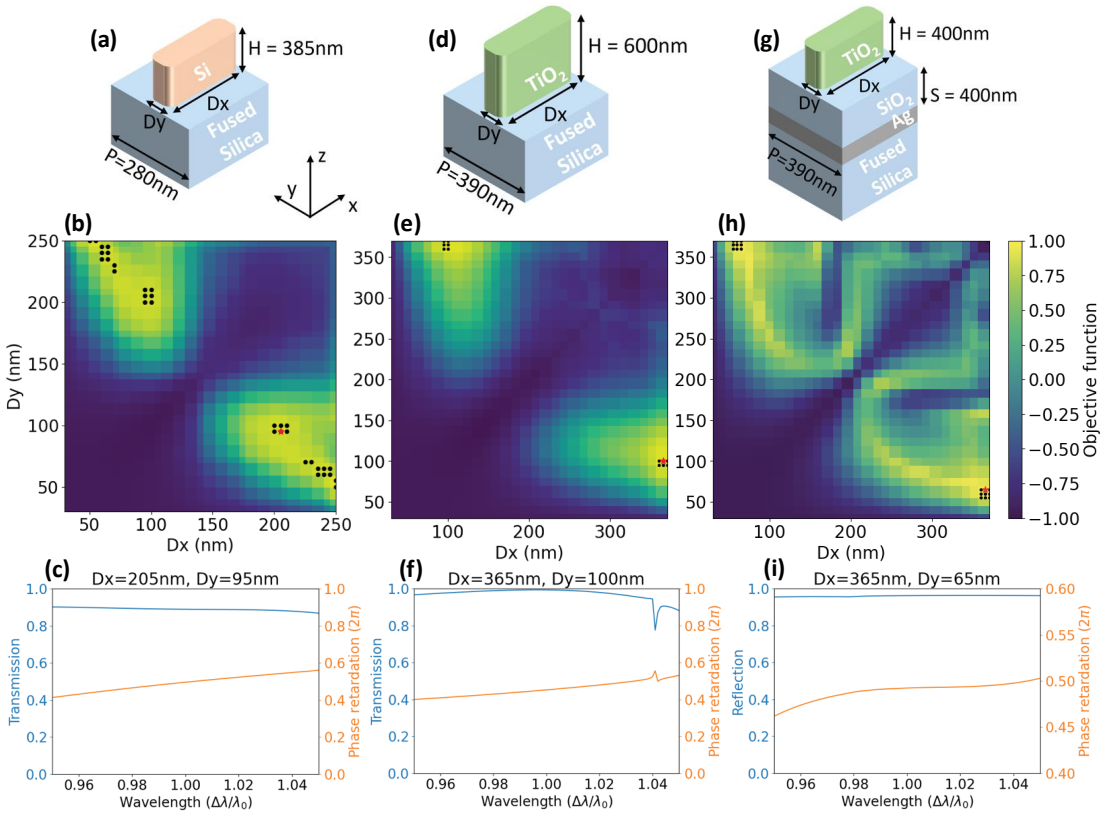


Figure 6.2: **Broadband unit cell optimization for geometric phase metasurface coronagraph masks.** Three types of unit cells are schematically depicted in (a), (d), and (g), where the first two are transmissive and the third is reflective. The broadband objective function results are shown in (b), (e), and (h). The parameter combinations yielding results higher than the corresponding thresholds are indicated with black dots (0.85 for structures in (a), 0.90 for structures in (d), and 0.95 for structures in (g)). The selected unit cells are indicated with red stars. (c), (f), and (i) show the transmission (reflection) and phase retardation across the bandwidth for the corresponding selected unit cell.

function results are shown in Figure 6.2 (b, e and h), with the selected parameters indicated by red stars. The transmission (reflection) and the phase retardation from $0.95\lambda_0$ to $1.05\lambda_0$ can be found in Figure 6.2 (c, f and i). Among the parameter combinations yielding the objective function above the corresponding threshold (indicated by black dots), the selected one has the lowest derivatives across D_x and D_y. This minimizes performance degradation due to fabrication errors. Simulations are performed with both FDTD (Lumerical) and S4, a Rigorous Coupled Wave Analysis (RCWA) solver[219]. The fused silica substrate has a refractive index of

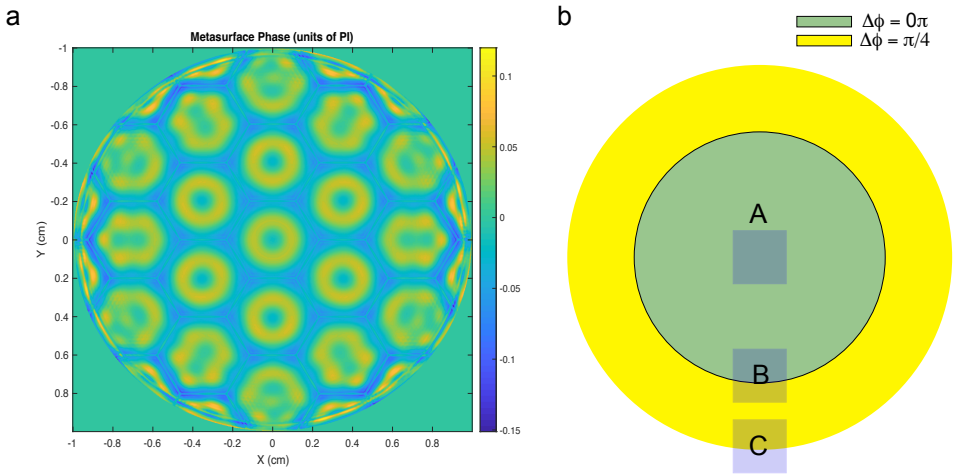


Figure 6.3: **Hexagonal aperture and annular ring phase mask designs.** Hexagonal aperture phase mask (a) and the annular ring phase mask (b).

1.45, a-Si has a refractive index varying from 3.7 to 3.8, and TiO_2 has 2.2 to 2.3 in the corresponding wavelength range.

Design of Geometrical Phase Masks

Two types of focal-plane phase correctors are optimized to correct phase aberrations in a coronagraph in a segmented aperture telescope, as shown in Figure 6.3. The annular ring, Figure 6.3.b, has two regions with different geometric phases, and the rotations of the unit cells are indicated in the figure. Another potential complication arises when using a segmented telescope arrangement. The gaps between mirror segments must be apodized to prevent unwanted diffraction in the image plane from amplitude discontinuities. A segmented aperture in the pupil plane, PP1, will result in diffracted starlight leaking into the dark hole, making exoplanet detection infeasible [220]. As a result, complex masks in the upstream pupil plane with a specific segmented aperture design can restore the 10^{-10} starlight suppression capability of the OVCs [221]; e.g., Figure 6.3.a shows a pupil mask designed for an apodized OVC with a notional ~0.9 m primary mirror comprising of hexagonal segments.

Fabrication

The deposition of a-Si on fused silica substrates is performed through plasma-enhanced chemical vapor deposition (PECVD). For a-Si patterning, an electron-beam resist, ZEP 520A, is used in electron-beam lithography (EBL) with a Raith

EBPG-5200. The pattern is transferred to a 30 nm alumina (Al_2O_3) hard mask through electron beam evaporation (CHA Industries Mark 40), followed by a lift-off process. With the aid of the hard mask, a-Si is etched using inductively coupled plasma reactive ion etching (ICP-RIE) (Oxford Instruments, Plasmalab System 100). The fabricated pattern is shown in Figure 6.4.a, b, where the target pillar parameters are 101 nm and 203 nm.

For TiO_2 transmissive masks, the patterns are written with a similar EBL process, which is followed by an ALD filling of TiO_2 (Figure 6.4.c). The uniform layer on the top of the resist is etched away with RIE, and the resist is then removed with NMP solvents. Similar processes can be found in the previous literature[13, 222, 223]. For reflective metasurfaces, high-reflective silver and 400 nm SiO_2 layers are deposited on the substrates prior to patterning. As shown in Figure 6.5, the ALD-grown TiO_2 presents a large real part of the refractive index in the visible range with a negligible imaginary part.

Multiple fabrication errors can lead to spatially dependent retardance errors, which result in non-optimal contrast ratios for the coronagraph and cannot be numerically corrected during operation. A major one is stitching errors among the main fields during EBL. Thus, the design parameters (D_x and D_y) are chosen by avoiding any lattice resonance, where the retardance changes slowly along the design parameters. Optical and SEM images of example fabricated phase masks are shown in Figure 6.4.

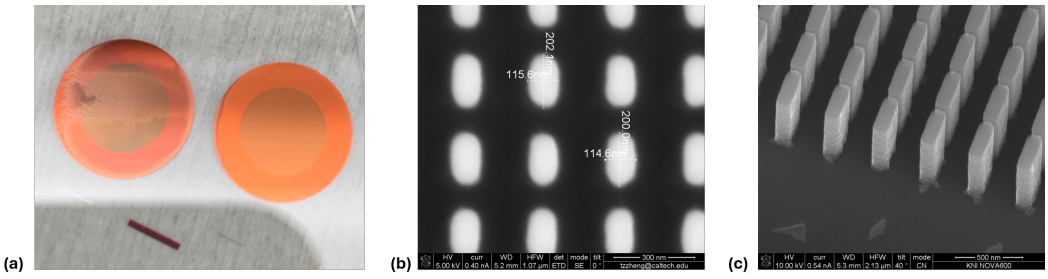


Figure 6.4: **Optical and SEM images of fabricated geometric phase metasurface masks.** (a) Optical image of the fabricated annular ring. (b) SEM image of the a-Si design with target parameters of 101 and 203 nm. (c) SEM image at a 40-degree tilt of the edge of a fabricated TiO_2 phase mask.

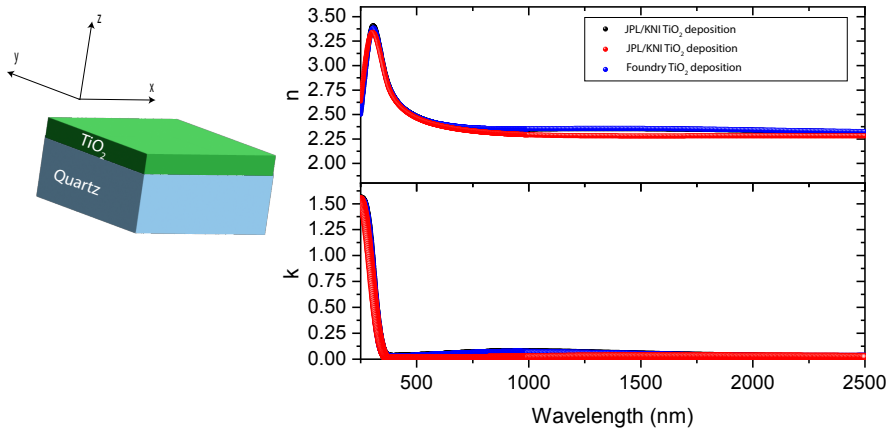


Figure 6.5: **Ellipsometry measurement of ALD-grown TiO_2 refractive index.** The measurement is performed on a uniform layer on a glass substrate, as shown in the schematic on the left. The refractive index's real part (n) and imaginary part (k) are shown on the right.

6.3 Experimental Results

Mueller matrix polarimetry characterizes the optical properties of a sample such as birefringence or dichroism, describing how it transforms the incident Stokes vector using a 4×4 Mueller matrix [224]. A Mueller matrix imaging microscope, AxoScan, with a wavelength range of 400-1000 nm was used to characterize the fabricated metamasks. The AxoScan system provides detailed retardance maps across the surface of the phase mask, allowing the detection of uniformity issues and retardance variations. Retardance is a critical parameter that measures the phase shift introduced between the two polarization components of light as it propagates through the birefringent medium of the phase mask. The wavelength resolution for these measurements is ~ 5 nm, and the retardance measurement accuracy is on the order of ±0.01 nm or ±0.1°.

For a fabricated a-Si annular ring, the transmission results, as shown in the top row of Figure 6.6, indicate an average transmission of better than 84% with an average 91% transmission for bare fused silica substrates. The retardance images, as shown in the middle row of Figure 6.6, show (179.4±0.4)° retardance value throughout the measurement window. The visible square patterns represent the remaining stitching errors during e-Beam lithography. The third row captures the retardance orientation (i.e. the meta-atom orientation), indicating the angular distribution of the phase shifts across the mask, as the geometric phase is twice the HWP orientation angle.

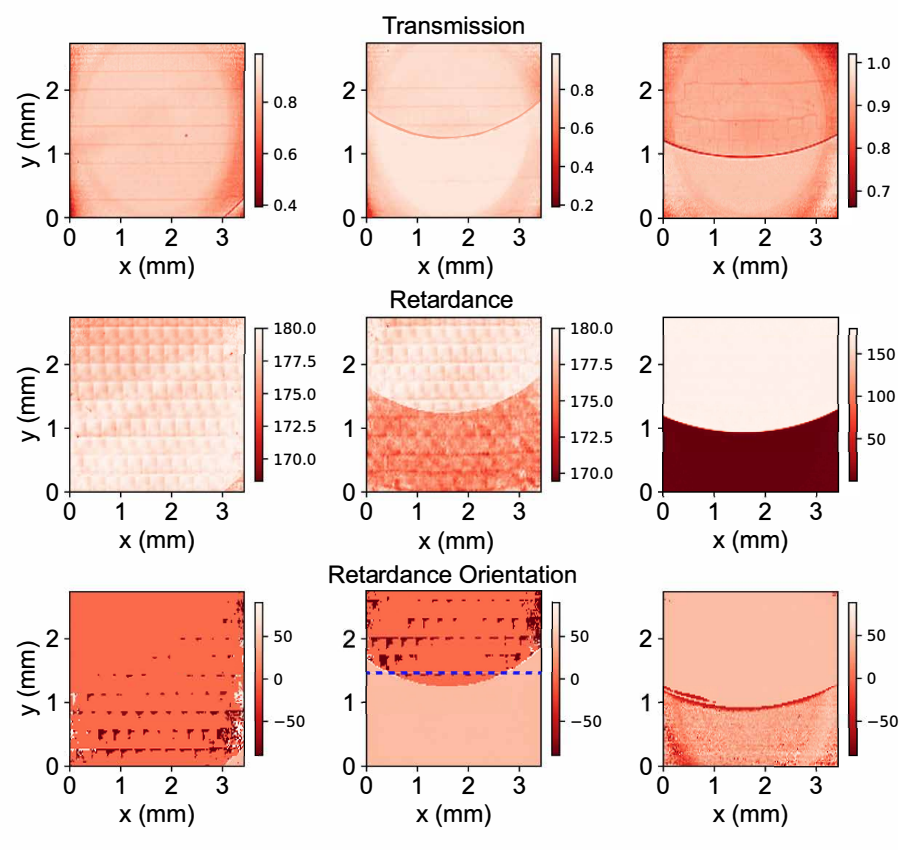


Figure 6.6: **Mueller matrix polarimetry characterization of the fabricated annular ring mask.** The measured transmission (top row), retardance (middle row), and retardance orientation (bottom row) for a fabricated annular ring across a 3.5 mm × 2.5 mm area. The left, middle, and right columns are measured in regions A, B, and C in Figure 6.3.b, respectively.

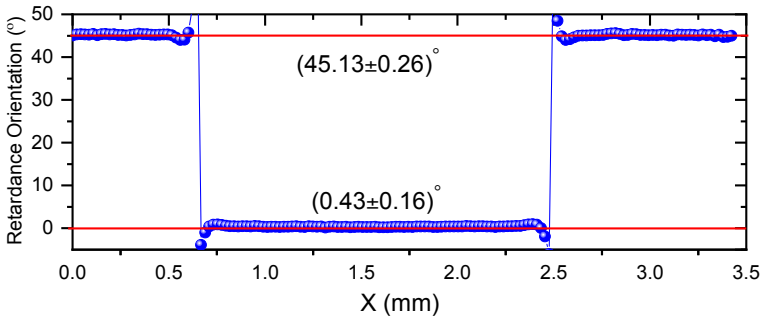


Figure 6.7: **Measured HWP retardance orientation across the annular ring boundary.** The measured HWP orientation for the annular ring along the dotted blue line in Figure 6.6.

The scans from the center of the pattern (region A in Figure 6.3.b) show a uniform orientation angle throughout the scan, and the scans from region B in Figure 6.3.b show a 45° discontinuity along the boundary between the two regions, as shown in Figure 6.7. The Mueller matrix measurements demonstrate consistent and uniform transmission and retardance across a 1 cm diameter phase mask.

Both Figure 6.8 and Figure 6.9 reveal the wavelength-dependent behaviors for the retardance using pillar-like a-Si or TiO_2 unit cells. In Figure 6.8a, the retardance values correspond to the average retardance measured in a 3.5 mm x 2.5 mm area, and each error bar is associated with the standard deviation of the measurements in the same window. The decrease in retardance for wavelengths longer than 760 *nm* can be attributed to the inherent phase wrapping in the Mueller matrix instrument. Figure 6.8.b shows the simulated retardance. The simulation results follow a similar trend, also peaking around 760 nm. The comparison between the experimental and simulated results validates the design and fabrication of the HWPs. Similarly, the measured retardance at λ = 580 nm, in Figure 6.9, validates the uniformity of TiO_2 mask fabrication.

To show the efficiency of this type of geometric phase metasurfaces, we calculated the contrast performance for charge-2 vortex phase masks that are constructed from optimized unit cells, as shown in Figure 6.10. The calculations consider a point

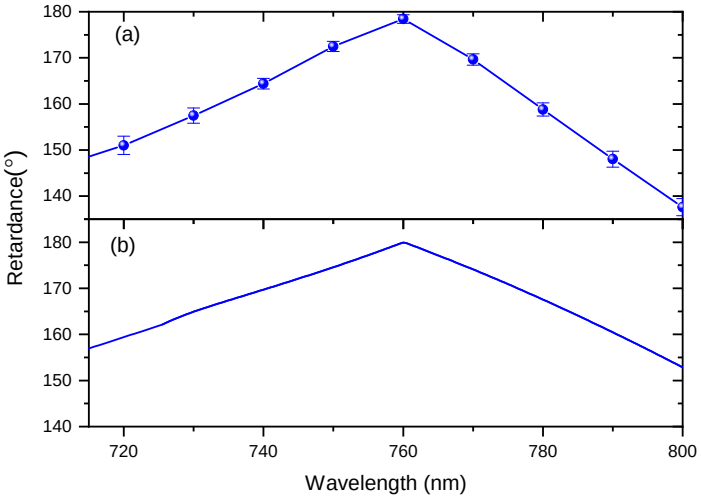


Figure 6.8: **Wavelength-dependent retardance of a-Si half-wave plates.** (a) The measured retardance with the spectral range from 700 to 800 nm and (b) the simulated retardance for a-Si HWPs as a function of wavelength.

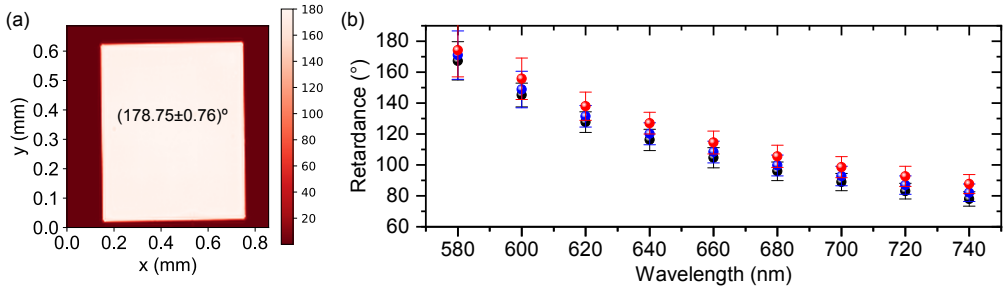


Figure 6.9: **Retardance uniformity and wavelength dependence of TiO_2 half-wave plates.** (a) The retardance measured at λ= 580 nm and (b) its wavelength dependence.

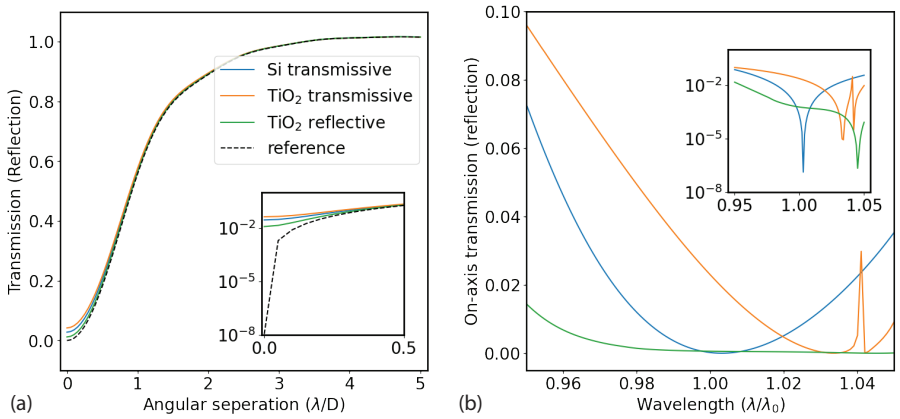


Figure 6.10: **Simulated coronagraph contrast performance of broadband vortex phase masks.** (a) Broadband transmission (reflection) using a vortex mask by the three optimized unit cells. The inset shows the same contrast plotted on a log scale. The black dashed line indicates the contrast using a monochromatic vortex mask as a reference. (b) The on-axis transmission for the three vortex masks over the bandwidth.

source, a circular aperture at PP1, a vortex phase mask at FP1, and a Lyot stop with a diameter equal to 0.8 of the aperture diameter[225]. Fabrication errors alter retardance responses locally and thus corrupt the contrast performance, as shown in Figure 6.11. However, according to previously shown measurements, the contrast corruption will be less than the orange-color curve.

6.4 Conclusion

The development of coronagraph phase masks using metasurface technology represents a significant advancement in optical instrumentation, particularly for applica-

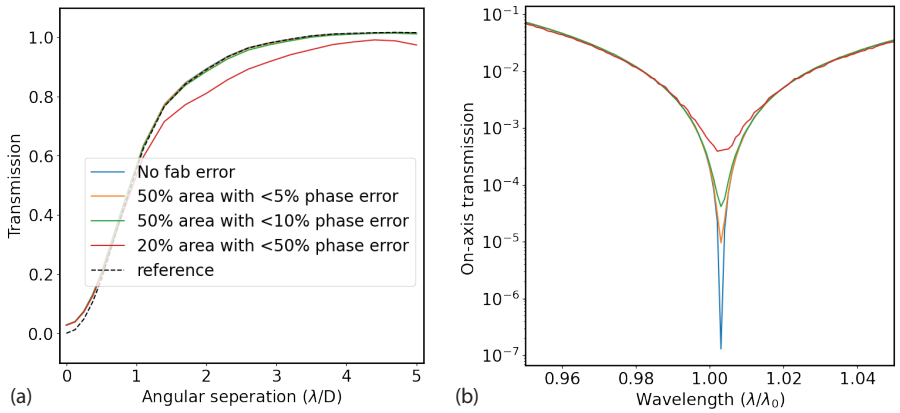


Figure 6.11: **Effect of fabrication phase errors on coronagraph contrast performance.** Calculated transmission for the vortex phase mask coronagraph with potential fabrication errors in phase.

tions in astronomy and exoplanet detection. Metasurfaces offer unparalleled control over phase, amplitude, and polarization at subwavelength scales, allowing for the creation of highly efficient, uniform, and compact phase masks. This technology provides a versatile platform to overcome the limitations of traditional diffractive optics, such as uniformity and bulkiness. By enabling precise wavefront shaping in coronagraphs, metasurface-based phase masks enhance the detection capabilities of high-contrast imaging systems by improving light suppression.

In this paper, we have demonstrated the design, fabrication, and testing processes involved in creating these metasurface phase masks. The results show that metasurfaces can achieve the necessary performance metrics to impart the necessary phase shifts. The uniformity for transmission, retardance, and orientation has been validated for fabrication methods of a-Si and TiO_2. However, even for an optimized design, wavelength-dependent retardance behaviors will hinder a truly broadband coronagraph. Instead of pillar-like unit cells, broadband performance can benefit from free-form inverse design[226] and 3D / multilayer metasurfaces[227, 228, 32]. Future work will also focus on optimizing the scalability of this technology and improving uniformity across large masks, enhancing its integration with existing optical systems. The versatility and precision of metasurface technology position it as a key enabler in the continued evolution of chronograph designs.

Chapter 7

STABLE YVO_4 QUANTUM TRANSDUCTION CAVITY WITH METAMIRRORS

7.1 Introduction

Optical cavities are among the most fundamental and enabling elements in photonics and quantum optics. By trapping light between two highly reflective mirrors, a cavity dramatically amplifies the interaction between photons and matter, underpinning technologies from lasers and optical frequency combs [229] to quantum electrodynamics [230] and gravitational wave detection [231]. For many of these applications, confining light to small mode volumes while maintaining high quality factors (high finesse) is essential. Achieving stable, low-loss light confinement requires careful engineering of the spatial mode structure inside the resonator.

Traditional open optical cavities achieve transverse mode stability by using at least one curved (concave) mirror. The curvature continuously refocuses the diverging Gaussian beam back toward the optical axis, allowing the field to sustain coherent round trips. The stability condition for a two-mirror resonator with mirror radii of curvature R_1 and R_2 separated by a distance L is given by the dimensionless g-parameters:

$$g_1 = 1 - \frac{L}{R_1}, \quad g_2 = 1 - \frac{L}{R_2}, \quad \text{stability condition: } 0 \leq g_1 g_2 \leq 1. \tag{7.1}$$

A plano-concave cavity consisting of one flat mirror and one curved mirror satisfies this condition when $L \leq R_2$ and represents a particularly useful geometry for integrating samples or emitters near the flat mirror, where the Gaussian beam waist is located. However, fabricating curved mirrors with small radii of curvature for compact, micron-scale cavities presents significant technical challenges. Conventional concave mirror fabrication through polishing or CO_2 laser ablation is limited in precision and scalability, and the resulting mirrors are difficult to integrate monolithically with on-chip photonic platforms.

Dielectric metasurfaces, arrays of subwavelength-scale resonators that impart spatially varying amplitude, phase, and polarization responses to reflected or transmitted light, have emerged as a compelling alternative for implementing optical functionality in an ultrathin, planar form factor [232]. By engineering the geom-

etry, orientation, and position of individual meta-atoms, metasurfaces can encode an arbitrary phase profile across their aperture. A metasurface designed to impart a quadratic (parabolic) spatial phase profile can therefore replace a physically curved mirror in a Fabry-Pérot cavity, enabling stable Gaussian mode resonances in an otherwise planar resonator.

The promise of metasurface-stabilized cavities has stimulated growing interest [233, 234, 232]. An early demonstration at microwave frequencies was provided by Fu et al. [234], who showed that a planar metasurface mimicking the focusing behavior of a concave mirror could be used to construct a stable, high-Q open cavity. The metasurface replaced one of the flat end mirrors, simultaneously providing the beam-confining phase curvature while preserving a planar form factor, establishing the conceptual foundation for this class of device.

At optical wavelengths, the landmark demonstration by Ossiander et al. [232] brought this concept to telecom wavelengths using dielectric metasurfaces. An amorphous silicon metasurface was patterned onto a distributed Bragg reflector (DBR) and used as one end mirror of a Fabry-Pérot microcavity, with a second opposing DBR serving as the flat mirror. The metasurface was designed to impart the spatial phase profile of the desired Gaussian mode at its plane, thereby compensating the transverse spreading of the focused beam on each round trip. The design methodology was also generalized to holographic mode profiles, demonstrating that complex transverse intensity distributions could be stabilized within such a cavity. More recently, metasurface-controlled holographic microcavities at visible wavelengths have further extended this capability [235], enabling mode-selective cavity-enhanced sensing and nonlinear optics.

In parallel, the broader context for this work is the challenge of quantum transduction, the coherent conversion of quantum states between microwave-frequency superconducting qubits and optical photons suitable for long-distance transmission through fiber networks. The rare-earth ion platform, in particular erbium (Er^{3+}) and ytterbium (Yb^{3+}) doped into yttrium orthovanadate (YVO_4) crystals, has emerged as a promising medium for microwave-to-optical (M2O) transduction [236, 237]. These ions simultaneously possess optical transitions at telecommunication wavelengths (~980 nm for Yb^{3+}, ~1530 nm for Er^{3+}) and spin transitions at microwave frequencies addressable by superconducting circuits, enabling coherent three-wave mixing between microwave, spin, and optical degrees of freedom.

The transduction efficiency in rare-earth ion systems scales with both the optical

pump power and the cavity quality factor for the transduced optical photons. Previous demonstrations of M2O transduction based on YVO_4 were limited in efficiency partly by the absence of an optical cavity enclosing the crystal, which would provide resonant enhancement of the optical interaction [237]. Integrating the YVO_4 crystal into a stable optical cavity with sufficiently high finesse is therefore a critical step toward achieving efficient, low-noise quantum transduction.

This chapter describes the design, simulation, and experimental characterization of a metasurface mirror (metamirror) intended to stabilize a Fabry-Pérot cavity enclosing a YVO_4 crystal. The cavity geometry is a plano-concave configuration: a flat, high-reflectivity distributed Bragg reflector (DBR) at the bottom serves as one mirror, while a second DBR combined with a metasurface layer encoding a quadratic reflection phase profile serves as the top (curved) mirror as shown in Figure 7.1. The metamirror phase profile is designed so that the cavity supports a stable Gaussian mode whose waist is located at the flat DBR and whose wavefront radius of curvature at the metasurface plane matches the designed radius of curvature R of the quadratic phase.

7.2 Cavity Design and Stability Analysis

Gaussian Beam Propagation and the Plano-Concave Configuration

The optical cavity in this work is designed to support the fundamental TEM_{00} Gaussian mode. In a plano-concave cavity, the flat mirror plays the role of the beam waist plane: the Gaussian beam has its minimum width there and a locally planar wavefront, so it reflects perfectly back from a flat mirror. The curved (or here, phase-equivalent curved) mirror is located at a distance L from the flat mirror (the cavity length) and must match the wavefront curvature of the propagated Gaussian beam at that plane.

For a Gaussian beam propagating in a medium of refractive index n at vacuum wavelength λ_0, the complex beam parameter $q(z)$ encodes both the beam radius $w(z)$ and the wavefront radius of curvature $R(z)$:

$$\frac{1}{q(z)} = \frac{1}{R(z)} - \frac{i\lambda_0}{\pi n\, w(z)^2}. \tag{7.2}$$

At the flat mirror located at $z = 0$ (the waist), the wavefront is planar ($R(0) \to \infty$) and the beam radius equals the waist w_0, so:

$$q(0) = iz_R, \qquad \text{where} \quad z_R = \frac{\pi n w_0^2}{\lambda_0} \tag{7.3}$$

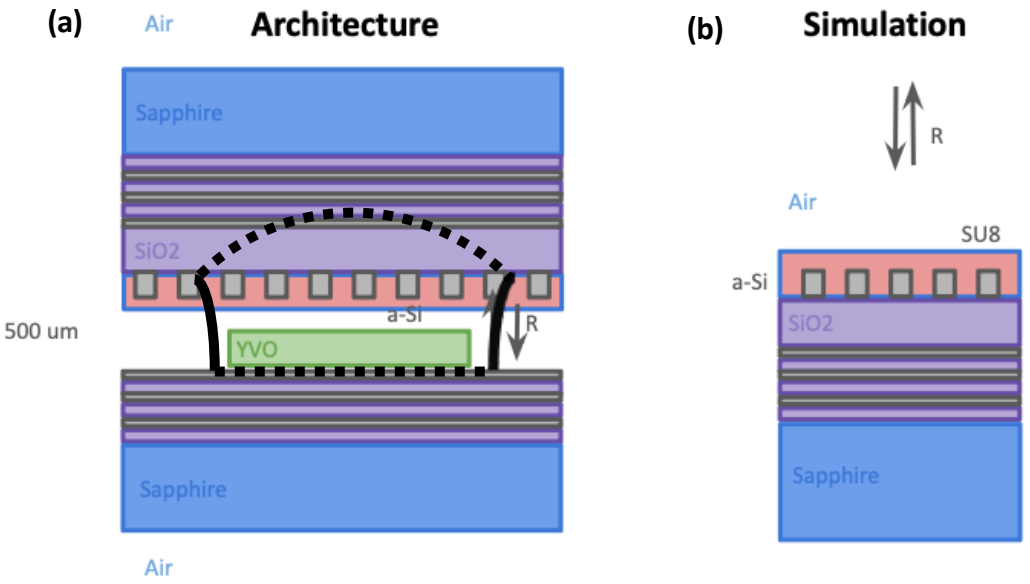


Figure 7.1: **Plano-concave cavity architecture with a DBR metamirror for YVO_4 quantum transduction.** (a) The cavity architecture with a DBR mirror at the bottom and a DBR + metasurface pair at the top. DBRs are varying layers of a-Si and SiO_2 thin films, and the metasurface is patterned into a-Si with a protective SU8 layer. The black line graphic in the middle represents the stable Gaussian mode in the cavity with its waist at the bottom mirror. (b) Metasurface architecture used in RCWA simulations, consisting of a sapphire substrate, DBR made of alternating Si and SiO_2 layers, the a-Si metasurface layer, and a 20 µm thick SU8 capping layer.

is the Rayleigh range. After propagating a distance L to the metasurface mirror, the complex beam parameter becomes:

$$q(L) = q(0) + L = iz_R + L. \tag{7.4}$$

The radius of curvature at the metasurface plane is extracted from the real part of $1/q(L)$:

$$\Re\left[\frac{1}{q(L)}\right] = \Re\left[\frac{1}{L + iz_R}\right] = \frac{L}{L^2 + z_R^2} = \frac{1}{R(L)}, \tag{7.5}$$

yielding:

$$R(L) = \frac{z_R^2 + L^2}{L}. \tag{7.6}$$

For the cavity to be stable, the metasurface at $z = L$ must impart a reflection phase profile that exactly matches the incoming wavefront curvature. That is, the designed

radius of curvature R_2 of the metamirror phase profile must equal $R(L)$:

$$R_2 = R(L) = \frac{z_R^2 + L^2}{L}. \tag{7.7}$$

Substituting $z_R = \pi n w_0^2/\lambda_0$ and rearranging, the stability condition links the beam waist w_0, the cavity length L, and the metamirror radius of curvature R_2:

$$\boxed{w_0^2 = \frac{\lambda_0}{\pi n}\sqrt{L(R_2 - L)},} \tag{7.8}$$

which is real and positive only when $0 \leq L \leq R_2$, the familiar stability condition for a plano-concave resonator, here recast in terms of the metasurface phase radius of curvature for the particular TEM_{00} Gaussian mode. Equation (7.8) simultaneously determines the beam waist that will form a self-consistent Gaussian mode in the cavity for given L and R_2.

Design Parameters

The physical constraints of this experiment are set by the available optomechanical cage assembly and mode-matching optics. The cavity length is fixed at $L = 500\ \mu$m, determined by the separation between the bottom DBR substrate and the top DBR/metasurface assembly within the cage. A target beam waist of $w_0 = 12.14\ \mu$m is chosen based on available mode-matching optics and the requirement for a beam waist large enough to overlap efficiently with the YVO_4 crystal.

Substituting these values into Eq. (7.8) determines the required metamirror radius of curvature:

$$R_2 = L + \left(\frac{\pi n w_0^2}{\lambda_0}\right)^2 \frac{1}{L} \approx 2200\ \mu\text{m}. \tag{7.9}$$

The beam radius at the metasurface plane follows from Gaussian propagation:

$$w_{\mathrm{MS}} = w_0\sqrt{1 + \left(\frac{L}{z_R}\right)^2} \approx 13.81\ \mu\text{m}. \tag{7.10}$$

The metasurface aperture must be large enough to intercept the incident Gaussian mode without significant clipping losses. Taking the aperture radius as 2.5 times the beam radius at the metasurface gives:

$$r_{\mathrm{MS}} = 2.5 \times w_{\mathrm{MS}} \approx 34.5\ \mu\text{m}. \tag{7.11}$$

The principal design parameters are summarized in Table 7.1.

Table 7.1: Principal cavity and beam parameters.

Parameter	Symbol	Value
Cavity length	L	500 μm
Beam waist (at flat DBR)	w_0	12.14 μm
Metamirror radius of curvature	R_2	2200 μm
Beam radius at metasurface	w_{MS}	13.81 μm
Metasurface aperture radius	r_{MS}	34.5 μm

These parameters place the cavity well within the stable regime ($L < R_2$) and fits the new stability condition arrived, approaching the hemispherical limit ($g_1 g_2 \rightarrow 0$). In practice this means the cavity is relatively insensitive to tilt misalignment of the mirrors, which is an important practical advantage given the planar assembly geometry.

7.3 Metamirror Design

The metamirror consists of a subwavelength array of amorphous silicon (a-Si) circular (for polarization insensitivity) pillars fabricated on top of a silicon dioxide (SiO_2) spacer layer, which rests on the top DBR substrate. The DBR provides broadband high reflectivity ($\sim$ 99.5%) near the operating wavelength (984.5 nm), while the pillar array modulates the reflection phase as a function of local pillar diameter. The target reflection phase profile across the metasurface aperture is the quadratic profile:

$$\Phi_{\mathrm{mirror}}(\rho) = -\frac{k\rho^2}{R_2}, \tag{7.12}$$

where $\rho = \sqrt{x^2 + y^2}$ is the radial distance from the optical axis and $k = 2\pi n/\lambda_0$ is the wavenumber. This phase profile imparts the same wavefront transformation as reflection from a concave spherical mirror of radius R_2, converting the diverging Gaussian wavefront of the incoming beam into a converging wavefront that reconstructs the waist at the flat DBR after one round trip.

The lattice constant of the pillar array is 300 nm and the pillar height is $h = 350$ nm. These parameters (small lattice period and short pillars) are deliberately chosen to support a large enough phase coverage in reflection while maintaining high reflectance across the accessible pillar diameter range as can be seen in Figure 7.2.a. 2π phase coverage is not needed in this application as the quadratic phase response needed is very shallow as can be understood through the design parameters given in Table 7.1, the metamirror radius of curvature and the beam radius at metasurface. Having a larger phase coverage results with spatially varying post diameters

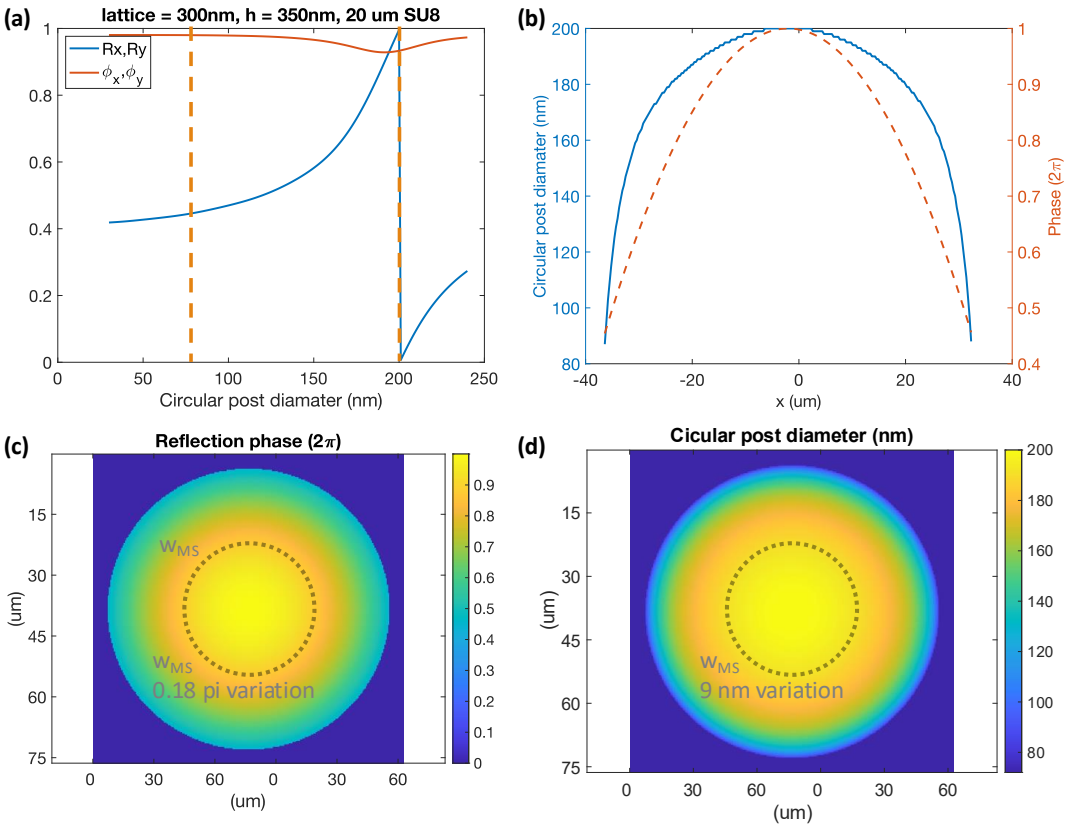


Figure 7.2: **Metamirror phase library and spatially varying pillar diameter profile.** (a) Reflection and reflected phase of the pillar-based metasurface with lattice period 300 nm, height 350 nm, and a 20 µm SU8 capping layer. (b) Circular post diameter (blue) and phase (2π, red) within the full metasurface aperture of 34.5 µm. (c) Spatially varying reflected phase (2π) within the full metasurface aperture; the dashed circle corresponds to the actual beam spot size hitting the metasurface. (d) Spatially varying post diameter (nm); the dashed circle corresponds to the actual beam spot size hitting the metasurface.

to be very similar to each other, which may not be resolved as accurately during fabrication. Within the beam spot at the metasurface, only 0.18π phase variation is needed (Figure 7.2.b-c). Since the metasurface is chosen to be 2.5 times larger than the actual beam spot size at the metasurface, the overall phase variation needed within the full metasurface aperture is $\sim 1.08\pi$ (Figure 7.2.b-c), which is achieved by varying the post diameter by 9 nm within the beam spot size at the metasurface, and by 116 nm within the full metasurface aperture (Figure 7.2.b-d). The reflection properties of the individual meta-atoms, circular a-Si pillars on the SiO_2/DBR substrate, are simulated using the Rigorous Coupled-Wave Analysis (RCWA) method

with periodic boundary conditions in the in-plane directions, enforcing the local periodicity approximation standard in phase-gradient metasurface design. In these simulations, in addition to the design parameters mentioned, the SU8 thickness is taken as 20 μm and the DBR consists of 70 nm a-Si and 164 nm SiO_2 layers, where each layer introduces a quarter wave phase delay for a constructive interference in reflection. The simulation sweeps the pillar diameter from approximately 80 nm to 250 nm at the design wavelength, yielding a library of complex reflection coefficients as a function of diameter. The pillar diameter is varied continuously across the aperture according to this look-up table, as shown in Figure 7.2.a, mapping diameter to reflection phase, so that each spatial location of the array realizes the local phase value $\Phi_{\text{mirror}}(\rho)$ required by the design.

7.4 Cavity Characterization and Finesse Measurements

Cavity finesse is defined as the ratio of the free spectral range (FSR) to the full-width-at-half-maximum (FWHM) linewidth of the resonance peaks:

$$\mathcal{F} = \frac{\Delta\nu_{\text{FSR}}}{\Delta\nu_{\text{FWHM}}} \tag{7.13}$$

Finesse measurements are performed by sweeping the laser wavelength across at least one free spectral range and recording the cavity transmission as a function of wavelength.

The laser source is a continuously tunable external-cavity diode laser (CTL) capable of mode-hop-free tuning over a range exceeding 150 GHz, sufficient to cover one FSR of the 500 μm cavity. At the operating wavelength of ~984.5 nm, the FSR corresponds to approximately 0.4–0.5 nm in wavelength, and a scan range of 0.5 nm is used. The wavelength is swept using the CTL motor control at a scan frequency of 0.2 Hz, chosen to avoid the waveform distortion that arises when the sweep is too fast relative to the detector sampling rate while still covering at least one full triangular scan cycle within the oscilloscope acquisition window.

Cavity transmission as a function of wavelength is recorded on a digital oscilloscope in single-acquisition mode with a time base of 4 ms/pt and 2500 record points per acquisition (oscilloscope timebase: 1.0 s/div), ensuring capture of at least one complete scan cycle. The finesse is extracted from the ratio of the FSR peak spacing to the resonance FWHM measured in the acquired waveform.

Before assembling the full cavity, the reflectivities of the individual mirror components are characterized at 2.2 mW input power from the same CTL source. Top DBR

is deliberately chosen as a lower reflection mirror with measured $R \approx 75$–80% for experimental practicality. The reflection for the high-reflectivity DBR, $R \approx 99.5\%$ is measured.

To directly assess whether the metasurface improves the cavity finesse, the finesse is measured as a spatially resolved map across the mirror surface. The top mirror assembly (DBR + metasurface) is mounted on a precision piezo-nanopositioning stage. The measurement is performed on a 50×50 grid over a $20{,}000 \times 20{,}000$ step region of the stage, sampling 2500 positions per group in a 2×2 array of metasurface patterns spaced approximately 108,000 steps ($\approx$13.5 metasurface periods) apart. At each grid point, a full CTL wavelength sweep is acquired and the finesse extracted.

The spatial finesse map clearly resolves the metasurface pattern array, as can be seen in Figure 7.3. Outside the metasurface regions, the cavity finesse is approximately 10, consistent with a cavity in which the top mirror provides no spatial phase correction and the beam is not efficiently confined transversely. Within each metasurface region, the finesse rises to approximately 22.

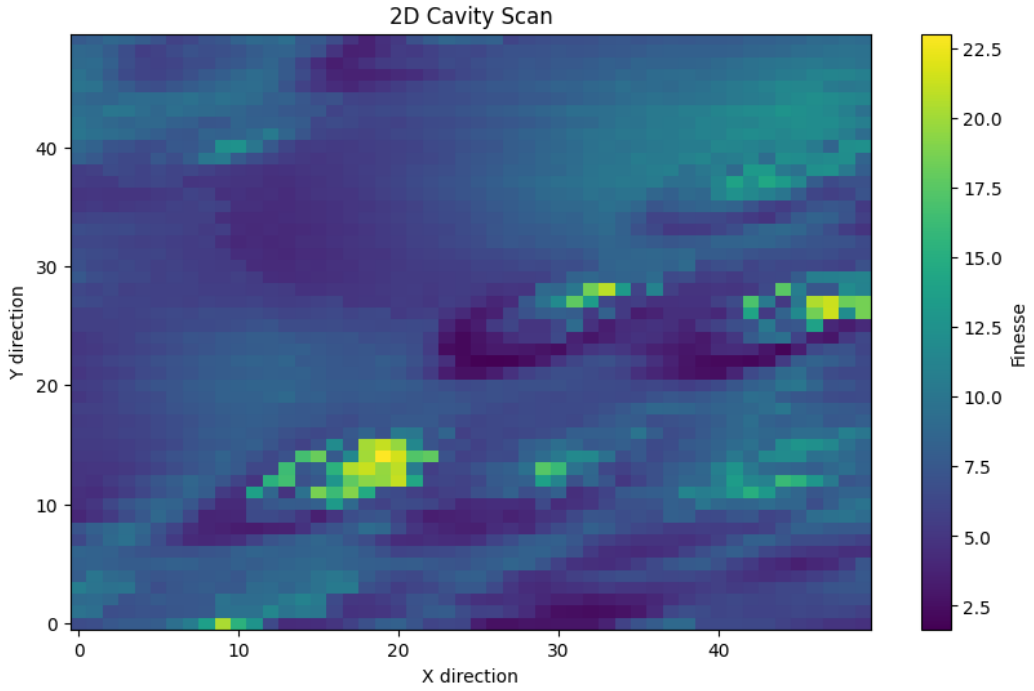


Figure 7.3: **Spatially resolved finesse map confirming metamirror-enhanced cavity performance.** Finesse measured as a function of position across the cavity mirror surface. The metasurface regions show an approximately two-fold enhancement in finesse relative to the surrounding area. Although there is some astigmatism in the imaging, the elliptical structures are part of the metasurface array.

For a cavity with one mirror at $R_1 = 99.5\%$ and one at $R_2 = 77.5\%$, the theoretical maximum finesse (in the absence of all other round-trip losses) is:

$$\mathcal{F}_{\max} = \frac{\pi(R_1 R_2)^{1/4}}{1 - \sqrt{R_1 R_2}} = 24.16, \tag{7.14}$$

which sets the performance ceiling for this mirror combination. Experimentally, we achieve a finesse of ~22 as can be seen in Figure 7.3, which is in the proximity of the upper theoretical limit. This approximately two-fold improvement in finesse directly demonstrates that the quadratic-phase metamirror successfully stabilizes the Gaussian mode in the cavity. The spatial correspondence between the high-finesse regions and the metasurface pattern array confirms that the enhancement is due to the designed phase profile, rather than any other local surface property.

7.5 Discussion

The measured finesse of ~22 on the metasurface regions is in good agreement with the theoretical maximum of 24.16 set by the mirror reflectivities, indicating that the additional round-trip loss introduced by the metasurface is small. The dominant loss in this cavity is therefore the intrinsic absorption and scattering of the top DBR, not the metasurface layer itself—consistent with the design criterion that the metasurface be operated in a high-reflectance, slowly varying region of the meta-atom phase library.

The improvement from a baseline finesse of ~10 (without metasurface) to ~22 (with metasurface) can be understood as follows. Without the metasurface phase correction, the focused Gaussian beam diffracts transversely within the cavity and acquires a diverging wavefront that does not match the flat DBR upon reflection. This leads to mode mismatch losses on each round trip, reducing the effective finesse well below the mirror-reflectivity limit. The metamirror corrects this mismatch by imparting the appropriate wavefront curvature on reflection, allowing the beam to reconstruct its waist at the flat DBR and sustain a coherent mode. With the mode properly stabilized, the finesse approaches the mirror-loss-limited value.

This approach is particularly well-suited for quantum transduction experiments with YVO_4 crystals, which have planar, polished surfaces compatible with planar mirror geometries. A conventional plano-concave cavity with a mechanically curved mirror would require the curved surface to be positioned very close to the crystal, creating practical difficulties in alignment and crystal exchange. By contrast, the metasurface mirror is fabricated on a flat substrate, allowing straightforward integration into the cage assembly while still providing the necessary mode-confining phase curvature.

Conclusion

This chapter has demonstrated that a planar dielectric metasurface can serve as an effective curved mirror for stabilizing an optical cavity enclosing a YVO_4 crystal intended for quantum transduction. By encoding a quadratic reflection phase profile into a subwavelength a-Si pillar array on a DBR substrate, we replaced the role of a conventional concave mirror with a flat metasurface that is straightforward to integrate into a compact cage assembly.

The cavity finesse was measured to increase approximately two-fold upon introduction of the metamirror, rising from a background value of ~10 to ~22 across the metasurface regions, approaching the limit set by the mirror reflectivities. This improvement directly reflects the metamirror's ability to confine a well-defined Gaussian mode inside the resonator, which is a prerequisite for efficient cavity-enhanced quantum transduction.

Looking forward, the finesse can be improved significantly by upgrading to higher-reflectivity mirror components, which would directly translate into stronger optical field enhancement and higher transduction efficiency. More broadly, the planar and scalable nature of the metasurface platform makes it well-suited for integration into future on-chip transducer architectures, where conventional curved optics would be impractical. This work therefore represents an important step toward building the high-quality optical resonators needed for efficient microwave-to-optical quantum transduction with rare-earth ion systems.

Chapter 8

CONCLUSION AND OUTLOOK

8.1 Summary

This thesis explored the design, fabrication, and characterization of active and multilayer metasurfaces across a range of photonic platforms and applications, with a unifying focus on engineering the optical response of subwavelength nanostructures to manipulate light, and demonstrated their potential across a range of photonic applications, from reconfigurable wavefront shaping to quantum optical cavities.

In Chapter 2, we proposed an on-substrate NEMS-tunable metasurface based on slot-mode resonances at telecom wavelengths. High-aspect-ratio doped silicon slabs bend electrostatically, shifting the slot-mode resonance and enabling an amplitude modulation of 80% and phase modulation of 1.4π within 10 V. Unlike prior suspended designs, the on-substrate geometry is mechanically robust and naturally breaks z-symmetry to achieve near-2π phase response without a back mirror. Beam steering reaching 58% efficiency was demonstrated numerically.

In Chapter 3, we established a high-throughput direct-write EBL platform using an antimony-BDCA precursor that decomposes in situ into Sb_2S_3, reducing the number of multilayer fabrication steps by eliminating processes suc as deposition, etching, and lift-off entirely. Three-layer q-BIC-derived filter devices with independently tunable resonance wavelengths and Q-factors were designed and experimentally demonstrated. Filter arrays with average absolute pairwise Pearson correlation coefficients of 0.11 and 0.21 for sets of 9 and 36 filters surpassed prior metasurface and photonic-crystal implementations for compressive spectral sensing.

In Chapter 4, the same Sb_2S_3 platform was applied to fiber-to-chip coupling. Two layers of gratings were patterned on top of an existing SOI waveguide with a taper, without any modification to the host circuit. All the widths of the individual etched and unetched elements of the vertical grating coupler optimized via adjoint-based inverse design with the Adam optimizer across 204 geometric parameters. The result is a simulated peak coupling efficiency of 89.5% (-0.48 dB) at 1550 nm, among the highest reported for any grating coupler design.

In Chapter 5, the Sb_2S_3 direct-write electron-beam lithography platform was ex-

tended to ten-layer volumetric Bayer color routers operating in the visible spectrum. Six device variants spanning refractive indices of $n = 2.0$, 2.1, and 2.2 and two RGB design wavelength sets centered on (475, 550, 650) nm and (550, 650, 750) nm were designed by adjoint-based inverse optimization and fabricated on a transparent doped-SiC substrate. This work constitutes, to our knowledge, the first free-form multilayer meta-optic Bayer color router in the visible spectrum, and demonstrates that the Sb_2S_3 direct-write platform can be scaled to layer counts well beyond those demonstrated in Chapters 3 and 4.

In Chapter 6, TiO_2 and a-Si geometric-phase metasurfaces were designed, fabricated, and tested as phase aberration correctors for optical vortex coronagraphs. Mueller-matrix polarimetry confirmed spatially uniform retardance of $(179.4 \pm 0.4)^\circ$ and average transmission above 84% across centimeter-scale apertures, establishing metasurfaces as a scalable platform for high-contrast astronomical imaging.

In Chapter 7, a planar a-Si metamirror encoding a quadratic reflection phase profile was used to stabilize a Fabry-Pérot cavity enclosing a $YVO_4{:}Yb^{3+}$ crystal for microwave-to-optical quantum transduction. Spatially resolved finesse measurements confirmed more than two-fold improvement, from ~10 to ~22, across the metasurface regions, approaching the mirror-reflectivity-limited theoretical maximum and demonstrating that a planar metasurface can fully replace a curved mirror in a compact cavity assembly.

8.2 Outlook

The works presented in this thesis reflect a broader effort to push metasurface technology from isolated demonstrations toward engineered systems with defined performance targets and practical fabrication constraints. Nevertheless, several challenges remain open both at the device level and in the field at large.

From a fabrication perspective, photonics continues to lag behind electronics in process maturity. Modern semiconductor foundries routinely pattern features below 5 nm and stack hundreds of interconnect layers in a single chip, yet these capabilities are optimized for electronic devices and are largely inaccessible to photonic nanostructures. Research cleanrooms, by contrast, lack the automation, process control, and design-rule infrastructure of a high-volume foundry. This gap manifests concretely in two places in this thesis. First, realizing the high-aspect-ratio silicon slabs required for the NEMS platform demands a reliable deep etch with vertical sidewalls and uniform slot widths, a process that proved difficult to achieve consistently in

a research setting. Second, the multilayer q-BIC filter platform required developing a direct-write fabrication approach precisely because no established multilayer process exists in research photonics. The antimony-based direct-write method introduced here is a practical step forward, but it carries its own constraints: film thickness is set by spin-coating conditions rather than by a controlled deposition tool, limiting the flexibility to independently dial in each layer's thickness. More generally, extending multilayer metasurface architectures to many layers demands platforms that maintain registration accuracy and material quality across repeated cycle, a challenge the Sb_2S_3 process begins to address but has not yet solved at scale. The broader adoption of metasurfaces in practical systems will ultimately require compatibility with high-throughput patterning methods such as deep-UV lithography or nanoimprint, and realizing that will call for an industry-level commitment to nanophotonics manufacturing.

From a design perspective, engineering design choices always come in trade-offs. The NEMS beam-steering device illustrates a good example: carefully selecting the optical mode that the active stimulus couples into can greatly amplify the device's tuning sensitivity. High-Q resonances offer greater sensitivity to small perturbations but narrow the operating bandwidth, tighten fabrication tolerances, and increase susceptibility to disorder and material loss. Navigating these trade-offs through intuition and parameter sweeps becomes increasingly difficult as device complexity grows. Inverse design and machine learning techniques offer a more systematic path, capable of exploring non-intuitive geometries and multi-layer parameter spaces that physics-guided design alone cannot efficiently reach [177]. More complex nanophotonic devices call for better optimization algorithms, more physics driven machine learning employment for nanophotonic design, as well as research and development in promising material platforms.

Despite these challenges, the field continues to advance rapidly, and metasurfaces are increasingly well-positioned to play a central role in next-generation photonic systems, from reconfigurable free-space optics and integrated photonic interfaces to high-contrast astronomical imaging and quantum optical platforms.

BIBLIOGRAPHY

[1] N. Yu and F. Capasso. "Flat Optics with Designer Metasurfaces". *Nature Materials* 13 (2014), pp. 139–150 (cit. on pp. 1, 3, 9).

[2] B. E. A. Saleh and M. C. Teich. *Fundamentals of Photonics*. 3rd ed. Wiley, 2019 (cit. on p. 1).

[3] D. Neshev and I. Aharonovich. "Optical Metasurfaces: New Generation Building Blocks for Multi-Functional Optics". *Light: Science & Applications* 7 (2018), p. 58 (cit. on pp. 1, 9).

[4] F. Ding, A. Pors, and S. I. Bozhevolnyi. "Gradient Metasurfaces: A Review of Fundamentals and Applications". *Reports on Progress in Physics* 81 (2018), p. 026401 (cit. on pp. 1, 9).

[5] C. L. Holloway, E. F. Kuester, J. A. Gordon, J. O'Hara, J. Booth, and D. R. Smith. "An Overview of the Theory and Applications of Metasurfaces: The Two-Dimensional Equivalents of Metamaterials". *IEEE Antennas and Propagation Magazine* 54.2 (2012), pp. 10–35 (cit. on p. 1).

[6] S. M. Kamali, E. Arbabi, A. Arbabi, and A. Faraon. "A review of dielectric optical metasurfaces for wavefront control". *Nanophotonics* 7.6 (2018), pp. 1041–1068 (cit. on pp. 1, 76).

[7] M. Khorasaninejad, A. Y. Zhu, C. Roques-Carmes, W. T. Chen, J. Oh, I. Mishra, R. C. Devlin, and F. Capasso. "Polarization-Insensitive Metalenses at Visible Wavelengths". *Nano Letters* 16 (2016), pp. 7229–7234 (cit. on pp. 1, 3, 9).

[8] L. Wang, S. Kruk, H. Tang, T. Li, I. Kravchenko, D. N. Neshev, and Y. S. Kivshar. "Grayscale Transparent Metasurface Holograms". *Optica* 3 (2016), pp. 1504–1505 (cit. on pp. 1, 3, 9).

[9] Y. Hu, X. Luo, Y. Chen, Q. Liu, X. Li, Y. Wang, N. Liu, and H. Duan. "3D-Integrated Metasurfaces for Full-Colour Holography". *Light: Science & Applications* 8 (2019), p. 86 (cit. on pp. 1, 3, 9).

[10] A. John-Herpin, A. Tittl, L. Kühner, F. Richter, S. H. Huang, G. Shvets, S.-H. Oh, and H. Altug. "Metasurface-Enhanced Infrared Spectroscopy: An Abundance of Materials and Functionalities". *Advanced Materials* 35 (2023), p. 2110163 (cit. on pp. 1, 3, 9).

[11] A. Arbabi, Y. Horie, M. Bagheri, and A. Faraon. "Dielectric metasurfaces for complete control of phase and polarization with subwavelength spatial resolution and high transmission". *Nature Nanotechnology* 10.11 (2015), pp. 937–943 (cit. on pp. 2, 3).

[12] Z. Bomzon, G. Biener, V. Kleiner, and E. Hasman. “Space-variant Pancharatnam–Berry phase optical elements with computer-generated subwavelength gratings”. *Optics Letters* 27.13 (2002), pp. 1141–1143 (cit. on pp. 2, 76).

[13] A. Arbabi, H. Yu, M. Bagheri, and A. Faraon. “Dielectric metasurfaces for complete control of phase and polarization with subwavelength spatial resolution and high transmission”. *Nature nanotechnology* 10.11 (2015), pp. 937–943 (cit. on pp. 2, 76, 80).

[14] K. Koshelev, S. Lepeshov, M. Liu, A. Bogdanov, and Y. Kivshar. “Asymmetric Metasurfaces with High-Q Resonances Governed by Bound States in the Continuum”. *Physical Review Letters* 121.19 (2018), p. 193903 (cit. on pp. 2, 3, 26).

[15] S. Joseph, S. Pandey, S. Sarkar, and J. Joseph. “Bound States in the Continuum in Resonant Nanostructures: An Overview of Engineered Materials for Tailored Applications”. *Nanophotonics* 10.17 (2021), pp. 4175–4207 (cit. on pp. 2, 3, 26).

[16] B. A. Munk. *Frequency Selective Surfaces: Theory and Design*. Wiley, 2000 (cit. on p. 2).

[17] P. Lalanne and P. Chavel. “Metalenses at visible wavelengths: past, present, perspectives”. *Laser & Photonics Reviews* 11.3 (2017), p. 1600295 (cit. on p. 2).

[18] X. Ni, N. K. Emani, A. V. Kildishev, A. Boltasseva, and V. M. Shalaev. “Broadband Light Bending with Plasmonic Nanoantennas”. *Science* 335.6067 (2012), p. 427 (cit. on p. 2).

[19] N. Yu, P. Genevet, M. A. Kats, F. Aieta, J.-P. Tetienne, F. Capasso, and Z. Gaburro. “Light Propagation with Phase Discontinuities: Generalized Laws of Reflection and Refraction”. *Science* 334.6054 (2011), pp. 333–337 (cit. on p. 2).

[20] F. Monticone, N. M. Estakhri, and A. Alù. “Full Control of Nanoscale Optical Transmission with a Composite Metascreen”. *Physical Review Letters* 110.20 (2013), p. 203903 (cit. on p. 3).

[21] S. Jahani and Z. Jacob. “All-dielectric metamaterials”. *Nature Nanotechnology* 11.1 (2016), pp. 23–36 (cit. on p. 3).

[22] R. C. Devlin, M. Khorasaninejad, W. T. Chen, J. Oh, and F. Capasso. “Broadband high-efficiency dielectric metasurfaces for the visible spectrum”. *Proceedings of the National Academy of Sciences* 113.38 (2016), pp. 10473–10478 (cit. on p. 3).

[23] S. Wang, P. C. Wu, V.-C. Su, Y.-C. Lai, M.-K. Chen, H. Y. Kuo, B. H. Chen, Y. H. Chen, T.-T. Huang, J.-H. Wang, R.-M. Lin, C.-H. Kuan, T. Li, Z. Wang, S. Zhu, and D. P. Tsai. “A Broadband Achromatic Metalens in the Visible”. *Nature Nanotechnology* 13 (2018), pp. 227–232 (cit. on pp. 3, 9).

[24] C. W. Hsu, B. Zhen, A. D. Stone, J. D. Joannopoulos, and M. Soljačić. "Bound states in the continuum". *Nature Reviews Materials* 1.9 (2016), p. 16048 (cit. on p. 3).

[25] A. Tittl, A. Leitis, M. Liu, F. Yesilkoy, D.-Y. Choi, D. N. Neshev, Y. S. Kivshar, and H. Altug. "Imaging-Based Molecular Barcoding with Pixelated Dielectric Metasurfaces". *Science* 360.6393 (2018), pp. 1105–1109 (cit. on pp. 3, 31).

[26] F. Yesilkoy, E. R. Arvelo, Y. Jahani, M. Liu, A. Tittl, V. Cevher, Y. Kivshar, and H. Altug. "Ultrasensitive Hyperspectral Imaging and Biodetection Enabled by Dielectric Metasurfaces". *Nature Photonics* 13.6 (2019), pp. 390–396 (cit. on pp. 3, 31).

[27] A. Leitis, A. Tittl, M. Liu, B. H. Lee, M. B. Gu, Y. S. Kivshar, and H. Altug. "Angle-Multiplexed All-Dielectric Metasurfaces for Broadband Molecular Fingerprint Retrieval". *Science Advances* 5.5 (2019), eaaw2871 (cit. on pp. 3, 31).

[28] O. A. M. Abdelraouf, Z. Wang, H. Liu, Z. Dong, Q. Wang, M. Ye, X. R. Wang, Q. J. Wang, and H. Liu. "Recent Advances in Tunable Metasurfaces: Materials, Design, and Applications". *ACS Nano* 16 (2022), pp. 13339–13369 (cit. on pp. 4, 5, 9).

[29] Z. Chang, R. Huang, P. Chen, and G. Li. "Shaping Light with Multilayer Metasurfaces: Design, Fabrication, and Applications". *Journal of Physics D: Applied Physics* 58.44 (2025), p. 443003 (cit. on pp. 4, 26, 66).

[30] O. Avayu, E. Almeida, Y. Prior, and T. Ellenbogen. "Composite Functional Metasurfaces for Multispectral Achromatic Optics". *Nature Communications* 8.1 (2017), p. 14992 (cit. on pp. 4, 25).

[31] Y. Zhou, I. I. Kravchenko, H. Wang, J. R. Nolen, G. Gu, and J. Valentine. "Multilayer Noninteracting Dielectric Metasurfaces for Multiwavelength Metaoptics". *Nano Letters* 18.12 (2018), pp. 7529–7537 (cit. on pp. 4, 25).

[32] V. R. Shrestha, A. C. Overvig, M. Lu, A. Stein, and N. Yu. "Broadband achromatic dielectric metalenses". *Light: Science & Applications* 7 (2018), p. 85 (cit. on pp. 4, 85).

[33] A. Arbabi, E. Arbabi, S. M. Kamali, Y. Horie, S. Han, and A. Faraon. "Miniature optical planar camera based on a wide-angle metasurface doublet corrected for monochromatic aberrations". *Nature Communications* 7 (2016), p. 13682 (cit. on p. 4).

[34] M. Faraji-Dana, E. Arbabi, A. Arbabi, S. M. Kamali, H. Kwon, and A. Faraon. "Compact folded metasurface spectrometer". *Nature Communications* 9 (2018), p. 4196 (cit. on p. 4).

[35] E. Arbabi, A. Arbabi, S. M. Kamali, Y. Horie, and A. Faraon. "Multiwavelength polarization-insensitive lenses based on dielectric metasurfaces with meta-molecules". *Optica* 3.6 (2016), pp. 628–633 (cit. on p. 4).

[36] M. Mansouree, H. Kwon, E. Arbabi, A. McClung, A. Faraon, and A. Arbabi. "Multifunctional 2.5D Metastructures Enabled by Adjoint Optimization". *Optica* 7.1 (2020), pp. 77–84 (cit. on pp. 4, 25, 66).

[37] A. M. Shaltout, V. M. Shalaev, and M. L. Brongersma. "Spatiotemporal Light Control with Active Metasurfaces". *Science* 364 (2019) (cit. on pp. 5, 10).

[38] G. K. Shirmanesh, R. Sokhoyan, P. C. Wu, and H. A. Atwater. "Electro-Optically Tunable Multifunctional Metasurfaces". *ACS Nano* 14 (2020), pp. 6912–6920 (cit. on pp. 5, 9).

[39] J. Park, B. G. Jeong, S. I. Kim, D. Lee, J. Kim, C. Shin, C. B. Lee, T. Otsuka, J. Kyoung, S. Kim, K.-Y. Yang, Y.-Y. Park, J. Lee, I. Hwang, J. Jang, S. H. Song, M. L. Brongersma, K. Ha, S.-W. Hwang, H. Choo, and B. L. Choi. "All-Solid-State Spatial Light Modulator with Independent Phase and Amplitude Control for Three-Dimensional LiDAR Applications". *Nature Nanotechnology* 16 (2021), pp. 69–76 (cit. on pp. 5, 9).

[40] B. Gholipour, J. Zhang, K. F. MacDonald, D. W. Hewak, and N. I. Zheludev. "An All-Optical, Non-Volatile, Bidirectional, Phase-Change Meta-Switch". *Advanced Materials* 25 (2013), pp. 3050–3054 (cit. on pp. 6, 9).

[41] H. Liu, W. Dong, H. Wang, L. Lu, Q. Ruan, Y. S. Tan, R. E. Simpson, and J. K. W. Yang. "Rewritable Color Nanoprints in Antimony Trisulfide Films". *Science Advances* 6 (2020) (cit. on pp. 6, 9).

[42] J. Sautter, I. Staude, M. Decker, E. Rusak, D. N. Neshev, I. Brener, and Y. S. Kivshar. "Active Tuning of All-Dielectric Metasurfaces". *ACS Nano* 9 (2015), pp. 4308–4315 (cit. on pp. 6, 9).

[43] A. Komar, R. Paniagua-Domínguez, A. Miroshnichenko, Y. F. Yu, Y. S. Kivshar, A. I. Kuznetsov, and D. Neshev. "Dynamic Beam Switching by Liquid Crystal Tunable Dielectric Metasurfaces". *ACS Photonics* 5 (2018), pp. 1742–1748 (cit. on pp. 6, 9).

[44] H. Kwon, T. Zheng, and A. Faraon. "Nano-Electromechanical Tuning of Dual-Mode Resonant Dielectric Metasurfaces for Dynamic Amplitude and Phase Modulation". *Nano Letters* 21 (2021), pp. 2817–2823 (cit. on pp. 6, 10, 12, 15, 19).

[45] H. Kwon and A. Faraon. "NEMS-Tunable Dielectric Chiral Metasurfaces". *ACS Photonics* 8 (2021), pp. 2980–2986 (cit. on pp. 6, 10, 12, 15).

[46] H. Kwon, T. Zheng, and A. Faraon. "Nano-Electromechanical Spatial Light Modulator Enabled by Asymmetric Resonant Dielectric Metasurfaces". *Nature Communications* 13 (2022), p. 5811 (cit. on pp. 6, 10, 12, 15).

[47] T. Zheng, H. Kwon, and A. Faraon. “Nanoelectromechanical Tuning of High-Q Slot Metasurfaces”. *Nano Letters* 23 (2023), pp. 5588–5594 (cit. on pp. 6, 10, 12, 15).

[48] T. Low, A. Chaves, J. D. Caldwell, A. Kumar, N. X. Fang, P. Avouris, T. F. Heinz, F. Guinea, L. Martin-Moreno, and F. Koppens. “Polaritons in layered two-dimensional materials”. *Nature Materials* 16 (2017), pp. 182–194 (cit. on p. 6).

[49] M. R. Shcherbakov, S. Liu, V. V. Zubyuk, A. Vaskin, P. P. Vabishchevich, G. Keeler, T. Pertsch, T. V. Dolgova, I. Staude, I. Brener, and A. A. Fedyanin. “Ultrafast all-optical tuning of direct-gap semiconductor metasurfaces”. *Nature Communications* 8 (2017), p. 17 (cit. on p. 6).

[50] M. A. Kats, R. Blanchard, P. Genevet, Z. Yang, M. M. Qazilbash, D. N. Basov, S. Ramanathan, and F. Capasso. “Thermal tuning of mid-infrared plasmonic antenna arrays using a phase change material”. *Optics Letters* 38.3 (2013), pp. 368–370 (cit. on p. 6).

[51] A. B. Baspinar, T. Zheng, H. Kwon, and A. Faraon. “Nanoelectromechanically Tunable Dielectric Metasurfaces for Reconfigurable Wavefront Shaping”. *ACS Photonics* 11.9 (2024), pp. 3585–3592 (cit. on p. 9).

[52] O. Avayu, E. Almeida, Y. Prior, and T. Ellenbogen. “Composite Functional Metasurfaces for Multispectral Achromatic Optics”. *Nature Communications* 8 (2017), p. 14992 (cit. on p. 9).

[53] J. B. Reeves, R. K. Jayne, T. J. Stark, L. K. Barrett, A. E. White, and D. J. Bishop. “Tunable Infrared Metasurface on a Soft Polymer Scaffold”. *Nano Letters* 18 (2018), pp. 2802–2806 (cit. on p. 9).

[54] A. L. Holsteen, S. Raza, P. Fan, P. G. Kik, and M. L. Brongersma. “Purcell Effect for Active Tuning of Light Scattering from Semiconductor Optical Antennas”. *Science* 358 (2017), pp. 1407–1410 (cit. on p. 9).

[55] J. Y. Ou, E. Plum, L. Jiang, and N. I. Zheludev. “Reconfigurable Photonic Metamaterials”. *Nano Letters* 11 (2011), pp. 2142–2144 (cit. on p. 9).

[56] M. Manjappa, P. Pitchappa, N. Singh, N. Wang, N. I. Zheludev, C. Lee, and R. Singh. “Reconfigurable MEMS Fano Metasurfaces with Multiple-Input–Output States for Logic Operations at Terahertz Frequencies”. *Nature Communications* 9 (2018), p. 4056 (cit. on p. 10).

[57] K. L. Ekinci and M. L. Roukes. “Nanoelectromechanical Systems”. *Review of Scientific Instruments* 76 (2005), p. 061101 (cit. on p. 10).

[58] A. L. Holsteen, A. F. Cihan, and M. L. Brongersma. “Temporal Color Mixing and Dynamic Beam Shaping with Silicon Metasurfaces”. *Science* 365 (2019), pp. 257–260 (cit. on p. 10).

[59] P. Steglich. *Silicon-on-Insulator Slot Waveguides: Theory and Applications in Electro-Optics and Optical Sensing*. 2018 (cit. on p. 10).

[60] Z. Han, A. Y. Elezzabi, and V. Van. “Experimental Realization of Subwavelength Plasmonic Slot Waveguides on a Silicon Platform”. *Optics Letters* 35 (2010), pp. 502–504 (cit. on p. 10).

[61] N.-N. Feng, M. L. Brongersma, and L. Dal Negro. “Metal–Dielectric Slot-Waveguide Structures for the Propagation of Surface Plasmon Polaritons at 1.55 μm”. *IEEE Journal of Quantum Electronics* 43 (2007), pp. 479–485 (cit. on p. 10).

[62] G. Veronis and S. Fan. “Modes of Subwavelength Plasmonic Slot Waveguides”. *Journal of Lightwave Technology* 25 (2007), pp. 2511–2521 (cit. on p. 10).

[63] E. Klopfer, S. Dagli, D. Barton, M. Lawrence, and J. A. Dionne. “High-Quality-Factor Silicon-on-Lithium Niobate Metasurfaces for Electro-Optically Reconfigurable Wavefront Shaping”. *Nano Letters* 22 (2022), pp. 1703–1709 (cit. on pp. 10, 12, 15, 18).

[64] V. R. Almeida, Q. Xu, C. A. Barrios, and M. Lipson. “Guiding and Confining Light in Void Nanostructure”. *Optics Letters* 29 (2004), pp. 1209–1211 (cit. on p. 12).

[65] K. Y. You. *Emerging Waveguide Technology*. 2018 (cit. on p. 12).

[66] J. Witzens, T. Baehr-Jones, and M. Hochberg. “Design of Transmission Line Driven Slot Waveguide Mach-Zehnder Interferometers and Application to Analog Optical Links”. *Optics Express* 18 (2010), p. 16902 (cit. on p. 12).

[67] R. Haldar, V. Mishra, A. Dutt, and S. K. Varshney. “On-Chip Broadband Ultra-Compact Optical Couplers and Polarization Splitters Based on off-Centered and Non-Symmetric Slotted Si-Wire Waveguides”. *Journal of Optics* 18 (2016), p. 105801 (cit. on p. 12).

[68] Z. He, F. Gou, R. Chen, K. Yin, T. Zhan, and S.-T. Wu. “Liquid Crystal Beam Steering Devices: Principles, Recent Advances, and Future Developments”. *Crystals* 9 (2019), p. 292 (cit. on p. 20).

[69] P. F. McManamon, P. J. Bos, M. J. Escuti, J. Heikenfeld, S. Serati, H. Xie, and E. A. Watson. “A Review of Phased Array Steering for Narrow-Band Electrooptical Systems”. *Proceedings of the IEEE* 97 (2009), pp. 1078–1096 (cit. on p. 20).

[70] P. F. McManamon, T. A. Dorschner, D. L. Corkum, L. J. Friedman, D. S. Hobbs, M. Holz, S. Liberman, H. Q. Nguyen, D. P. Resler, R. C. Sharp, and E. A. Watson. “Optical Phased Array Technology”. *Proceedings of the IEEE* 84 (1996), pp. 268–298 (cit. on p. 20).

[71] X. Shang, J.-Y. Tan, O. Willekens, J. De Smet, P. Joshi, D. Cuypers, E. Islamaj, J. Beeckman, K. Neyts, M. Vervaeke, H. Thienpont, and H. De Smet. “Electrically Controllable Liquid Crystal Component for Efficient Light Steering”. *IEEE Photonics Journal* 7 (2015), pp. 1–13 (cit. on p. 20).

[72] X. Chen, S. Jiang, Y. Li, Y. Jiang, W. Wang, and Bayanheshig. “Fabrication of Ultra-High Aspect Ratio Silicon Grating Using an Alignment Method Based on a Scanning Beam Interference Lithography System”. *Optics Express* 30 (2022), pp. 40842–40853 (cit. on p. 20).

[73] P. S. Finnegan, A. E. Hollowell, C. L. Arrington, and A. L. Dagel. “High Aspect Ratio Anisotropic Silicon Etching for X-Ray Phase Contrast Imaging Grating Fabrication”. *Materials Science in Semiconductor Processing* 92 (2019), pp. 80–85 (cit. on p. 20).

[74] Z. Shi, K. Jefimovs, L. Romano, and M. Stampanoni. “Towards the Fabrication of High-Aspect-Ratio Silicon Gratings by Deep Reactive Ion Etching”. *Micromachines* 11 (2020), p. 864 (cit. on p. 20).

[75] M. D. Henry. “ICP Etching of Silicon for Micro and Nanoscale Devices”. PhD thesis. California Institute of Technology, 2010 (cit. on pp. 20, 21).

[76] H. Miao, L. Chen, M. Mirzaeimoghri, R. Kasica, and H. Wen. “Cryogenic Etching of High Aspect Ratio 400-nm Pitch Silicon Gratings”. *Journal of Microelectromechanical Systems* (2016), pp. 963–967 (cit. on p. 20).

[77] M. G. Hogg, I. V. Timoshkin, S. J. MacGregor, M. P. Wilson, M. J. Given, and T. Wang. “Electrical Breakdown of Short Non-Uniform Air Gaps”. *19th IEEE Pulsed Power Conference (PPC)*. 2013, pp. 1–4 (cit. on p. 24).

[78] A. B. Baspinar, P. Pearson, and A. Faraon. “Multilayer Q-BIC-Like Optical Filters with High Throughput Direct-Write Multilayer Lithography”. *Advanced Optical Materials* (2026), e71282 (cit. on pp. 25, 51, 52, 59, 60, 66).

[79] J. Jordaan, A. E. Minovich, D. Neshev, and I. Staude. “Design of Multilayer Huygens’ Metasurfaces for Large-Area Multiwavelength and Polarization-Insensitive Metalenses”. *Optics Express* 33.16 (2025), pp. 33643–33654 (cit. on p. 25).

[80] J. Zhang, L. Ma, and Y. Gong. “Design and Analysis of Terahertz Trilayer Achromatic Grating Metasurface Wave Plate”. *Scientific Reports* 15.1 (2025), p. 5471 (cit. on p. 25).

[81] Y. Zhao, M. A. Belkin, and A. Alù. “Twisted Optical Metamaterials for Planarized Ultrathin Broadband Circular Polarizers”. *Nature Communications* 3.1 (2012), p. 870 (cit. on p. 25).

[82] W. Xu, C. Zhao, H. Li, J. Li, Q. Tan, Y. Liu, H. Xu, Y. Shen, and J. Yao. “Cascaded Metasurface for Polarization-Dependent Varifocal Vortex Beam Manipulation”. *Nanophotonics* 14.17 (), pp. 2881–2890 (cit. on p. 25).

[83] G. Chen, J. Zhou, L. Chen, F. Tian, and Z. Liu. “Infrared Color-Sorting Metasurfaces”. *Nanoscale* 16.30 (2024), pp. 14490–14497 (cit. on pp. 25, 65, 66).

[84] H. Z. Khan, J. Zafar, A. Jabbar, J. u. R. Kazim, M. U. Rehman, M. A. Imran, and Q. H. Abbasi. “Advancements in Metasurfaces for Polarization Control: A Comprehensive Survey”. *Next Research* 2.3 (2025), p. 100407 (cit. on p. 25).

[85] G. Roberts, C. Ballew, T. Zheng, J. C. Garcia, S. Camayd-Muñoz, P. W. C. Hon, and A. Faraon. “3D-patterned Inverse-Designed Mid-Infrared Metaoptics”. *Nature Communications* 14.1 (2023), p. 2768 (cit. on pp. 25, 66).

[86] X. Li, R. Feng, F. Sun, Y. Zhang, Q. Jia, D. Tang, B. Shi, H. Li, Y. Gao, W. Gao, Y. Cao, and W. Ding. “Simultaneous Sorting of Arbitrary Vector Structured Beams with Spin-Multiplexed Diffractive Metasurfaces”. *Advanced Photonics Nexus* 3.3 (2024), p. 036010 (cit. on p. 25).

[87] X. Lin, Y. Rivenson, N. T. Yardimci, M. Veli, Y. Luo, M. Jarrahi, and A. Ozcan. “All-Optical Machine Learning Using Diffractive Deep Neural Networks”. *Science* 361.6406 (2018), pp. 1004–1008 (cit. on p. 25).

[88] X. Luo, Y. Hu, X. Ou, X. Li, J. Lai, N. Liu, X. Cheng, A. Pan, and H. Duan. “Metasurface-Enabled on-Chip Multiplexed Diffractive Neural Networks in the Visible”. *Light: Science & Applications* 11.1 (2022), p. 158 (cit. on p. 25).

[89] G. Soma, K. Komatsu, Y. Nakano, and T. Tanemura. “Complete Vectorial Optical Mode Converter Using Multi-Layer Metasurface”. *Nature Communications* 16.1 (2025), p. 7744 (cit. on p. 25).

[90] H. Zhou, C. Zhao, C. He, L. Huang, T. Man, and Y. Wan. “Optical Computing Metasurfaces: Applications and Advances”. *Nanophotonics* 13.4 (2024), pp. 419–441 (cit. on p. 25).

[91] J. Han, S. Wang, J. Yang, S. Guo, Q. Cao, H. Tang, X. Pu, B. Gao, and X. Li. “Solution-Processed Sb2S3 Planar Thin Film Solar Cells with a Conversion Efficiency of 6.9% at an Open Circuit Voltage of 0.7 V Achieved via Surface Passivation by a SbCl3 Interface Layer”. *ACS Applied Materials & Interfaces* 12.4 (2020), pp. 4970–4979 (cit. on pp. 26, 27).

[92] J. Han, X. Pu, H. Zhou, Q. Cao, S. Wang, J. Yang, J. Zhao, and X. Li. “Multidentate Anchoring through Additive Engineering for Highly Efficient Sb2S3 Planar Thin Film Solar Cells”. *Journal of Materials Science & Technology* 89 (2021), pp. 36–44 (cit. on pp. 26, 27).

[93] G. Wang, S. Wang, Y. Cui, and D. Pan. “A Novel and Versatile Strategy to Prepare Metal–Organic Molecular Precursor Solutions and Its Application in Cu(In,Ga)(S,Se) $_2$ Solar Cells”. *Chemistry of Materials* 24.20 (2012), pp. 3993–3997 (cit. on pp. 26, 27).

[94] H. Wang, H. Yuan, S. Sae Hong, Y. Li, and Y. Cui. “Physical and Chemical Tuning of Two-Dimensional Transition Metal Dichalcogenides”. *Chemical Society Reviews* 44.9 (2015), pp. 2664–2680 (cit. on pp. 26, 27).

[95] X. Wang, J. Li, W. Liu, S. Yang, C. Zhu, and T. Chen. "A Fast Chemical Approach towards $Sb_2 S_3$ Film with a Large Grain Size for High-Performance Planar Heterojunction Solar Cells". *Nanoscale* 9.10 (2017), pp. 3386–3390 (cit. on pp. 26, 27).

[96] W. Wang, P. Pfeiffer, and L. Schmidt-Mende. "Direct Patterning of Metal Chalcogenide Semiconductor Materials". *Advanced Functional Materials* 30.27 (2020), p. 2002685 (cit. on pp. 26, 27, 40).

[97] W. Wang, U. Hübner, T. Chen, A. Gärtner, J. Köbel, F. Jahn, H. Schneidwind, A. Dellith, J. Dellith, T. Wieduwilt, M. Zeisberger, T. A. Shaik, A. Bingel, M. A. Schmidt, J.-S. Huang, and V. Deckert. *Grayscale Electron Beam Lithography Direct Patterned Antimony Sulfide*. 2024. arXiv: 2401.13427 [physics] (cit. on p. 26).

[98] A. Forouzmand and H. Mosallaei. "All-Dielectric C-Shaped Nanoantennas for Light Manipulation: Tailoring Both Magnetic and Electric Resonances to the Desire". *Advanced Optical Materials* 5.14 (2017), p. 1700147 (cit. on p. 26).

[99] S. Campione, S. Liu, L. I. Basilio, L. K. Warne, W. L. Langston, T. S. Luk, J. R. Wendt, J. L. Reno, G. A. Keeler, I. Brener, and M. B. Sinclair. "Broken Symmetry Dielectric Resonators for High Quality Factor Fano Metasurfaces". *ACS Photonics* 3.12 (2016), pp. 2362–2367 (cit. on p. 26).

[100] R. Kanyang, C. Fang, Q. Yang, Y. Shao, G. Han, Y. Liu, and Y. Hao. "Electro-Optical Modulation in High Q Metasurface Enhanced with Liquid Crystal Integration". *Nanomaterials* 12.18 (2022), p. 3179 (cit. on p. 26).

[101] X. Yang, A. Antonov, A. Aigner, T. Weber, Y. Lee, T. Jiang, H. Hu, and A. Tittl. "Polarization-Independent Metasurfaces Based on Bound States in the Continuum with High Q-factor and Resonance Modulation". *Optics Express* 33.7 (2025), pp. 15682–15689 (cit. on p. 26).

[102] L. Kühner, F. J. Wendisch, A. A. Antonov, J. Bürger, L. Hüttenhofer, L. de S. Menezes, S. A. Maier, M. V. Gorkunov, Y. Kivshar, and A. Tittl. "Unlocking the Out-of-Plane Dimension for Photonic Bound States in the Continuum to Achieve Maximum Optical Chirality". *Light: Science & Applications* 12.1 (2023), p. 250 (cit. on p. 26).

[103] L. Gao, Y. Qu, L. Wang, and Z. Yu. "Computational Spectrometers Enabled by Nanophotonics and Deep Learning". *Nanophotonics* 11.11 (2022), pp. 2507–2529 (cit. on p. 27).

[104] C. Liu and Z. Sun. "Design and Fabrication of a Metallic Irregular F–P Filter Array for a Miniature Spectrometer". *Applied Optics* 60.16 (2021), p. 4948 (cit. on pp. 27, 37).

[105] C. Wang, X. Liu, Y. Zhang, Y. Sun, Z. Yu, and Z. Zheng. "Dual-Channel Switchable Metasurface Filters for Compact Spectral Imaging with Deep Compressive Reconstruction". *Nanomaterials* 13.21 (2023), p. 2854 (cit. on p. 27).

[106] J. Xiong, X. Cai, K. Cui, Y. Huang, J. Yang, H. Zhu, W. Li, B. Hong, S. Rao, Z. Zheng, S. Xu, Y. He, F. Liu, X. Feng, and W. Zhang. "Dynamic Brain Spectrum Acquired by a Real-Time Ultraspectral Imaging Chip with Reconfigurable Metasurfaces". *Optica* 9.5 (2022), pp. 461–468 (cit. on p. 27).

[107] B. Craig, V. R. Shrestha, J. Meng, J. J. Cadusch, and K. B. Crozier. "Experimental Demonstration of Infrared Spectral Reconstruction Using Plasmonic Metasurfaces". *Optics Letters* 43.18 (2018), pp. 4481–4484 (cit. on p. 27).

[108] Z. Wang, S. Yi, A. Chen, M. Zhou, T. S. Luk, A. James, J. Nogan, W. Ross, G. Joe, A. Shahsafi, K. X. Wang, M. A. Kats, and Z. Yu. "Single-Shot on-Chip Spectral Sensors Based on Photonic Crystal Slabs". *Nature Communications* 10.1 (2019), p. 1020 (cit. on p. 27).

[109] A. McClung, S. Samudrala, M. Torfeh, M. Mansouree, and A. Arbabi. "Snapshot Spectral Imaging with Parallel Metasystems". *Science Advances* 6.38 (2020), eabc7646 (cit. on p. 27).

[110] M. Alexe, C. Harnagea, W. Erfurth, D. Hesse, and U. Gösele. "100-Nm Lateral Size Ferroelectric Memory Cells Fabricated by Electron-Beam Direct Writing". *Applied Physics A* 70.3 (2000), pp. 247–251 (cit. on p. 27).

[111] T. Bhuvana and G. U. Kulkarni. "Highly Conducting Patterned Pd Nanowires by Direct-Write Electron Beam Lithography". *ACS Nano* 2.3 (2008), pp. 457–462 (cit. on p. 27).

[112] A. Chaker, H. R. Alty, P. Tian, A. Kotsovinos, G. A. Timco, C. A. Muryn, S. M. Lewis, and R. E. P. Winpenny. "Nanoscale Patterning of Zinc Oxide from Zinc Acetate Using Electron Beam Lithography for the Preparation of Hard Lithographic Masks". *ACS Applied Nano Materials* 4.1 (2021), pp. 406–413 (cit. on p. 27).

[113] Y. J. Jeong, T. K. An, D.-J. Yun, L. H. Kim, S. Park, Y. Kim, S. Nam, K. H. Lee, S. H. Kim, J. Jang, and C. E. Park. "Photo-Patternable ZnO Thin Films Based on Cross-Linked Zinc Acrylate for Organic/Inorganic Hybrid Complementary Inverters". *ACS Applied Materials & Interfaces* 8.8 (2016), pp. 5499–5508 (cit. on p. 27).

[114] Y. S. Rim, H. Chen, Y. Liu, S.-H. Bae, H. J. Kim, and Y. Yang. "Direct Light Pattern Integration of Low-Temperature Solution-Processed All-Oxide Flexible Electronics". *ACS Nano* 8.9 (2014), pp. 9680–9686 (cit. on p. 27).

[115] L. D. Zarzar, B. S. Swartzentruber, J. C. Harper, D. R. Dunphy, C. J. Brinker, J. Aizenberg, and B. Kaehr. "Multiphoton Lithography of Nanocrystalline Platinum and Palladium for Site-Specific Catalysis in 3D Microenviron-

ments". *Journal of the American Chemical Society* 134.9 (2012), pp. 4007–4010 (cit. on p. 27).

[116] D. H. Webber and R. L. Brutchey. "Alkahest for V2VI3 Chalcogenides: Dissolution of Nine Bulk Semiconductors in a Diamine-Dithiol Solvent Mixture". *Journal of the American Chemical Society* 135.42 (2013), pp. 15722–15725 (cit. on p. 27).

[117] R. L. Brutchey. "Diorganyl Dichalcogenides as Useful Synthons for Colloidal Semiconductor Nanocrystals". *Accounts of Chemical Research* 48.11 (2015), pp. 2918–2926 (cit. on p. 27).

[118] D. H. Webber, J. J. Buckley, P. D. Antunez, and R. L. Brutchey. "Facile Dissolution of Selenium and Tellurium in a Thiol–Amine Solvent Mixture under Ambient Conditions". *Chemical Science* 5.6 (2014), pp. 2498–2502 (cit. on p. 27).

[119] M. Delaney, I. Zeimpekis, D. Lawson, D. W. Hewak, and O. L. Muskens. "A New Family of Ultralow Loss Reversible Phase-Change Materials for Photonic Integrated Circuits: Sb2S3 and Sb2Se3". *Advanced Functional Materials* 30.36 (2020), p. 2002447 (cit. on pp. 27, 42).

[120] Y. Gutiérrez, A. P. Ovvyan, G. Santos, D. Juan, S. A. Rosales, J. Junquera, P. García-Fernández, S. Dicorato, M. M. Giangregorio, E. Dilonardo, F. Palumbo, M. Modreanu, J. Resl, O. Ishchenko, G. Garry, T. Jonuzi, M. Georghe, C. Cobianu, K. Hingerl, C. Cobet, F. Moreno, W. H. P. Pernice, and M. Losurdo. "Interlaboratory Study on Sb2S3 Interplay between Structure, Dielectric Function, and Amorphous-to-Crystalline Phase Change for Photonics". *iScience* 25.6 (2022) (cit. on pp. 27, 42).

[121] N. Drissi, W. Nouira, and M. Gassoumi. "SPECTROSCOPIC ELLIPSOMETRY ANALYSIS OF A ANTIMONY TRISULFIDE (Sb2S3) THIN FILM". *Chalcogenide Letters* 17.9 (2020), pp. 461–468 (cit. on pp. 27, 42).

[122] D. L. Donoho. "Compressed sensing". *IEEE Transactions on Information Theory* 52.4 (2006), pp. 1289–1306 (cit. on p. 29).

[123] S. Yang and J. C. Ndukaife. *Optofluidic Transport and Particle Trapping Using an All-Dielectric Quasi-BIC Metasurface*. 2022. arXiv: 2212.07054 (cit. on p. 31).

[124] H. Hu, W. Lu, A. Antonov, R. Berté, S. A. Maier, and A. Tittl. "Environmental Permittivity-Asymmetric BIC Metasurfaces with Electrical Reconfigurability". *Nature Communications* 15.1 (2024), p. 7050 (cit. on p. 31).

[125] Z. F. Sadrieva, I. S. Sinev, K. L. Koshelev, A. Samusev, I. V. Iorsh, O. Takayama, R. Malureanu, A. A. Bogdanov, and A. V. Lavrinenko. "Transition from Optical Bound States in the Continuum to Leaky Resonances: Role of Substrate and Roughness". *ACS Photonics* 4.4 (2017), pp. 723–727 (cit. on p. 31).

[126] S. Choi, M. J. Word, V. Kumar, and I. Adesida. "Comparative Study of Thermally Cured and Electron-Beam-Exposed Hydrogen Silsesquioxane Resists". *Journal of Vacuum Science & Technology B: Microelectronics and Nanometer Structures Processing, Measurement, and Phenomena* 26.5 (2008), pp. 1654–1659 (cit. on p. 35).

[127] J. Oliver, W.-B. Lee, and H.-N. Lee. "Filters with Random Transmittance for Improving Resolution in Filter-Array-Based Spectrometers". *Optics Express* 21.4 (2013), pp. 3969–3989 (cit. on p. 36).

[128] S. Wang, L. Lu, and L. Zhu. "Long-Wave Infrared Computational Multispectral Metasurface and Spectral Reconstruction Method". *Scientific Reports* 15.1 (2025), p. 22274 (cit. on pp. 36, 37, 39).

[129] K. Guo, D. Yang, B. Liu, and Z. Guo. "Random Broadband Filters Based on Combination of Metasurface and Multilayer Thin Films for Hyperspectral Imaging". *Journal of Physics D: Applied Physics* 57 (2024) (cit. on pp. 36, 37).

[130] Z. Wang and Z. Yu. "Spectral Analysis Based on Compressive Sensing in Nanophotonic Structures". *Optics Express* 22.21 (2014), pp. 25608–25614 (cit. on pp. 36, 37).

[131] C. Hu, X. Zhao, Y. Qiu, S. Zheng, Q. Zhong, Y. Dong, and T. Hu. "A Computational Microspectrometer Based on Binary-Image-Generated Freeform Metasurfaces for Spectral Sensing". *IEEE Photonics Journal* 16.1 (2024), pp. 1–5 (cit. on pp. 36, 37, 39).

[132] T. Zhao, J. Zhu, W. Wu, Y. Zhang, J. Chen, and L. Zhu. "Computational Spectrum Reconstruction Based on All-Dielectric Metasurface and Correlation Selection". *Optics Communications* 596 (2025), p. 132416 (cit. on p. 36).

[133] X. Tan, Y. Zhang, L. Zhang, Y. Zhu, J. Chen, Y. Zhou, G. Liang, Z. Wen, J. Xiang, and G. Chen. "High Spatial Resolution Spectral Imaging Based on Amplitude-Phase Joint Modulation Metasurfaces Using a Global Optimization Algorithm". *Optics Express* 33.3 (2025), pp. 4765–4777 (cit. on p. 36).

[134] H. He, Y. Zhang, Y. Shao, Y. Zhang, G. Geng, J. Li, X. Li, Y. Wang, L. Bian, J. Zhang, and L. Huang. "Meta-Attention Network Based Spectral Reconstruction with Snapshot Near-Infrared Metasurface". *Advanced Materials* 36.23 (2024), p. 2313357 (cit. on p. 36).

[135] C. Chen, X. Li, G. Yang, X. Chen, S. Liu, Y. Guo, and H. Li. "Computational Hyperspectral Devices Based on Quasi-Random Metasurface Supercells". *Nanoscale* 15.19 (2023), pp. 8854–8862 (cit. on pp. 37, 39).

[136] N. Chen, X. Zhou, L. Yin, R. Chen, and J. Dong. "Angle-Robust Hyperspectral Imaging Based on Quasi-Random Metal Metasurfaces and Cross-Correlation Optimization". *Applied Optics* 64.11 (2025), pp. 2949–2957 (cit. on pp. 37, 39).

[137] M. Yao, C. Qian, J. Yuan, C. Zhu, H. Zhang, J. Weng, S. Pan, X. He, and R. Yin. "Effective Linear-Array Computational Hyperspectral Imaging With Multilayer Thin Films". *IEEE Photonics Technology Letters* 37.18 (2025), pp. 1041–1044 (cit. on p. 37).

[138] T. F. Gonzalez. "Clustering to Minimize the Maximum Intercluster Distance". *Theoretical Computer Science* 38 (1985), pp. 293–306 (cit. on p. 38).

[139] A. Yariv and P. Yeh. *Photonics: Optical Electronics in Modern Communications*. 6th ed. New York: Oxford University Press, 2007 (cit. on p. 43).

[140] A. B. Baspinar, A. Ghita, and A. Faraon. "Sub-Decibel Efficiency Augmented Multilayer Vertical Coupler for Integrated Optics via Adjoint Inverse Design". *In Preparation* (2026) (cit. on p. 48).

[141] D. Thomson, A. Zilkie, J. E. Bowers, T. Komljenovic, G. T. Reed, L. Vivien, D. Marris-Morini, E. Cassan, L. Virot, J.-M. Fédéli, J.-M. Hartmann, J. H. Schmid, D.-X. Xu, F. Boeuf, P. O'Brien, G. Z. Mashanovich, and M. Nedeljković. "Roadmap on silicon photonics". *Journal of Optics* 18.7 (2016), p. 073003 (cit. on p. 48).

[142] G. T. Reed, G. Mashanovich, F. Y. Gardes, and D. J. Thomson. "Silicon optical modulators". *Nature Photonics* 4.8 (2010), pp. 518–526 (cit. on p. 48).

[143] J. Sun, E. Timurdogan, A. Yaacobi, E. S. Hosseini, and M. R. Watts. "Large-scale nanophotonic phased array". *Nature* 493.7431 (2013), pp. 195–199 (cit. on p. 48).

[144] C. V. Poulton, A. Yaacobi, D. B. Cole, M. J. Byrd, M. Raval, D. Vermeulen, and M. R. Watts. "Coherent solid-state LIDAR with silicon photonic optical phased arrays". *Optics Letters* 42.20 (2017), pp. 4091–4094 (cit. on p. 48).

[145] J. Wang, F. Sciarrino, A. Laing, and M. G. Thompson. "Integrated photonic quantum technologies". *Nature Photonics* 14.5 (2020), pp. 273–284 (cit. on p. 48).

[146] J. W. Silverstone, D. Bonneau, J. L. O'Brien, and M. G. Thompson. "Silicon quantum photonics". *IEEE Journal of Selected Topics in Quantum Electronics* 22.6 (2016), pp. 390–402 (cit. on p. 48).

[147] A. L. Washburn and R. C. Bailey. "Photonics-on-a-chip: recent advances in integrated waveguides as enabling detection elements for real-world, lab-on-a-chip biosensing applications". *Analyst* 136.2 (2011), pp. 227–236 (cit. on p. 48).

[148] M. Iqbal, M. A. Gleeson, B. Spaugh, F. Tybor, W. G. Gunn, M. Hochberg, T. Baehr-Jones, R. C. Bailey, and L. C. Gunn. "Label-free biosensor arrays based on silicon ring resonators and high-speed optical scanning instrumentation". *IEEE Journal of Selected Topics in Quantum Electronics* 16.3 (2010), pp. 654–661 (cit. on p. 48).

[149] T. Tamir and S. T. Peng. "Analysis and design of grating couplers". *Applied Physics* 14.3 (1977), pp. 235–254 (cit. on p. 48).

[150] X. Chen, C. Li, C. K. Y. Fung, S. M. G. Lo, and H. K. Tsang. "Apodized waveguide grating couplers for efficient coupling to optical fibers". *IEEE Photonics Technology Letters* 22.15 (2010), pp. 1156–1158 (cit. on pp. 48, 54, 60).

[151] R. Marchetti, C. Lacava, A. Khokhar, X. Chen, I. Cristiani, D. J. Richardson, G. T. Reed, P. Petropoulos, and P. Minzioni. "High-Efficiency Grating-Couplers: Demonstration of a New Design Strategy". *Scientific Reports* 7.1 (2017), p. 16670 (cit. on pp. 48, 54, 60–62).

[152] J. Schrauwen, F. Van Laere, D. Van Thourhout, and R. Baets. "Focused-ion-beam fabrication of slanted grating couplers in silicon-on-insulator waveguides". *IEEE Photonics Technology Letters* 19.11 (2007), pp. 816–818 (cit. on p. 48).

[153] B. Wang, J. Jiang, and G. P. Nordin. "Embedded slanted grating for vertical coupling between fibers and silicon-on-insulator planar waveguides". *IEEE Photonics Technology Letters* 17.9 (2005), pp. 1884–1886 (cit. on p. 48).

[154] F. Van Laere, G. Roelkens, M. Ayre, J. Schrauwen, D. Taillaert, D. Van Thourhout, T. F. Krauss, and R. Baets. "Compact and highly efficient grating couplers between optical fiber and nanophotonic waveguides". *Journal of Lightwave Technology* 25.1 (2007), pp. 151–156 (cit. on p. 48).

[155] W. S. Zaoui, M. F. Rosa, W. Vogel, M. Berroth, J. Butschke, and F. Letzkus. "Cost-effective CMOS-compatible grating couplers with backside metal mirror and 69% coupling efficiency". *Optics Express* 20.26 (2012), B238–B243 (cit. on p. 48).

[156] W. S. Zaoui, A. Kunze, W. Vogel, M. Berroth, J. Butschke, F. Letzkus, and H. Burghartz. "Bridging the gap between optical fibers and silicon photonic integrated circuits". *Optics Express* 22.2 (2014), pp. 1277–1286 (cit. on p. 48).

[157] R. Marchetti, C. Lacava, L. Carroll, K. Gradkowski, and P. Minzioni. "Coupling strategies for silicon photonics integrated chips". *Photonics Research* 7.2 (2019), pp. 201–239 (cit. on p. 48).

[158] M. Kohli, D. Chelladurai, B. Vukovic, D. Moor, D. Bisang, K. Keller, A. Messner, T. Buriakova, M. Zervas, Y. Fedoryshyn, U. Koch, and J. Leuthold. "C- and O-band dual-polarization fiber-to-chip grating couplers

for silicon nitride photonics". *ACS Photonics* 10.9 (2023), pp. 3366–3373 (cit. on pp. 48, 60).

[159] W. Fraser, R. Korček, I. Glesk, J. Litvik, J. H. Schmid, P. Cheben, W. N. Ye, and D. Benedikovic. "High-efficiency metamaterial-engineered grating couplers for silicon nitride photonics". *Nanomaterials* 14.7 (2024), p. 581 (cit. on pp. 48, 60).

[160] W. Fraser, R. Korček, I. Glesk, J. Litvik, J. H. Schmid, P. Cheben, W. N. Ye, and D. Benedikovic. "High-efficiency self-focusing metamaterial grating coupler in silicon nitride with amorphous silicon overlay". *Scientific Reports* 14 (2024), p. 11651 (cit. on pp. 49, 60).

[161] T. K. Saha and W. Zhou. "High efficiency diffractive grating coupler based on transferred silicon nanomembrane overlay on photonic waveguide". *Journal of Physics D: Applied Physics* 42.8 (2009), p. 085115 (cit. on pp. 49, 60).

[162] D. Vercruysse, N. V. Sapra, L. Su, R. Trivedi, and J. Vucković. "Analytical level set fabrication constraints for inverse design". *Scientific Reports* 9.1 (2019), p. 8999 (cit. on p. 49).

[163] S. Molesky, Z. Lin, A. Y. Piggott, W. Jin, J. Vucković, and A. W. Rodriguez. "Inverse design in nanophotonics". *Nature Photonics* 12.11 (2018), pp. 659–670 (cit. on p. 49).

[164] C. M. Lalau-Keraly, S. Bhargava, O. D. Miller, and E. Yablonovitch. "Adjoint shape optimization applied to electromagnetic design". *Optics Express* 21.18 (2013), pp. 21693–21701 (cit. on pp. 49, 54).

[165] D. Maclaurin, D. Duvenaud, and R. P. Adams. "Autograd: Effortless gradients in NumPy". *ICML Workshop on Automatic Machine Learning*. 2015 (cit. on pp. 49, 55, 63).

[166] D. P. Kingma and J. Ba. "Adam: A method for stochastic optimization". *Proceedings of the International Conference on Learning Representations (ICLR)*. 2015 (cit. on pp. 49, 55, 68).

[167] N. V. Sapra, D. Vercruysse, L. Su, K. Y. Yang, J. Skarda, A. Y. Piggott, and J. Vuckovic. "Inverse Design and Demonstration of Broadband Grating Couplers". *IEEE Journal of Selected Topics in Quantum Electronics* 25.3 (2019), pp. 1–7 (cit. on pp. 49, 53, 54, 61).

[168] A. Y. Piggott, J. Lu, T. M. Babinec, K. G. Lagoudakis, J. Petykiewicz, and J. Vučković. "Inverse design and implementation of a wavelength demultiplexing grating coupler". *Scientific Reports* 4 (2014), p. 7210 (cit. on pp. 49, 53).

[169] A. M. Hammond, J. B. Slaby, M. J. Probst, and S. E. Ralph. "Multi-Layer Inverse Design of Vertical Grating Couplers for High-Density, Commercial Foundry Interconnects". *Optics Express* 30.17 (2022), pp. 31058–31072 (cit. on pp. 49, 60, 61).

[170] A. Michaels and E. Yablonovitch. “Inverse design of near unity efficiency perfectly vertical grating couplers”. *Optics Express* 26.4 (2018), pp. 4766–4779 (cit. on p. 49).

[171] R. Halir, P. Cheben, S. Janz, D.-X. Xu, Í. Molina-Fernández, and J. G. Wangüemert-Pérez. “Waveguide grating coupler with subwavelength microstructures”. *Optics Letters* 34.9 (2009), pp. 1408–1410 (cit. on p. 52).

[172] W. D. Sacher, Y. Huang, L. Ding, B. J. F. Taylor, H. Jayatilleka, G.-Q. Lo, and J. K. S. Poon. “Wide bandwidth and high coupling efficiency Si_3N_4-on-SOI dual-level grating coupler”. *Optics Express* 22.9 (2014), pp. 10938–10947 (cit. on p. 52).

[173] Flexcompute Inc. *tidy3D: FDTD electromagnetic simulation software*. https://www.flexcompute.com/tidy3d/. 2024 (cit. on pp. 52, 55, 63).

[174] D. Taillaert, F. Van Laere, M. Ayre, W. Bogaerts, D. Van Thourhout, P. Bienstman, and R. Baets. “Grating Couplers for Coupling between Optical Fibers and Nanophotonic Waveguides”. *Japanese Journal of Applied Physics* 45.8R (2006), pp. 6071–6077 (cit. on p. 53).

[175] M. Delaney, I. Zeimpekis, D. Lawson, D. W. Hewak, and O. L. Muskens. “A New Family of Ultralow Loss Reversible Phase-Change Materials for Photonic Integrated Circuits: Sb_2S_3 and Sb_2Se_3”. *Advanced Functional Materials* 30.36 (2020), p. 2002447 (cit. on p. 53).

[176] Y. Gutiérrez, A. P. Ovvyan, G. Santos, D. Juan, S. A. Rosales, J. Junquera, P. García-Fernández, S. Dicorato, M. M. Giangregorio, E. Dilonardo, F. Palumbo, M. Modreanu, J. Resl, O. Ishchenko, G. Garry, T. Jonuzi, M. Georghe, C. Cobianu, K. Hingerl, C. Cobet, F. Moreno, W. H. P. Pernice, and M. Losurdo. “Interlaboratory study on Sb_2S_3 interplay between structure, dielectric function, and amorphous-to-crystalline phase change for photonics”. *iScience* 25.6 (2022), p. 104377 (cit. on pp. 53, 60).

[177] S. Molesky, Z. Lin, A. Y. Piggott, W. Jin, J. Vučković, and A. W. Rodriguez. “Inverse design in nanophotonics”. *Nature Photonics* 12.11 (2018), pp. 659–670 (cit. on pp. 53, 54, 99).

[178] A. M. Hammond, A. Oskooi, S. G. Johnson, and S. E. Ralph. “Photonic topology optimization with semiconductor-foundry design-rule constraints”. *Optics Express* 29.15 (2021), pp. 23916–23938 (cit. on p. 53).

[179] J.-H. Chen, A. D. Bouamra, C.-L. Wu, A. Fiore, and S.-Y. Tseng. “High-Tolerance Grating Couplers for Vertical Backside Coupling”. *Applied Sciences* 14.23 (2024), p. 11015 (cit. on p. 61).

[180] S. E. Hansen, G. Arregui, A. N. Babar, M. Albrechtsen, B. V. Lahijani, R. E. Christiansen, and S. Stobbe. “Efficient Low-Reflection Fully Etched Vertical Free-Space Grating Couplers for Suspended Silicon Photonics”. *Optics Express* 31.11 (2023), pp. 17424–17436 (cit. on p. 61).

[181] S.-Y. Huang and S. Barz. *Compact Inversely-Designed Vertical Coupler with Bottom Reflector for Sub-Decibel Fiber-to-Chip Coupling on Silicon-on-Insulator Platform*. 2024. arXiv: 2409.10660 [physics] (cit. on pp. 60–62).

[182] X. Jin, J. Xu, C. Xue, C. Guo, L. Fu, M. Liu, Y. Shen, X. Quan, and X. Cheng. "Design and Demonstration of High Efficiency Perfectly Vertical Grating Couplers with a Random Structure". *Optics Letters* 49.7 (2024), pp. 1856–1859 (cit. on p. 61).

[183] B. Shen, P. Wang, R. Polson, and R. Menon. "Integrated Metamaterials for Efficient and Compact Free-Space-to-Waveguide Coupling". *Optics Express* 22.22 (2014), pp. 27175–27182 (cit. on pp. 61, 62).

[184] A. J. Van Lange, A. Lof, and D. Van Oosten. "Non-Contact Surface Grating Coupling for Arrays of Atom–Photonic Devices". *Journal of the Optical Society of America B* 37.4 (2020), p. 921 (cit. on p. 61).

[185] B. Xiong, W. Ma, W. Wang, X. Hu, and T. Chu. "Compact Vertical Grating Coupler with an Achromatic In-Plane Metalens on a 220-Nm Silicon-on-Insulator Platform". *Optics Express* 30.20 (2022), pp. 36254–36264 (cit. on p. 61).

[186] M. Yang, Y. Yan, Z. Wu, Y. Gu, S. Zhao, G. Morthier, and M. Zhao. "High-Performance Grating Couplers on 220-Nm Thick Silicon by Inverse Design for Perfectly Vertical Coupling". *Scientific Reports* 13.1 (2023), p. 18112 (cit. on p. 61).

[187] G. Zhong, H. Xu, R. Zhang, and Y. Tian. "Highly Efficient Perfectly Vertical Grating Couplers Based on the Adjoint Optimization for O-band Operation". *Optics Communications* 596 (2025), p. 132505 (cit. on pp. 61, 62).

[188] A. B. Baspinar*, I. Foo*, and A. Faraon. "Multilayer Bayer Filter in Visible via Direct-Write E-Beam Lithography". *In Preparation* (2026) (cit. on pp. 65, 74).

[189] X. Zou, Y. Zhang, R. Lin, G. Gong, S. Wang, S. Zhu, and Z. Wang. "Pixel-Level Bayer-Type Colour Router Based on Metasurfaces". *Nature Communications* 13.1 (2022), p. 3288 (cit. on pp. 65, 66).

[190] C. Kim, J. Hong, J. Jang, G.-Y. Lee, Y. Kim, Y. Jeong, and B. Lee. "Freeform Metasurface Color Router for Deep Submicron Pixel Image Sensors". *Science Advances* 10 (2024), eadn9000 (cit. on pp. 65, 66).

[191] P. B. Catrysse and B. A. Wandell. "Optical Efficiency of Image Sensor Pixels". *Journal of the Optical Society of America A* 19.8 (2002), pp. 1610–1620 (cit. on p. 66).

[192] J. E. Farrell, F. Feng, and S. Kavusi. "Resolution and Light Sensitivity Tradeoff with Pixel Size". *Proceedings of SPIE* 6069 (2006), 60690N (cit. on p. 66).

[193] C. Park, S. Lee, T. Lee, J. Kang, J. Jeon, C. Park, S. Kim, H. Chung, and M. S. Jang. "Towards Subwavelength Pixels: Nanophotonic Color Routers for Ultra-Compact High-Efficiency CMOS Image Sensors". *Journal of Optics* 26.9 (2024), p. 093002 (cit. on p. 66).

[194] M. Miyata, N. Nemoto, K. Shikama, F. Kobayashi, and T. Hashimoto. "Full-Color-Sorting Metalenses for High-Sensitivity Image Sensors". *Optica* 8.12 (2021), pp. 1596–1604 (cit. on p. 66).

[195] Y. Shao, S. Guo, R. Chen, Y. Dang, Y. Zhou, Y. Wang, J. Zhan, J. Yu, B. Ju, and Y. Ma. "Pixelated NIR–VIS Spectral Routers Based on 2D Mie-Type Metagratings". *Laser & Photonics Reviews* 17.8 (2023), p. 2300027 (cit. on p. 66).

[196] Kavli Nanoscience Institute. *Nanoscribe PPGT: Microscale 3D Printer*. https://lab.kni.caltech.edu/Nanoscribe_PPGT:_Microscale_3D_Printer. 2024 (cit. on p. 66).

[197] M. McLamb, Y. Li, P. Stinson, and T. Hofmann. "Metasurfaces for the Infrared Spectral Range Fabricated Using Two-Photon Polymerization". *Thin Solid Films* 721 (2021), p. 138548 (cit. on p. 66).

[198] Y. Fujii, D. Angerhausen, R. Deitrick, S. Domagal-Goldman, J. L. Grenfell, H. Y, S. R. Kane, E. Pallé, H. Rauer, N. Siegler, K. Stapelfeldt, and K. B. Stevenson. "Exoplanet Biosignatures: Observational Prospects". *Astrobiology* 18.6 (2017), pp. 739–778 (cit. on p. 75).

[199] B. P. Crill and N. Siegler. "Space technology for directly imaging and characterizing exo-Earths". *UV/Optical/IR Space Telescopes and Instruments: Innovative Technologies and Concepts VIII*. Vol. 10398. SPIE, 2017, pp. 175–195 (cit. on p. 75).

[200] D. Mawet, L. Pueyo, P. Lawson, L. Mugnier, W. Trauger, and A. e. a. Boccaletti. "Review of small-angle coronagraphic techniques in the wake of ground-based second-generation adaptive optics systems". *Proc. SPIE 8442, Adaptive Optics Systems III*. 2012, p. 844204 (cit. on p. 75).

[201] National Academies of Sciences, Engineering, and Medicine. *Pathways to Discovery in Astronomy and Astrophysics for the 2020s*. Washington, DC: The National Academies Press, 2021 (cit. on p. 75).

[202] O. Guyon. "Limits of adaptive optics for high-contrast imaging". *Astrophysical Journal* 629.1 (2005), pp. 592–614 (cit. on p. 75).

[203] W. A. Traub and B. R. Oppenheimer. "Direct Imaging of Exoplanets". *Exoplanets*. Ed. by S. Seager. Tucson, AZ: University of Arizona Press, 2010, pp. 111–156 (cit. on p. 75).

[204] D. Mawet, P. Riaud, O. Absil, and J. Surdej. "Annular Groove Phase Mask Coronagraph". *The Astrophysical Journal* 633.2 (2005), p. 1191 (cit. on p. 75).

[205] E. Serabyn, D. Mawet, and R. Burruss. “An image of an exoplanet separated by two diffraction beamwidths from a star”. *Nature* 464 (2010), pp. 1018–1020 (cit. on p. 75).

[206] X. Wang, Z. Nie, Y. Liang, J. Wang, T. Li, and B. Jia. “Recent advances on optical vortex generation”. *Nanophotonics* 7.9 (2018), pp. 1533–1556 (cit. on p. 76).

[207] F. Mei, G. Qu, X. Sha, J. Han, M. Yu, H. Li, Q. Chen, Z. Ji, J. Ni, C.-W. Qiu, Q. Song, Y. Kivshar, and S. Xiao. “Cascaded metasurfaces for high-purity vortex generation”. *Nature Communications* 14.1 (2023), p. 6410 (cit. on p. 76).

[208] M. D. Shafqat, N. Mahmood, J. Akbar, M. Zubair, Y. Massoud, and M. Q. Mehmood. “Broadband multifunctional metasurfaces for concentric perfect vortex beam generation via trigonometric functions”. *Optical Materials Express* 14.1 (2024), pp. 125–138 (cit. on p. 76).

[209] A. V. Carpentier, H. Michinel, J. R. Salgueiro, and R. Garcia-Fernandez. “Making optical vortices with computer-generated holograms”. *American Journal of Physics* 76.10 (2008), pp. 916–921 (cit. on p. 76).

[210] A. Bekshaev, V. Pas’ko, T. Fadeyeva, and A. Volyar. “Generation of optical vortex light beams using volume holograms with embedded phase singularity”. *arXiv preprint arXiv:1203.6322* (2012) (cit. on p. 76).

[211] J. Kühn, M. C. Aksoy, T. Öztürk, B. Oslake, S. Orhan, C. Yilmaz, C. Ulusoy, and H. H. Esenoglu. “The Programmable Liquid-crystal Active Coronagraphic Imager for the DAG telescope (PLACID)”. *Proceedings of SPIE*. Vol. 12184. 2022, p. 121841V (cit. on p. 76).

[212] I. Laginja, J. Jewell, T. Morgan, J. Krist, D. Mawet, J. Trauger, E. Sidick, C. Dorrer, M. Perrin, and R. Belikov. “Liquid crystal coronagraph prototypes for imaging exo-Earth candidates”. *arXiv preprint arXiv:2404.14723* (2024) (cit. on p. 76).

[213] G. Foo, D. M. Palacios, and G. A. Swartzlander. “Optical vortex coronagraph”. *Optics Letters* 30.24 (2005), pp. 3308–3310 (cit. on p. 76).

[214] N. Yu and F. Capasso. “Flat optics with designer metasurfaces”. *Nature Materials* 13.2 (2014), pp. 139–150 (cit. on p. 76).

[215] Y. Guo, M. Pu, F. Zhang, M. Xu, X. Li, X. Ma, and X. Luo. “Classical and generalized geometric phase in electromagnetic metasurfaces”. *Photonics Insights* 1.1 (2022), R03 (cit. on p. 76).

[216] E. S. Douglas, J. Debes, B. Mennesson, B. Nemati, J. Ashcraft, B. Ren, K. R. Stapelfeldt, D. Savransky, N. K. Lewis, and B. Macintosh. “Sensitivity of the Roman Coronagraph Instrument to Exozodiacal Dust”. *Publications of the Astronomical Society of the Pacific* 134.1032 (2022), p. 024402 (cit. on p. 77).

[217] M. Kang, T. Feng, H.-T. Wang, and J. Li. “Wave front engineering from an array of thin aperture antennas”. *Optics express* 20.14 (2012), pp. 15882–15890 (cit. on p. 77).

[218] W. T. Chen, A. Y. Zhu, and F. Capasso. “Flat optics with dispersion-engineered metasurfaces”. *Nature Reviews Materials* 5.8 (2020), pp. 604–620 (cit. on p. 77).

[219] V. Liu and S. Fan. “S4: A free electromagnetic solver for layered periodic structures.” *Computer Physics Communications* 183.10 (2012), pp. 2233–2244 (cit. on p. 78).

[220] G. Ruane, D. Mawet, J. B. Jewell, and S. B. Shaklan. “Performance and sensitivity of vortex coronagraphs on segmented space telescopes”. *Techniques and Instrumentation for Detection of Exoplanets VIII* 10400 (2017), pp. 140–155 (cit. on p. 79).

[221] G. Ruane, J. B. Jewell, D. Mawet, S. B. Shaklan, and C. C. Stark. “Segmented coronagraph design and analysis (SCDA): an initial design study of apodized vortex coronagraphs”. *arXiv: Instrumentation and Methods for Astrophysics* (2017) (cit. on p. 79).

[222] R. C. Devlin, M. Khorasaninejad, W. T. Chen, J. Oh, and F. Capasso. “Broadband high-efficiency dielectric metasurfaces for the visible spectrum”. *Proceedings of the National Academy of Sciences* 113.38 (2016), pp. 10473–10478 (cit. on p. 80).

[223] M. Khorasaninejad, W. T. Chen, R. C. Devlin, J. Oh, A. Y. Zhu, and F. Capasso. “Metalenses at visible wavelengths: Diffraction-limited focusing and subwavelength resolution imaging”. *Science* 352.6290 (2016), pp. 1190–1194 (cit. on p. 80).

[224] A. McWilliam, M. A. A. Khafaji, S. J. Svensson, S. Pádua, and S. Franke-Arnold. “Dynamic Mueller matrix polarimetry using generalized measurements”. *Optics Express* 32.12 (2024), pp. 21909–21924 (cit. on p. 81).

[225] E. H. Por, S. Y. Haffert, V. M. Radhakrishan, D. S. Doelman, M. van Kooten, and S. P. Bos. “High Contrast Imaging for Python (HCIPy): an open-source adaptive optics and coronagraph simulator.” *Adaptive Optics Systems VI* 10703 (2018), pp. 1112–1125 (cit. on p. 84).

[226] Z. Li, R. Pestourie, Z. Lin, S. G. Johnson, and F. Capasso. “Empowering Metasurfaces with Inverse Design: Principles and Applications.” *ACS Photonics* 9.7 (2022), pp. 2178–2192 (cit. on p. 85).

[227] V. V. Kotlyar, A. A. Kovalev, A. G. Nalimov, and S. S. Stafeev. “Topological Charge of Multi-Color Optical Vortices.” *Photonics* 9.3 (2022), p. 145 (cit. on p. 85).

[228] L. Perumal, S. Hengsbach, M. Mahdavifar, J. Korvink, and A. Forbes. “3D Printed Optics Achieves Broadband Structured Light.” *Advanced Optical Materials* (2025), p. 2403028 (cit. on p. 85).

[229] T. Udem, R. Holzwarth, and T. W. Hänsch. “Optical frequency metrology”. *Nature* 416 (2002), pp. 233–237 (cit. on p. 86).

[230] S. Haroche. “Nobel Lecture: Controlling photons in a box and exploring the quantum to classical boundary”. *Reviews of Modern Physics* 85 (2013), pp. 1083–1102 (cit. on p. 86).

[231] B. P. Abbott et al. “Observation of Gravitational Waves from a Binary Black Hole Merger”. *Physical Review Letters* 116 (2016), p. 061102 (cit. on p. 86).

[232] M. Ossiander, M. L. Meretska, S. Rourke, C. Spägele, X. Yin, I.-C. Benea-Chelmus, and F. Capasso. “Metasurface-stabilized optical microcavities”. *Nature Communications* 14 (2023), p. 1114 (cit. on pp. 86, 87).

[233] J. Flannery, R. Al Maruf, T. Yoon, and M. Bajcsy. “Fabry-Pérot Cavity Formed with Dielectric Metasurfaces in a Hollow-Core Fiber”. *ACS Photonics* 5.2 (2018), pp. 337–341 (cit. on p. 87).

[234] J. Fu, Y. Jin, and S. He. “Metasurface for Constructing a Stable High-Q Plano-Planar Open Cavity”. *Advanced Optical Materials* 7.5 (2019), p. 1801339 (cit. on p. 87).

[235] S. Mason, M. L. Meretska, C. Spägele, M. Ossiander, and F. Capasso. “Metasurface-Controlled Holographic Microcavities”. *ACS Photonics* 11.3 (2024), pp. 941–949 (cit. on p. 87).

[236] T. Xie, J. Rochman, J. G. Bartholomew, A. Ruskuc, J. M. Kindem, I. Craiciu, C. Thiel, R. Cone, and A. Faraon. “Characterization of Er^{3+}:YVO_4 for microwave to optical transduction”. *Physical Review Applied* 16 (2021), p. 044006 (cit. on p. 87).

[237] T. Xie et al. “Scalable microwave-to-optical transducers at the single-photon level with spins”. *Nature Physics* (2025) (cit. on pp. 87, 88).